



TECHNISCHE UNIVERSITÄT MÜNCHEN

Fakultät für Medizin

**Deciphering Pulmonary Delivery and Biokinetics of
Nanoparticles in Murine Lungs using Novel Imaging
Techniques**

Lin Yang

Vollständiger Abdruck der von der Fakultät für Medizin der Technischen
Universität München zur Erlangung des akademischen Grades eines

Doktor der Naturwissenschaften (Dr. rer. nat.)

genehmigten Dissertation.

Vorsitzender: Prof. Wolfgang Weber

Prüfer der Dissertation: 1. Prof. Dr. Gil Gregor Westmeyer

2. Prof. Dr. Franz Pfeiffer

Die Dissertation wurde am 10.12.2019 bei der Technische Universität München
eingereicht und durch die Fakultät für Medizin am 06.10.2020 angenommen.

TECHNISCHE UNIVERSITÄT MÜNCHEN

Fakultät für Medizin

**Deciphering Pulmonary Delivery and Biokinetics of
Nanoparticles in Murine Lungs using Novel Imaging
Techniques**

Dissertation

zur Erlangung des Grades

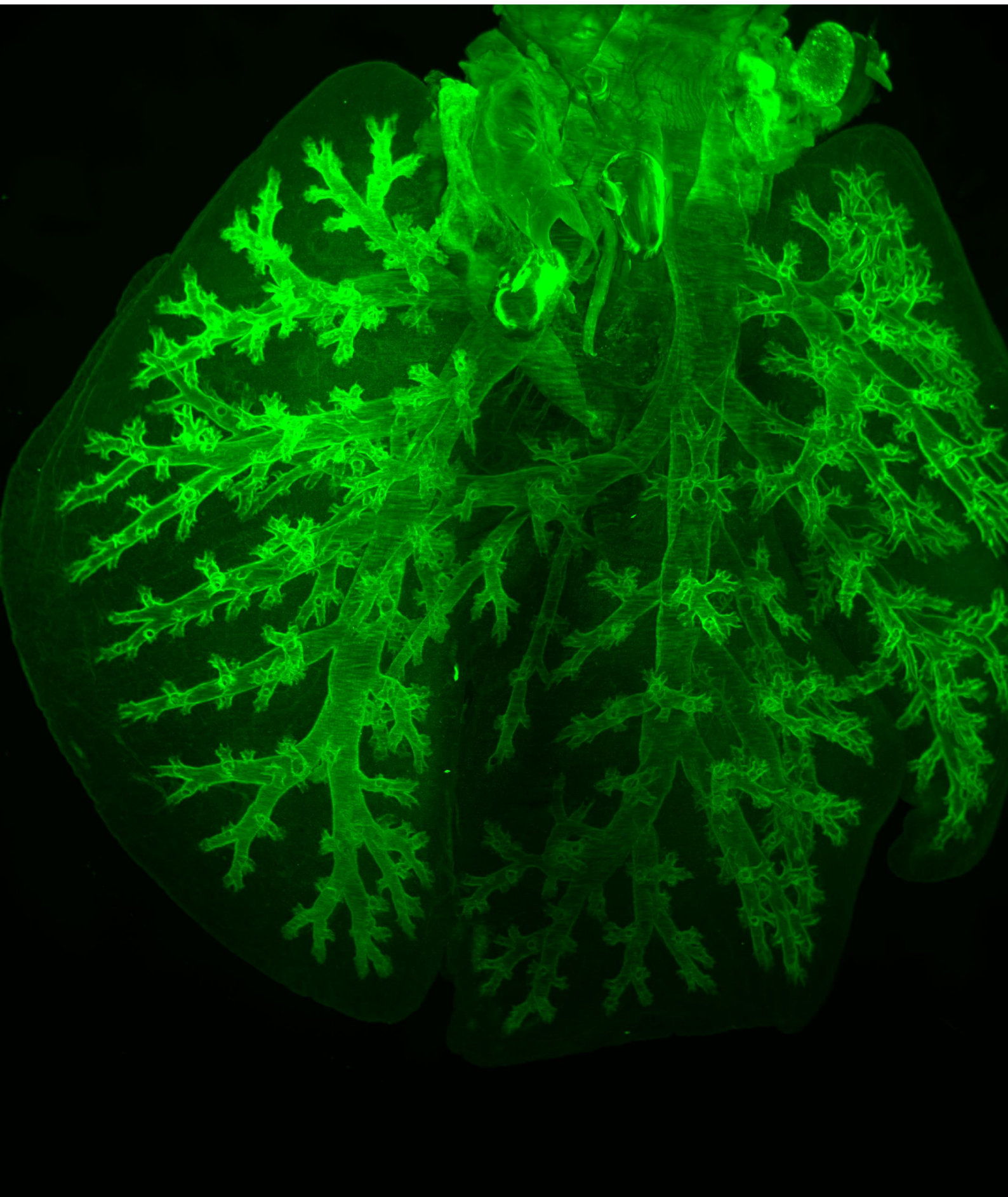
Doktor der Naturwissenschaften

(Dr. rer. nat.)

Lin Yang

München 2019

The work was performed under the guidance of Dr. Otmar Schmid, Helmholtz Zentrum München.



If you can't explain it simply, you don't understand it well enough.

-Albert Einstein

Table of Contents

Abbreviations.....	I
Peer-reviewed Publications (PRP) for this dissertation	II
Abstract.....	III
1. Introduction	1
1.1 Nanotechnology in inhalation therapy and toxicology.....	1
1.1.1 Nanomedicine.....	1
1.1.2 Nano-biokinetics	3
1.1.3 Dosimetry and Nanotoxicology.....	6
1.2 Application routes of pulmonary delivery	9
1.2.1 Clinical pulmonary delivery routes/devices.....	9
1.2.2 Preclinical pulmonary delivery routes/devices.....	11
1.3 Imaging tools to assess the pulmonary delivery and distribution.....	15
1.3.1 Nuclear medical imaging.....	15
1.3.2 MRI.....	16
1.3.3 X-ray based imaging.....	17
1.3.4 Optical imaging	18
1.3.5 Hybrid lung imaging	19
2. Aim of this study	21
3. Materials and methods.....	23
3.1 Materials.....	23
3.2 Size measurement of particle suspensions.....	23
3.3 Animal handling and methods of pulmonary substance delivery	23
3.3.1 Regular intratracheal instillation (PRP1).....	24
3.3.2 Ventilator-assisted aerosol inhalation 1.0 (PRP1).....	24
3.3.3 Intratracheal slow-instillation (PRP2)	24
3.3.4 Ventilator-assisted aerosol inhalation 2.0 (PRP2).....	25
3.3.5 Intranasal aspiration (PRP2).....	26
3.3.6 Other routes.....	26
3.4 <i>In vivo</i> propagation-based phase contrast X-ray imaging (PB-PCXI).....	27
3.5 <i>Ex vivo</i> lung computed tomography	27
3.6 <i>Ex vivo</i> whole-lung and lung-slice fluorescence imaging.....	28
3.7 <i>Ex vivo</i> tissue-clearing LSFM	29
3.8 Image processing and analysis.....	29

3.8.1 Determination of lung morphology	29
3.8.2 Establishment of the intensity-dose conversion curve for particle dosimetry.....	30
3.8.3 C/P and lobe-wise distribution analysis.....	30
3.9 Quantitative fluorescence analysis of particle dose in lung homogenates	32
3.10 Statistical Analysis.....	32
4. Results.....	33
4.1 Summary of the work PRP1	33
4.2 Summary of the work PRP2	48
5. Discussion.....	66
6. Outlook	74
7. References	76
8. Acknowledgments.....	84

Abbreviations

NP	Nanoparticle
NM	Nanomedicine
MIP	Maximum intensity projection
WHO	World Health Organization
COPD	Chronic obstructive pulmonary disease
NSCLC	Non-small-cell lung cancer
SCLC	Small cell lung cancer
AMs	Alveolar macrophage
GIT	Gastrointestinal tract
TEM	Transmission electron microscopy
MRI	Magnetic resonance imaging
SPECT	Single photon emission computed tomography
PET	Positron emission tomography
PCXI	Phase-contrast X-ray imaging
CT	Computed tomography
ICP-MS	Inductively coupled plasma-mass spectrophotometer
IVIS	<i>In vivo</i> imaging system
LSFM	Light sheet fluorescent microscopy
PMNs	Polymorphonuclear neutrophils
pMDIs	Pressurized metered-dose inhalers
DPIs	Dry powder inhalers
CFCs	Chlorofluorocarbons
HFAs	Hydrofluoroalkanes
NIR	Near-infrared region
PA	Photoacoustic
NMR	Nuclear Magnetic Resonance
FMT	Fluorescent molecular tomography
CCD	Charge coupled device
QDs	Quantum dots
3D	Three-dimensional
PB-PCXI	Propagation-based phase-contrast X-ray imaging
ex/em	Excitation/emission
VMD	Volume median diameter
MF NP	Melamine resin fluorescence nanoparticle
DLS	Dynamic light scattering
WLFI	Whole lung fluorescence imaging
LSFI	Lung slice fluorescent imaging
THF	Tetrahydrofuran
DCM	Dichloromethane
DBE	Dibenzyl ether
MCL	Mean chord length
SD	Standard deviation
CAST	Computer-assisted stereological toolbox
AAD	Adaptive aerosol delivery

Peer-reviewed Publications (PRP) for this dissertation

The publication-based dissertation includes the following two peer-reviewed papers with me as the first author.

Yang, L., Feuchtinger, A., Möller, W., Ding, Y., Kutschke, D.,... **Stoeger, T., Razansky, D., Walch, A., Schmid, O.** 2019. Three-Dimensional Quantitative Co-Mapping of Pulmonary Morphology and Nanoparticle Distribution with Cellular Resolution in Nondissected Murine Lungs. *ACS Nano*, 13(2), pp.1029-1041. (**PRP1**)

Yang, L., Gradl, R., Dierolf, M., Möller, W., Kutschke, D.,... **Stoeger, T., Razansky, D., Pfeiffer, F., Morgan, K.S., Schmid, O.** 2019. Multimodal Precision Imaging of Pulmonary Nanoparticle Delivery in Mice: Dynamics of Application, Spatial Distribution, and Dosimetry. *Small*, p.1904112. (**PRP2**)

Related publications are not included in the thesis during the doctoral study

Gradl, R., Dierolf, M., Yang, L., Hehn, L., Günther, B., Möller, W., Kutschke, D., Stoeger, T., Gleich, B., Achterhold, K., Donnelley, M., **Pfeiffer, F., Schmid, O., Morgan, K.S.** 2019. Visualizing treatment delivery and deposition in mouse lungs using in vivo x-ray imaging. *Journal of Controlled Release*, 307, pp282-291

Gradl, R., Morgan, K.S., Dierolf, M., Jud, C., Hehn, L., Günther, B., Möller, W., Kutschke, D., Yang, L., Stoeger, T.,... Schmid, O., Pfeiffer, F. 2018. Dynamic in vivo chest x-ray dark-field imaging in mice. *IEEE transactions on medical imaging*, 38(2), pp.649-656.

Gradl, R., Dierolf, M., Günther, B., Hehn, L., Möller, W., Kutschke, D., Yang, L., Donnelley, M.,... Schmid, O., Pfeiffer, F., Morgan, K.S. 2018. In vivo dynamic phase-contrast X-ray imaging using a compact light source. *Scientific reports*, 8(1), p.6788.

Doryab, A., Tas, S., Taskin, M.B., Yang, L., Hilgendorff, A., Groll, J., Wagner, D.E., Schmid, O., 2019. Evolution of Bioengineered Lung Models: Recent Advances and Challenges in Tissue Mimicry for Studying the Role of Mechanical Forces in Cell Biology. *Advanced Functional Materials*, p.1903114.

Yang, L., Kuang, H., Zhang, W., Wei, H., **Xu, H.**, 2018. Quantum dots cause acute systemic toxicity in lactating rats and growth restriction of offspring. *Nanoscale*, 10(24), pp.11564-11577.

Abstract

Pulmonary drug delivery is the primary route for the treatment of lung diseases. Drug nanocarriers or nanomedicine/nanoparticles (NM/NPs) have exhibited great potential to enhance both therapeutic and diagnostic (theranostic) efficacy because of their nanometer size range (*e.g.*, high surface area to mass ratio, deep penetration to disease regions; nano-specific cellular uptake/biokinetics) and the merits of (nano)-drug carriers (*e.g.*, surface functionalization with cell-specific ligands for cellular targeting, protection from metabolic degradation). The therapeutic effect of inhaled NM/NPs is dependent upon the delivered dose and its spatial distribution throughout the lung. Deciphering pulmonary drug delivery in the context of delivery dynamics, dose, distribution, biokinetics, and bioactivity of NM/NPs with high enough spatial resolution in nondissected, whole organ tissue (*e.g.*, the lung) is of utmost importance for the development of novel NM with improved therapeutic index (maximized efficacy and minimized side effects), but remains elusive due to the lack of effective imaging tools.

This study introduces *ex vivo* light sheet fluorescence microscopy (LSFM) on tissue-cleared lungs for three dimensional (3D) co-mapping of lung morphology and NP distribution with single-cell resolution in non-dissected whole mouse lungs. The 3D airway architecture of the entire lung can be clearly visualized by tissue autofluorescence allowing for staining-free, quantitative morphometry of the entire bronchial tree, alveolar structure, and vasculature system as well as localization of fluorescent NPs (as surrogate for NM). This study revealed for the first time significant differences in the 3D spatial distribution profile of NPs in intact lungs depending on the route of NP application, namely intratracheal instillation of the NP suspension as bulk liquid or as inhalable aerosol. More specifically, aerosol inhalation displays a uniform distribution pattern in conducting airways (central region) and acini (region of gas exchange; peripheral region) as indicated by a central-to-peripheral (C/P) NP deposition ratio of unity (0.98 ± 0.13). In contrast, instillation of bulk liquid results in a patchy and central deposition profile with a C/P deposition ratio of 1.98 ± 0.37 , indicating that NPs are primarily delivered to and accumulated in the central and proximal bronchioles and acini. Moreover, within the acini NPs were mainly found in the proximal part of acinar region for both inhalation and even more so for instillation. Quantitative analysis of accumulated doses in the different lobes of the lung indicated that the lobe-specific dose was closely related to lobe volume, which is consistent with increasing ventilation with lobe volume.

Secondly, a novel preclinical imaging platform combining two X-ray with three fluorescence imaging techniques was developed and applied for comprehensively unveiling the performance characteristics and underlying mechanisms of the drug delivery process for three commonly used preclinical pulmonary drug delivery routes (intratracheal instillation, ventilator-assisted aerosol inhalation, and nasal aspiration). Propagation-based phase-contrast X-ray imaging (PB-PCXI) allows for *in vivo* time-resolved visualization of the dynamic process of bulk NP-liquid delivery of a mixture of X-ray absorbing substances (*e.g.*, iodine) with fluorescent NPs. For intratracheal instillation secondary aerosol formation associated with blockage of airways and subsequent bursting of the blockage during breathing activity could be identified as mechanism of distributing bulk liquids throughout the lung reaching even the deeper regions of the lung. The process of aerosol inhalation of NPs is more difficult to visualize *in vivo* with PB-PCXI due to low delivery rates and extremely uniform aerosol distribution resulting in low signal-to-noise ratio. However, certain features of the aerosol inhalation process like occasional inadvertent transport of bulk liquid from the trachea into the bronchial region of the lung could be observed, probably resulting from gradual accumulation of liquid aerosols near the exit of the intubation cannula placed in the trachea. Moreover, fluorescence imaging techniques like whole lung or lung slice fluorescent imaging using an epifluorescence imaging (IVIS) or LSM provide quantitative NP dosimetry and qualitative 3D NP distribution pattern throughout the entire lung at multiple resolution scales down to single-cell level, which were in good agreement with those observed with the X-ray imaging methods (*in vivo* PB-PCXI and *ex vivo* CT). The second part of this study thus demonstrates the benefit of utilization of complementary X-ray and fluorescent imaging techniques for *in vivo* time-resolved and *ex vivo* spatially-resolved visualization of pulmonary NP delivery.

In summary, the multimodal imaging platform established here provides unprecedented insights into both pulmonary NP delivery in real-time and 3D distribution, biokinetics, and cellular targeting of NPs at single-cell resolution in intact (non-dissected) mouse lungs. This technology is expected to facilitate optimization of pulmonary NM/NP delivery methods and expedite unraveling of fate and bioactivity of NM/NPs in the lung, which is essential for the development of advanced NM with enhanced targeting efficiency and efficacy for treatment of lung diseases.

1. Introduction

1.1 Nanotechnology in inhalation therapy and toxicology

1.1.1 Nanomedicine

According to the World Health Organization (WHO)¹ lung diseases were amongst the leading causes of mortality worldwide during the past 15 years. In particular, four common respiratory diseases, namely chronic obstructive pulmonary disease (COPD), lung cancer, lower respiratory infections, and tuberculosis, account for 17% of the total of 56.9 million deaths worldwide in 2016 (Figure 1.1) and are projected to cause even 20% of global deaths by 2030¹⁻². Direct application of active components such as interferons, antibiotics, chemotherapeutics, proteins, peptides, and nucleic acids to the lung via aerosol inhalation offers a targeted drug therapy for respiratory diseases. Some of the major advantages of this route are high drug efficacy at the site of disease, limited drug degradation (no stomach or liver processing), and low systemic side effects³⁻⁴. Thus, inhalation therapy has been widely used in patients with COPD, asthma, cystic fibrosis, pulmonary arterial hypertension, and pulmonary infections, but also for the treatment of lung cancer and even systemic diseases like inhalation of insulin as an aerosol to treat diabetes⁵.

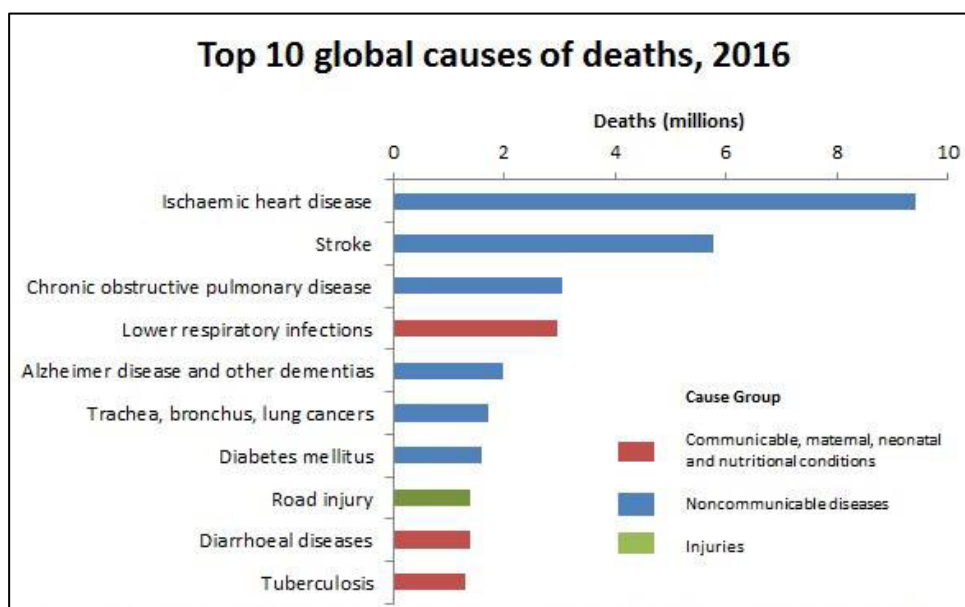


Figure 1.1 Four types of lung diseases are amongst the top 10 causes of mortality worldwide, resulting in about 9.1 million deaths in 2016. Source: WHO, 2018.

The advancement of nanotechnology-enabled drugs (*e.g.*, drug nanocarrier or nanomedicine, NM) exhibits high potential to improve both diagnostic capabilities and therapeutic index by combining the merits of drug carriers (*e.g.*, controlled release, enhanced tissue retention, reduced metabolic degradation, cell-specific targeting) with those of nanometer-sized particles (*e.g.*, reduced phagocytic elimination for particles < 200 nm diameter)⁶. NM or nanocarrier can be defined as “the application of nanotechnology to medicine including the design and use of carrier/conjugate materials at dimensions of 1 to 100 nm for yielding more effective disease diagnosis, disease therapy, and treatment monitoring”⁷⁻⁸. So far, numerous types of nanoparticle (NP) carriers such as liposomes, dendrimers, micelles, polymers, albumin NPs, iron oxide NPs, lipid NPs, and silica NPs encapsulating/conjugating the therapeutic agents have been routinely used in the clinic or are currently undergoing clinical trials (Figure 1.2)⁹⁻¹⁰. Those therapeutic NP platforms have been mainly applied for the

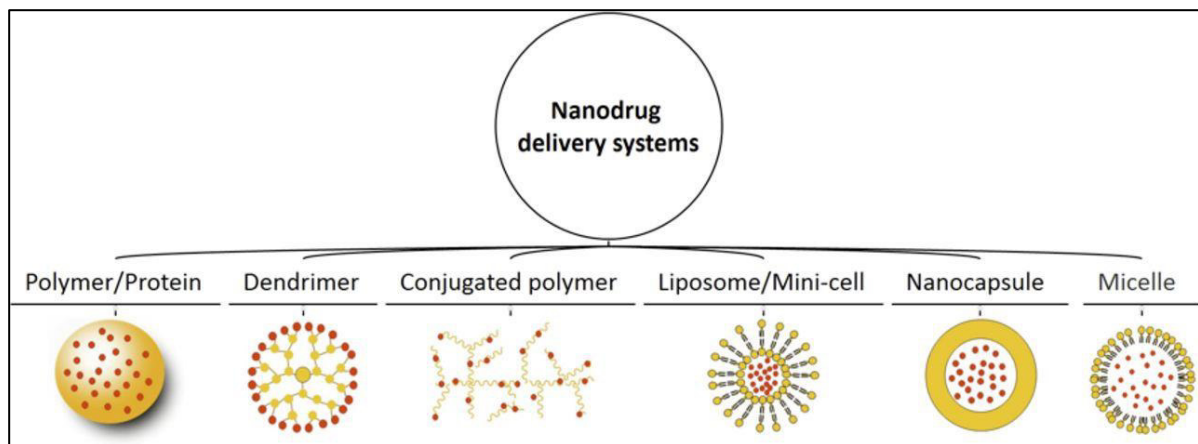


Figure 1.2 A summary of the most common NM formations in routine clinical use or undergoing preclinical/clinical evaluations for lung disease therapy. Red circles refer to therapeutic agents. Reprinted with permission from ref¹⁰, copyright 2019 BMJ Publishing Group Ltd.

diagnosis and treatment of different kinds of cancer like metastatic breast cancer treated with liposomal doxorubicin (Myocet)¹¹. Until now, intravenous administration of novel-designed NM is the primary approach for the treatment of non-small-cell lung cancer (NSCLC), lung carcinoma, and small cell lung cancer (SCLC) in clinics and in clinical trials. However, inhalation therapy for lung cancer treatment has already been frequently carried out in preclinical studies using rodents like mice and rats¹². Moreover, for diagnosis and treatment of lung infections, asthma, and COPD aerosol inhalation of NM was successfully applied in both clinical and preclinical studies^{6, 10}. The physicochemical and theranostic (both

therapeutic and diagnostic) properties of NM depend strongly on a number of factors including chemical composition, size, shape, and density as well as chemistry and functionalization (conjugated ligands, ligand density) of the surface, which represents the interface between NM and tissue (bio-nano interface). Previous scientific efforts have mainly focused on the development of NM formulations with sustained/controlled drug release characteristics to provide prolonged residence time of the drug in the lung, which should improve the local (pulmonary) therapeutic efficacy¹³. For example, inhalation of non-mucoadhesive polystyrene particles (particles do not adhere to mucus) loaded with dexamethasone sodium phosphate provides uniform and prolonged drug release to airway tissue substantially reducing the inflammation in a mouse model of acute lung inflammation¹⁴. Also, for lung infections induced by bacteria such as *Staphylococcus aureus* (*S. aureus*) and *Pseudomonas aeruginosa*, inhaled antibiotics- and phage-loaded particles more effectively targeted infected lung tissue, suppressed infections and mitigated inflammation in a murine model than inhaled free (non-carrier-bound) drugs¹⁵⁻¹⁶.

1.1.2 Nano-biokinetics

To maximize the efficacy of NM, the first fundamental step is to fully understand the fate of NM in the lungs which includes initial pulmonary distribution, retention, clearance, and transport to the bloodstream. For practical reasons this is often studied with nanoparticles (NP; as surrogate NM) in animal models rather than human beings. Understanding the fate of NM in the lung and its relevance for treatment activity, degradation, as well as the possible adverse effects to healthy tissue is even more challenging due to the complexity of biological tissues, inter-subject variability in animal models, and heterogeneity of disease^{8, 17}. Furthermore, deciphering the link between physicochemical characteristics of NPs and associated health effects in the lung is of paramount importance not only for intentionally inhaled synthesized NM but also for incidentally inhaled ambient NPs.

Current knowledge on NP fate in the lung after respiratory application mainly includes initial NP distribution throughout the whole lung from trachea/upper airways via bronchial tree to the alveolar region, fast NP elimination by the mucociliary clearance (within hours), long persistence within the lung, slow clearance by migration of NP-loaded alveolar macrophages to the mucociliary escalator (months to years), and limited translocation across epithelial-endothelial air-blood barrier towards the systemic circulation (Figure 1.3)^{8, 18-20}. More specific, *first* only a small amount of inhaled particles deposited on the epithelium of trachea

or bronchial airways are cleared rapidly by mucociliary transport to the larynx, but most of them remain within epithelial barrier long-term. *Secondly*, for slowly dissolving (biopersistent) micro-sized particles (0.2 – 10 μm diameter) like 1.3 μm alumina-silica particles, 0.5 μm , 2.1 μm , and 3 μm polystyrene latex particles are readily easy to be phagocytized by alveolar macrophages (AMs)²¹⁻²². In contrast, NP such as 20 or 80 nm iridium NP, 20 nm gold NP, 20 nm TiO_2 are thought to experience less uptake by AMs, which enhances their probability to cross the epithelium and relocate into the lung interstitium from which they may gradually and slowly re-entrain back onto the airway epithelium mediated by the (interstitial) macrophages^{19, 23-26}. However, how the role of macrophages in the return of NP to the lung epithelium is not clear. Is this NP-specific phenomenon related to the different types of macrophages *e.g.*, AMs *versus* interstitial macrophages, or tissue-resident macrophages *versus* monocytes-derived macrophages? The *third* fate-related mechanism is clearance of both micro-sized particles and NP from the alveolar region due to slow, long-term macrophage-mediated transport via the mucociliary escalator to the larynx and then passage through the gastrointestinal tract (GIT) with subsequent fecal excretion. *Fourth*, translocation of NP across the air-blood barrier to the systemic circulation followed by accumulation in the secondary organs like the liver, spleen, kidney, and brain is rare, indicating this pathway is a minor clearance mechanism^{20, 25, 27-28}. This translocation mechanism of NP is typically small (<0.1% of total dose), but increases especially for <20 nm NP reaching up to about 10% for 5 nm NP. These phenomena have also been confirmed for humans, but due to technical and ethical limitations the body of evidence mainly consists of animal data²⁸. In summary, the initial site of deposition and size of the (nano-)particles are key players determining the behavior and fate of particles in the lungs.

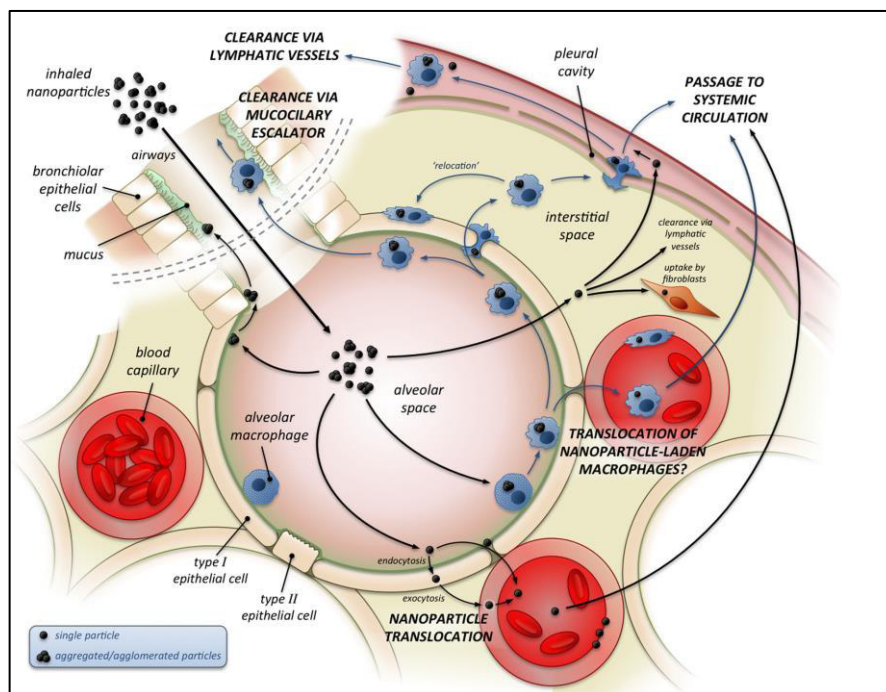


Figure 1.3 The pulmonary biokinetics and fate of NM/NPs deposited in the alveolar region of the lung. Upon deposition of inhaled NPs onto the alveolar lung epithelium, a small portion of NPs can be quickly removed from the bronchial region by the *so-called* mucociliary clearance, while most of (insoluble) NPs deposited in the alveolar region rapidly transport into the interstitial spaces and result in long-term retention. NP reentrainment back onto the alveolar epithelial surface (via an unknown mechanism) for macrophage-mediated transport toward ciliated airways and the larynx was considered as the predominant route for NP clearance in long term. Very few NPs as a free NP or macrophages-loaded NPs could further across endothelial barrier translocating to the blood circulation or lymphatic drainage system. Reproduced from Environmental Health Perspectives (ref.²⁶) with permission from the authors.

However, there is still a debate on the effect of particle size on clearance mechanisms and rates especially if there is a significant difference between micro-sized particles and NPs²⁹⁻³⁰. Most of the data on particle biokinetics were collected either from 2D histomorphological examination in a relatively small number of lung slices (not whole lung data) using confocal microscopy and transmission electron microscopy (TEM) or from radiometric analysis for radiolabeled NPs in different organs/tissues using gamma spectroscopy. Due to the static information in excised tissue slice or organs with limited resolution, those techniques are somehow not able to provide direct and clear evidence to unveil the underlying clearance mechanism of particles, which can be overcome by technological advances in the fields of

TEM, magnetic resonance imaging (MRI), single photon emission computed tomography (SPECT), X-ray based imaging, as well as optical imaging. Among them, optical imaging like super-resolution fluorescent microscopy³¹⁻³², tissue-cleared light sheet fluorescent microscopy (LSFM)¹⁸, and intravital microscopy³³ offers direct evidence for three-dimensional (3D) visualization of particle movement, redistribution, and translocation in real time. There is no doubt that the technical or methodology improvement could enhance our understanding about the particle fate in the biological tissues. In this thesis, application of two novel imaging modalities for visualization of pulmonary delivery and distribution of NPs and their correspondingly novel insights will be discussed.

1.1.3 Dosimetry and Nanotoxicology

Besides their theranostic potential the toxicological profiles of NM or nanocarrier arising from prolonged lung retention should be taken into account during formulation. Epidemiological studies also strongly suggested that inhaled nano-sized ambient particulate matter and/or engineering nanomaterials are associated with enhanced pulmonary and cardiovascular morbidity and mortality³⁴. Accurate dosimetry of delivered NM and NPs in the lung is thus of paramount importance as the administered dose is a critical factor that controls the therapeutic index and health risks³⁵.

For preclinical animal studies different methods for quantitative measurement of NP dose and distribution in the biological tissues have been reported in literature^{7, 36}. The determination of radioactivity in murine tissues such as the lung, liver, spleen, and other organs for radiolabeled NM/NPs using gamma spectroscopy is one of the most common and accurate tools for NP quantification^{19, 24, 27, 37}. Nuclear medicine imaging (SPECT and positron emission tomography (PET)) could offer quantitative information on *in vivo* regional distribution of radiolabeled NM/NPs. Elemental analysis using inductively coupled plasma-mass spectrophotometer (ICP-MS) for metal NPs like silver NPs, gold NPs, iron oxide NPs, and QDs has been broadly used in toxicokinetics and quantification studies³⁸⁻⁴¹. Examined by ICP-MS, inhaled silver NPs were found to be uniformly distributed into all 5 lobes of murine lungs after 1 day or 5 days nose-only aerosol inhalation exposure³⁸. Fluorescence analysis on *ex vivo* lung tissue slice, intact lungs and whole body (*e.g.*, *In Vivo* Imaging System, IVIS, PerkinElmer, USA) provides semiquantitative information on NP dose and biodistribution because of the strong tissue scattering and absorption of imaging light through the thick tissue⁴²⁻⁴⁴. Recently, the development of 3D LSFM offers improved quantification

of fluorophore-labeled NPs in the lungs of mice as it enables whole-organ imaging after tissue clearing, a chemical process that renders tissue optically transparent^{18, 45-46}. Fluorescence quantification analysis of NP dose in lung homogenates is another accurate and effective way to determine the NP total dose, albeit without spatial resolution since homogenization destroys the anatomical structure of the lung completely^{18, 47}. In addition, X-ray based imaging modalities such as synchrotron radiation computed tomography (CT) and phase-contrast X-ray imaging (PCXI) generally allow observation of radio-active aerosol particles in organs of interest and recently they were established for both visualization and quantification of regional distribution and deposition of particles in lungs of rabbits or mice *in vivo*⁴⁸⁻⁴⁹. All of those methods for quantification of NM/NPs in lungs will be described in detail in section 1.3 with particular emphasis on their principle of operation, fields of application, advantages, and limitations.

Due to the unusual physicochemical properties of (engineered) NPs *e.g.*, small particle size, high surface area to mass ratio, varied surface functionalization, low solubility, and different particle shape and the resulting therapeutic and toxic potential of inhaled NM/NP has received much scientific attention in the past two decades (Figure 1.4). The possible adverse effects caused by non-therapeutic inhaled NM/NP have been mainly associated with the cardiovascular system and lung involving acute lung inflammation, oxidative stress, exacerbation of asthma, and promotion of lung fibrosis and lung cancer⁵⁰⁻⁵². There is mounting evidence that these adverse health effects are driven by effects occurring at the nano-bio interface, which is best described by the surface area of the NP. For instance, acute lung inflammation characterized by enhanced polymorphonuclear neutrophils (PMNs) influx into the lung of mice after intratracheal NP instillation was observed for six kinds of carbonaceous⁵³ and two types of TiO₂⁵⁴ NPs independent particle size (for NPs from 10-250 nm), if surface area – not mass or number – was chosen as dose metric⁵⁵. A retrospective analysis of acute inflammation in rodents due to exposure to 5 types of nanomaterials with widely varying chemical composition and particle size, surface area dose was further confirmed as the biologically most relevant dose metric for spherical, biopersistent NPs in comparison to the other dose metrics like delivered mass, volume or particle number⁵⁰. Moreover, pulmonary instilled multi-walled carbon nanotubes contributed to the development of malignant mesothelioma and lung alveolar cell tumors in rodent models⁵⁶ and accumulation of inhaled gold NPs was found at the vascular site of disease in both animal models and humans corroborating the epidemiologic finding that (nano-)particle exposure is

related to cardiovascular effects ⁵⁷. Recently, extensive scientific evidence suggests that ambient or engineering inhaled nanomaterials could exacerbate non-pulmonary diseases such as breast cancer metastasis ⁵⁸ and reactivation of latent viruses in the lung ⁵⁹. Nowadays, many new types of NM/NP with/without surface coating have been synthesized and used not only in different research labs but also in nano-enabled industrial products. Hence, it essential albeit difficult to understand their respective health risks. Current risk assessment approaches include “read-across” and “hazard classification” strategies, which aim to inter-/extrapolate from the known toxicity for selected key nanomaterials like metal oxide and carbonaceous NPs, fiber-like NPs (*e.g.*, carbon or cellulose nanofibers-/tubes) and so-called two-dimensional nanomaterials (*e.g.*, graphene) to complex, multi-component nanomaterials ⁵⁰. To this end, scientists are seeking to establish comprehensive, integrated and standardized protocols for both *in vitro* methodologies ranging from NP synthesis/generation, characterization, and insoluble NP dispersion to dosimetry and NP-cell culture exposure model and *in vivo* approaches consisting of NP dose quantification, NP exposure to animal model, and unified toxicological endpoints ⁶⁰⁻⁶².

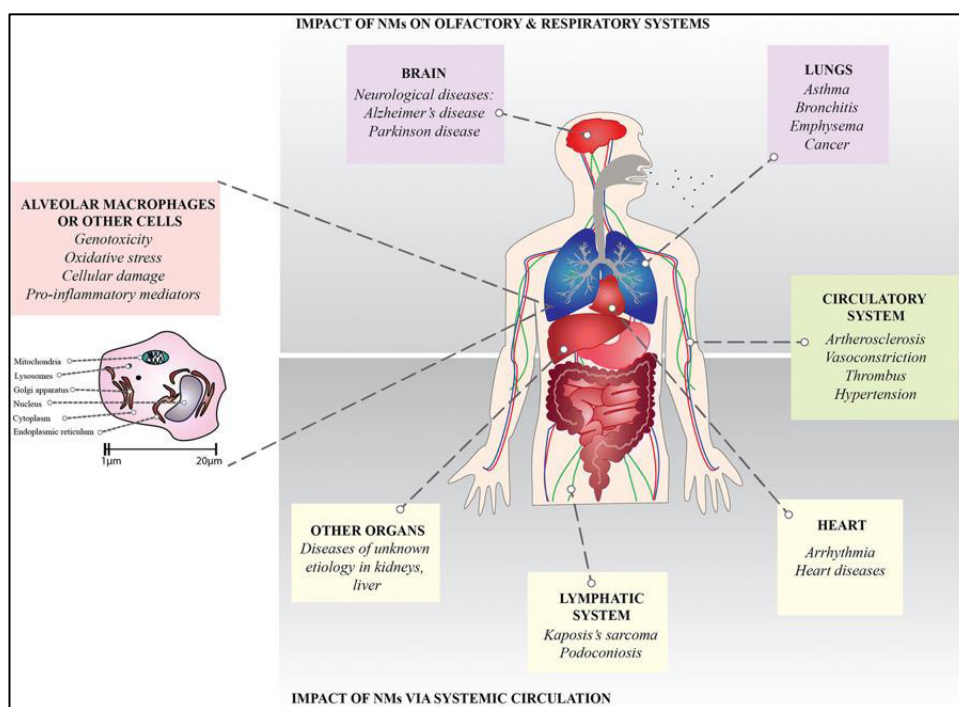


Figure 1.4 The potential health effects after inhalation exposure of NM/NPs. Following inhalation, NPs persistently accumulate in the lung and a small part of NP could translocate to other organs including the liver, kidney, and brain via air-blood barrier (or the olfactory bulb), which are associated with a range of disease states in the pulmonary and non-

pulmonary organs/tissues. Reprinted under the terms of the Creative Commons CC BY license, ref.⁶² copyright 2018, the authors, published by Springer Nature.

1.2 Application routes of pulmonary delivery

It is well known that different application routes result in different spatial deposition and distribution profiles of NM or NPs in the respiratory tract leading to differences in their fate and bioactivity. Various pulmonary delivery routes/devices in both clinical and preclinical settings are introduced here.

1.2.1 Clinical pulmonary delivery routes/devices

In clinical practice, the most commonly used aerosol drug delivery devices are nebulizers, pressurized metered-dose inhalers (pMDIs), and dry powder inhalers (DPIs)⁴. Recent developments in inhalation technology have focused on improved aerosolization performance, therapeutic efficacy and patient adherence.

Nebulizers

Nebulizers are devices that convert a liquid suspension or solution into small aerosol droplets. Three types of nebulizers, namely jet nebulizers, ultrasonic nebulizers, and vibrating mesh nebulizers, are currently in clinical use, which utilize the expansion of compressed gas, acoustic waves or piezoelectrically driven vibration of a porous membrane, respectively, to break up liquid formulations into small droplets (aerosols). In spite of relatively low cost, the widely used jet nebulizers often require relatively long inhalation times and are associated with poor delivery efficiency, leading to a large time burden for the patients and significant waste of expensive medications. A number of factors such as variations in the nebulizer design, energy source, connecting tubing, gas flow and pressure, adopted interface (spacers and mouthpiece or facemask), and the breathing pattern of patients contribute to the large variabilities in nebulizer performance. Ultrasonic nebulizers generate sound waves by vibrating a piezoelectric crystal at high frequency (>1 MHz), which forms standing waves at the surface of the drug solution resulting into crests that burst into droplets. The conventional models of ultrasonic nebulizers have restricted portability, are costly and inefficient in nebulizing some drug suspension, liposomes, and highly viscous solutions. Recently, vibrating-mesh nebulizer has gained much attention due to their portability, faster rate of nebulization, shorter treatment time, and minimal residual volume, leading to higher lung deposited dose, as compared to jet or ultrasonic nebulizers. The integration of software to

control drug output and inspiratory flow, breathing frequency, and inspiratory time has greatly improved efficiency and repeatability of drug delivery. For example, the AKITA[®] system consists of a stand-alone SmartCard electronic control unit with an air compressor, which is coupled either with a jet nebulizer or a mesh nebulizer (AKITA[®] APIXNEB)⁶³. The technology even enables targeted delivery of drugs to certain regions of the lung by controlling the aerosol flow rate, delivery (tidal) volume, and timing of nebulization (optimize aerosol release at specific period during the inhalation phase of a patient)⁶⁴. I-Neb[®] uses a vibrating mesh nebulizer and an adaptive aerosol delivery (AAD) software control unit that combined into a single handheld device to control drug delivery⁶⁵. In addition to accurate and efficient dosing, other favorable properties of the I-neb are the provision of feedback to the patient on dose completion along with details of each treatment. These data can be transmitted via a modem to a remote location, which enables continuing assessment of adherence of the patient to the drug regimen⁴ – one of the most promising eHealth applications in inhalation therapy.

Pressurised metered-dose inhalers (pMDIs)

pMDIs are the most widely used inhalation devices for the treatment of COPD and asthma and other respiratory diseases. They are convenient, portable, multiple-use inhalers that deliver a specific (metered) dose of aerosolized medications to the lung. pMDIs consist of several key components: a canister where the active substance formulated with propellant, a metering valve enables the generation of a metered quantity of aerosolized medications with each actuation, an actuator connects the metering valve to an atomization nozzle, and a mouthpiece⁶⁶. This technology from the 1960s has essentially been unchanged except for the transition of pMDIs from chlorofluorocarbons (CFCs) to hydrofluoroalkanes (HFAs) as propellants. Many patients experience problems in coordinating activation of the device actuation with the required inhalation maneuver, resulting in inefficient and highly variable drug delivery, sub-optimal disease control, and repeated use of inhalers. Breath-actuated pMDIs (*i.e.*, Easibreathe, IVAX, Miami, FL, USA) and add-on devices such as spacers and valved holding chambers have been developed to address those issues. Implementation of a dose counter on the new pMDIs could further improve adherence by continuous monitoring of drug use.

Dry powder inhalers (DPIs)

DPIs are devices that deliver medications to the lung in the form of a dry powder. Traditional asthma and COPD therapy with drugs such as β -agonists, corticosteroids, bronchodilators, steroids, mast cell stabilizers, and anticholinergic agents have been primarily applied by pMDIs⁶⁷. Because of the environmental concern of CFCs propellants and inherent limitations of pMDIs, DPIs are gradually wider use as one of the effective alternatives to the pMDIs. Another advantage of DPIs is that the drug is released automatically during the inhalation phase of the patient, *i.e.*, inhalation maneuver and activation of the DPI do not have to be actively coordinated (as for the pDMA).

Most often clinically used DPIs can be characterized as “passive” inhalers as they are breath-actuated which require moderate inspiratory effort to absorb the drug formation from the device⁶⁸. The aerosolization performance of DPIs depends on both the formulation and the geometry of the air path in the device. The amount of drug powder deposited to the lung is thus dominated by a number of factors including the airflow rate, inhaler resistance, inertial impaction, particle (de)-agglomeration. Another type of DPIs is the “active” device that incorporates vibrating piezoelectric crystals or battery-driven impellers that eliminate the need for the patient to generate a high inspiratory flow rate, an advantage for many patients, particularly infants and elderly patients with severe COPD. DPIs can be generally grouped into 4 groups: single-use, reusable single dose, multi-dose reservoir, and multi-unit devices. The selection of a device will be dependent on the type of diseases, particle powder properties, effective delivered dose, and dosing frequency³.

1.2.2 Preclinical pulmonary delivery routes/devices

In preclinical pulmonary drug delivery studies, a large number of animal species like rodents, guinea pigs, rabbits, dogs, sheep, monkeys, and non-human primates have been relied upon for investigating the absorption, distribution, and pharmacokinetics of drugs in the lung⁶⁹. Anatomical and morphologic differences between the extrathoracic respiratory tract (*e.g.*, nasal and nasopharyngeal cavity) and the pulmonary respiratory tract (trachea, bronchi, and lung) should be taken into consideration when selecting an animal model for pharmaceutical or toxicological evaluation of drugs in the lungs⁷⁰. Small animals such as mice are particularly important and most widely used due to their small body size (low space requirement in animal facility and low cost), high reproductive rate (can be used in large numbers), mature genetic manipulation background (mechanism-specific gene knock-out/knock-in models), *etc.* as compared to large animal models. The method of pulmonary

administration is a key factor in determining the amount of delivered dose and regional distribution of applied medications/particles and will greatly impact on the therapeutic/toxicological outcomes. Medications/particles can be delivered to the lungs via spontaneous inhalation (whole-body, head-only, and nose-only exposure), intranasal and oropharyngeal aspiration (drop of liquid placed on the nostrils and larynx), or direct administration methods that bypass the upper respiratory tract (*e.g.*, intratracheal instillation or inhalation).

Passive delivery

Aerosolized drug generated from liquid suspensions/solutions or dry powder formulations can be delivered to the conscious animals by passive inhalation in sealed chambers that allows for whole-body, head only, or nose-only exposure. The merits of whole-body inhalation system are convenient to use, no restraint to experimental animals, and limited experimental artifacts. However, only a small amount of applied aerosols can be reached to the animals ($\sim 0.1\%$) and even less to the lung ($\sim 0.01\%$) since a substantial loss of aerosol will be deposited to the animal's fur and on the exposure chamber and tubing⁷¹. Drug absorption via oral and gastrointestinal further makes the assessment of actual deposited dose difficult. Additionally, significant inter-individual differences in deposited dose might be expected as variations in animal lung capacity, body size, and breathing parameters. Head-only or nose-only inhalation system could effectively eliminate the non-pulmonary absorption of drugs and thus increase the potential delivered dose to the lungs. Although nose-only exposure is more physiologically relevant, large number of aerosols are deposited in the nasal cavity that eventually is transported to GIT by means of mucociliary clearance⁷². Other limitations of nose-only or head-only system are that animals are fixed in a defined position under stress, the system may generate heat, animals may get suffocated in the chamber, and require intensive labor⁷³. Nevertheless, there are a few commercialized nose-only inhalation systems available like TSE GmbH (Badhamburg, Germany), Intox Products (Edgewood, NM), CH Technologies (Westwood, NJ), and ADG Developments (Herts, UK) and some more custom-designed aerosol chamber described in the literature^{71, 74}. For example, a nose only exposure inhalation system (manufactured by CH Technologies Inc, Westwood, NJ) with five ports connected to the nose of each mouse has been used for the treatment of lung cancer⁷⁵. A popular design for nose-only inhalation system is that the cylindrical chamber with animal port located around the central chamber and test atmosphere enters from the top and reaches individual animal port via a tube (Figure 1.5).

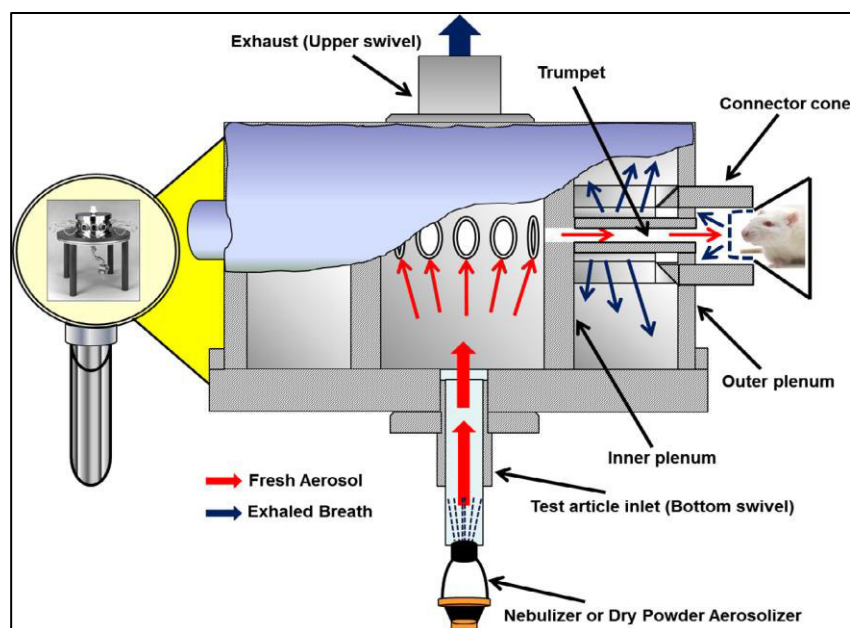


Figure 1.5 Schematic diagram of exposure chambers used for nose-only exposure of drug/formulation to rodents. Reprinted from permission ref.⁷³ copyright 2013 Elsevier B.V. All rights reserved.

Direct administration methods

Direct administration methods consist of intratracheal liquid instillation, spray instillation, and dry powder insufflation. The main advantages are that they permit controlled delivery of a specific dose to the lung and accurate measurement of the deposited dose, as well as circumvent oropharyngeal or nasopharyngeal deposition. The application is performed by intratracheal inserting a cannula in the trachea of an animal model under light sedation or anesthesia⁷⁶. The liquid instillation delivers drug suspension/solution in the form of liquid bolus to the lung by emptying the syringe (tightly connected to the intratracheal inserted cannula) within 1 second⁷⁷. Instead of liquid bolus application, spray instillation and dry powder instillation deliver drugs in the form of aerosolized droplets or particles proxy to the true aerosol⁷³. Intratracheal application using spray/aerosol devices like the MicroSprayer® Aerosolizer and Dry Powder Insufflator™ (Penn-Century Inc., US) allows for rapid and reliable delivery a specific amount of drug directly to the lungs, which has been widely used in delivering antibiotics, antibodies, antiproteases, chemotherapy, proteins and peptides, NPs and many more⁶⁹. It should be noted however that this direct administration method is not representative of the spontaneously breathing process as the drug suspension/solution is forced into the airways while the animal is under anesthesia. This method could potentially induce significant stress and inflammation in the subject due to the insertion of an extra

cannula inside the trachea. Repeated administrations to a single animal are thus not recommended. Additionally, the forced instillation process could prevent the homogenous distribution of liquid/aerosol/particle throughout the lung and a small portion but unknown amount of the drug may be coughed up or swallowed.

Ventilator-assisted aerosol inhalation

A refined version of the administration method compared to the spray instillation is the ventilator-assisted aerosol inhalation. This aerosol delivery system includes the tracheal intubation, mechanical ventilation, and liquid nebulization⁷⁸. Briefly, the mechanical ventilator (flexiVent system, SciReeq Inc., Canada) equipped with a nebulizer (Aeroneb Lab, small droplet diameter (2.5–4.0 μm), Aerogen Inc., Ireland), where the liquid aerosol droplets are generated and transported through the intratracheal intubated cannula to the mouse airways¹⁸. This system allows for precisely controlling mouse respiration during aerosol inhalation. As compared to the liquid bolus or spray instillation, this method mimics the realistic physiology inhalation process and provides uniform distribution throughout the lung, but requires relative long anesthesia time (tens of seconds to 1-3 minutes depending on the nebulized volume and output rate, *etc.*). Although it enables a relatively high ratio of applied dose deposited to the lung, the distribution pattern of this method in mechanically ventilated, deeply anesthetized mice might be different for that of using head-only or nose-only inhalation system in spontaneously breathing or more mildly anesthetized mice.

Intranasal and oropharyngeal aspiration

In certain experimental scenarios, intranasal aspiration and oropharyngeal aspiration can be used as alternative methods for pulmonary drug delivery studies because of their easy application, analogous inhalation process, and high deposited dose. Both methods are performed on the mild anesthetized mouse kept in a vertical position. Intranasal aspiration refers to that a liquid is dropped on a nostril of mouse using the micropipette and is quickly aspirated in the respiratory airways during breathing. It has been shown that small volume of applied liquid (5-10 μL per nostril) via intranasal delivery is limited to the nasal cavity but the use of large volume (25-50 μL per nostril) resulted in deeper deposition of liquid in the upper airways⁷⁹. The difference for oropharyngeal aspiration is that the liquid is deposited on the top of pharynx which can be directly aspirated to the lung during the next inhalation bypassing the upper respiratory tract, as compared to intranasal aspiration. This former dosing approach is generally applied for the generation of murine disease models (like

bleomycin-induced lung fibrosis⁸⁰ and chemically induced asthma⁸¹). Recent evidence suggests that the distribution profile of drugs delivered by oropharyngeal aspiration is similar to that of delivered by MicroSprayer® aerosolizer instillation, in spite of the latter possesses a longer overall process and deeper anesthetic regimes^{70, 82}.

In the study, we have determined the characteristics and mechanisms of pulmonary delivery and distribution for 5 commonly used means of pulmonary application mentioned above namely nose-only inhalation, intranasal and oropharyngeal aspiration, intratracheal instillation, and ventilator-assisted aerosol inhalation, but a specific focus will be on the latter two.

1.3 Imaging tools to assess the pulmonary delivery and distribution

To better understand the drug efficacy and biological effects of NM/NPs in the animal lungs, a key component in pulmonary drug delivery is determining their delivery and fate including the (re-)distribution, translocation, elimination, and bioactivity *in vivo*. A range of noninvasive imaging techniques is therefore used for qualitatively evaluating regional lung distribution of drugs, consisting of nuclear medicine imaging (SPECT and PET), MRI, X-ray based imaging (PCXI and CT), and *in vivo* optical imaging. Another imaging method for clinical routine use is the ultrasound imaging, which is not suitable for visualization of particle deposition in the lung because of the poor propagation of sound waves in the tissue-air interface. Taking advantage of optical imaging with wider selection at near-infrared region (NIR) of the spectrum and high resolution of ultrasound detection, photoacoustic (PA) imaging is a noninvasively novel modality that offers anatomical and dynamic information on deep-seated fluorescent agents *in vivo*⁸³. However, it faces the same challenge as ultrasound imaging when it applies to the lung. Consequently, limited by their restricted light penetration depth, low sensitivity, and quantification ability, PA and ultrasound imaging are not sufficient for investigating the NM/NPs distribution and pharmacokinetics in the lungs. Here, we therefore provide an introduction to these noninvasive imaging techniques suitable for the lungs and address their various features in pulmonary drug delivery research.

1.3.1 Nuclear medical imaging

Gamma scintigraphy is the traditionally most relevant and standardized 2D imaging method, offering robust results in fundamental evaluation of the drug deposition and clearance in the lungs of humans after administration using different devices or formulations⁸⁴. Recently,

SPECT and PET are growing in popularity due to the 3D information provided on the regional distribution of particles in the lung and the ability to differentiate between the large and small airway⁸⁵. To adopt these imaging modalities from clinical systems to preclinical study, a significant improvement in spatial resolution offered by advanced instruments suitable for large and small animals like micro-SPECT or micro-PET has been adapted⁸⁶. Generally, in gamma scintigraphy and SPECT, they require radiolabeled agents that radionuclide like ^{99m}Tc, ¹¹¹In, ¹²³I, and ⁶⁷Ga should be added/conjugated to the drug/particles prior to administration⁸⁷. One thus has to consider and validate the radiolabeling stability and the conservation of formulations in biological tissue before pulmonary application since any degradation or separation of radionuclides with drugs/particles will give misleading distribution information. By contrast, PET imaging avoids the degradation/separation issue due to the incorporation of positron emitters such as ¹¹C and ¹⁸F directly into the formulations. The major merits of PET and SPECT are the high signal-to-noise ratio, high penetration depth, and sufficient quantification accuracy. A number of studies have thus applied them to visualize the radiolabeled agents delivered to relative large animals not only because of the accurate information on deposited dose, regional distribution, biokinetics of inhaled radiotracers, but also the functional imaging of physiologic and biologic processes⁸⁸. However, no anatomical information can be collected, high cost, limited spatial resolution, requirement of radiolabeling process, and complexity in data interpretation, are making them relatively high inaccessibility in some pulmonary studies. Additionally, those approaches are mainly useful for imaging the lung distribution of drug/particles in humans and relative large animals instead of small animals like mice.

1.3.2 MRI

Above described nuclear medical imaging requires the use of isotopes that have some drawbacks such as specialized training in labeling process and high radiation dose. Those issues can be addressed by using MRI, which is one of the safest methods among all of the noninvasive imaging techniques. MRI is based on Nuclear Magnetic Resonance (NMR) phenomenon that a powerful external magnetic field that forces protons (hydrogen nuclei) in the body to align with the field. Images in 2D or 3D are generated from the signal obtained from nuclei within different tissues or contrast agents return to their equilibrium state (*i.e.*, relax) at different rates after perturbing by the radiofrequency pulses⁸⁹. Beside the wide application of MRI with or without contrast agents in lung physiology and diseases such as lung perfusion, lung fibrosis, pulmonary edema, and tumors⁸⁹⁻⁹⁰, it is also particularly useful

for evaluating the regional distribution and bioactivity of NM/NP (iron oxide NP) in the lung and other organs of small animals like mice and rats^{7,91}. The major advantages of MRI are that it allows the acquirement of relatively high-resolution image (pixel size: 10-100 μm), and better lung tissue contrast, no involvement of ionizing radiation as compared to nuclear imaging. However, the MRI is costly and has slow acquisition speed which is unable to capture the real-time dynamic delivery of NP suspension/solution in the lungs. It also requires incorporation of high amounts of contrast agents into the NP formulations because of the poor sensitivity⁹².

1.3.3 X-ray based imaging

Medical X-ray based imaging techniques possess fast image acquisition and high penetration ability in biological tissue by utilizing photons with wavelengths ranging from 10^{-2} to 10^1 nm, which are much shorter than that of visible and ultraviolet light. According to their varied attenuation efficiency, biological tissues such as soft tissue (*e.g.*, the lung) and hard tissue (*e.g.*, the bone) imaged by conventional planar X-ray imaging produce different absorption images in grayscale⁸⁹. By introducing a short gap between the detector and the object, phase-contrast X-ray imaging (PBXI) allows for simultaneous detection of both phase shift and absorption of X-rays, resulting in a more crisp depiction of lung and surrounding tissue structure. Images with X-ray based approaches can be obtained with or without contrast agents. Generally, addition of contrast agents could increase the methodological sensitivity to visualize and differentiate among different tissues. Substances with a high atomic number or density like iodine- or barium-, gold-, and lanthanide-based compounds are preferably applied X-ray contrast agents, which efficiently attenuate external X-rays. Planar PBXI has been largely used to study the pulmonary liquid delivery dynamics with high temporal resolution *in vivo* (Figure 1.6)⁹³ and micro-particle clearance via mucociliary transport in the *ex vivo* trachea of animal models⁹⁴. CT (or Micro-CT suitable for small animals like rats and mice) enables high-resolution observation of the lung anatomy like the vasculature system and acini⁹⁵, and *in vivo* real-time 3D visualization of biodistribution of NM/NPs with incorporation of contrast agents⁹². Numerous NM formulations such as liposomes, polymer-coated NPs, micelles, and dendrimers have thus been applied to determine their biodistribution in different organs and targeting effects in the tumor of various animal models by using CT. However, there is scarce information on pulmonary NP delivery and distribution imaged by X-ray based imaging modalities. Taken together, the merits of X-ray methods are that they allow for rapid acquisition of an image (within 100 ms) co-localizing active tracers

and anatomical structure, low cost, and high spatial resolution (pixel size: 30 μm)⁸⁹. The major limitations of X-ray methods include poor sensitivity and thus requiring high contrast agent loading into formulations and high ionizing radiation dose, and its inability to assess drug efficacy.

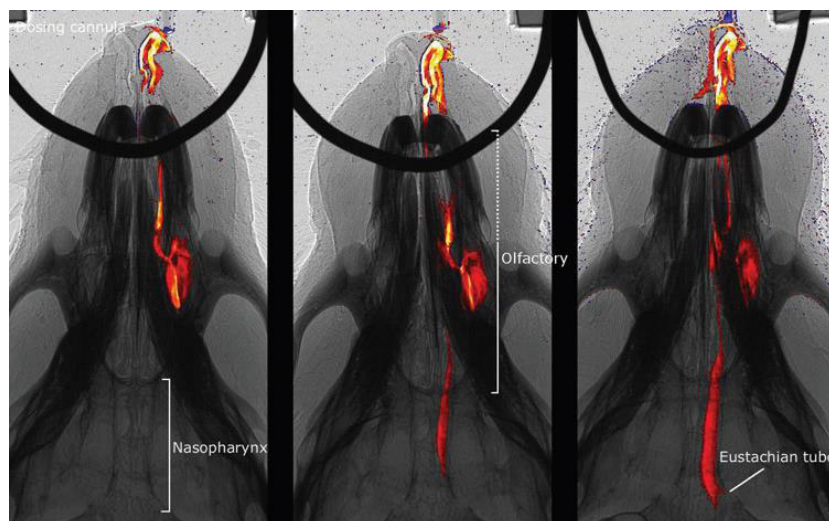


Figure 1.6 Nasal bolus dosing delivery imaged by synchrotron phase-contrast X-ray imaging with different volumes of iodine-based contrast fluid (from left to right 4 μL , 10 μL , and 20 μL). Reprinted from ref.⁹³ Copyright 2013, Mary Ann Liebert, Inc.

1.3.4 Optical imaging

In vivo optical imaging has been mainly carried out to visualize the biodistribution of NPs in living animals and in *ex vivo* organs and tissues by utilizing *e.g.*, the IVIS and fluorescent molecular tomography (FMT). It is very simple to conduct, low cost and no radiation risks, multiple time-points imaging. Optical imaging is based on the principle that exciting by a specific filtered light the fluorophores such as fluorescent proteins, dyes, and particles emit a longer wavelength of light that detected by a charge-coupled device (CCD) camera. Generally speaking, the lower penetration depth of light (*i.e.*, photon), strong light scattering and absorption in biological tissue are the major problems correlated with *in vivo* whole animal imaging. Fluorophores with longer emissions at the NIR (600-1000 nm) or even at NIR-II region (1000-1700 nm) are thus selected to be used to *in vivo* optical imaging due to the substantially reduced tissue light scattering and absorption as well as much lower tissue autofluorescence. The technique also has lower spatial resolution that only enables determination of NP biodistribution at the whole tissue/organ level without any detailed anatomical information as compared to CT or MRI. For instance, a general particle distribution in mouse lung was scanned by FMT demonstrated that the distribution uniformity

and deepness of dry powder particles delivered by using an aerosol generator was better than that of the use of Penn-Century insufflator (Figure 1.7) ⁹⁶. To further overcome the limitations of optical imaging, several studies have been performed on *ex vivo* lung samples that the qualitative and quantitative distribution of fluorescence-labelled NPs after intratracheal instillation and aerosol inhalation delivery can be obtained by using lung-slice fluorescence imaging namely the lung was embedded, cut into thin slices and imaged consecutively ⁴²⁻⁴⁴.

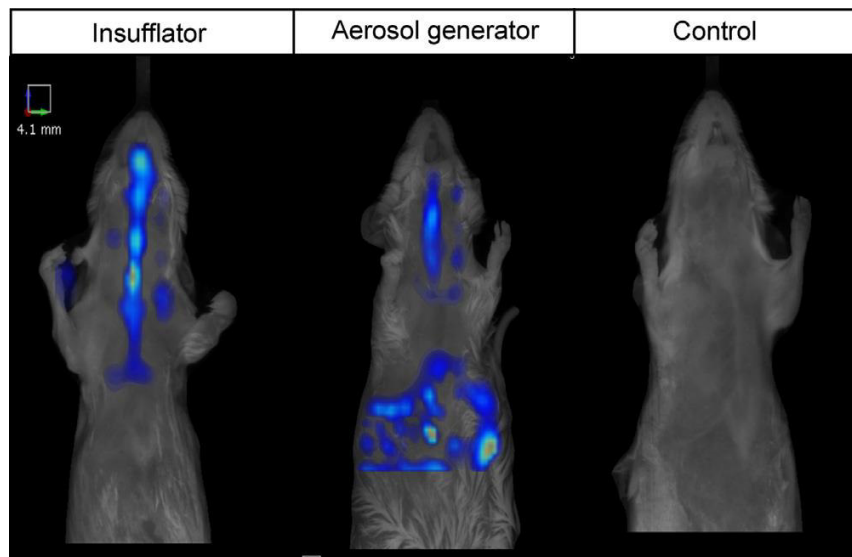


Figure 1.7 Typical FMT-images after pulmonary administration of the powder via the Penn-Century insufflator (left), via the aerosol generator (middle), or control (no powder administration) (right). Reprinted from permission ref.⁹⁶ copyright 2014 Elsevier B.V. All rights reserved.

1.3.5 Hybrid lung imaging

Since each of the imaging modalities mentioned above has its own strengths and weaknesses, multimodal hybrid imaging tools such as PET-CT, SPECT-MRI, and FMT-CT⁹⁷ are increasingly used as they provide deeper insight into targeting and distribution profile of NM/NPs in terms of anatomical information, detection sensitivity, and spatially resolved dosimetry ⁷. For instance, a hybrid FMT-CT imaging method was successfully used to monitor lung tumor size and growth with a fluorescence probe ($\alpha\text{v}\beta 3$ integrin–targeting IntegriSense 680) in a *Kras* mouse model ⁹⁸. Simultaneous anatomical and functional imaging of tumor with a radiotracer [¹⁸F]-2-fluoro-2-deoxy-D-glucose captured by *in vivo* PET and MRI provide accurate tumor volume and growth information ⁹⁹. Moreover, SPECT/PET-CT systems have also broadly applied to image the targeting and therapeutic

efficacy of NM in tumor xenografts in animal models like intravenous administration of liposomal doxorubicin to squamous cell carcinoma xenografts ¹⁰⁰ and peptide-coupled polymeric micelles to prostate cancer xenografts ¹⁰¹, which present clear evidence on the effective accumulation of NM to the tumor. However, multimodality imaging approaches for deciphering the pulmonary drug delivery are still largely unexplored, albeit many delivery strategies have been designed to targeted delivery of NM/NPs to lung tumors via intravenous or subcutaneous injection ⁷. Another very important aspect for the development of multimodal imaging is to formulate the robust contrast agents suitable for various imaging methods. NP systems offer several advantages due to the porous structure that allows incorporation of contrast agents, specific surface ligands enhancing cellular targeting, and the small size enables a higher amount loading of contrast agents as compared to conventional bulk systems. Examples consist of quantum dots (QDs) and iron oxide NPs incorporated lipoproteins ¹⁰², paramagnetic-coated fluorescent QDs ¹⁰³, paramagnetic and fluorescent liposomes ¹⁰⁴, and magnetic nanocrystals- and fluorescent agents-coated antibodies ¹⁰⁵. These NP systems could further be designed with radionuclides for PET and SPECT imaging.

2. Aim of this study

Understanding the dynamic process of pulmonary drug delivery in the context of dose, distribution, biokinetics, and bioactivity of NM/NPs with cellular resolution is essential for both maximizing therapeutic efficacy of NM and minimizing health hazards of NPs. Currently available preclinical imaging tools for animal models are unable to visualize NM/NPs distribution in nondissected whole lungs with cellular resolution. Moreover, commonly used *ex vivo* NP detection/dosimetry assays such as 2D stereological methods, flow cytometry, TEM, and ICP-MS do not preserve 3D anatomical information.

The overall objective of this study to facilitate the development of novel, more effective NM by providing new insights into pulmonary delivery and biokinetics of NM/NP in the lung. This will be accomplished by establishing, validating and applying a multi-modal imaging platform for real-time *in vivo* visualization of pulmonary NM/NP delivery and *ex vivo* three dimensional co-mapping of NP distribution and lung morphology in non-dissected murine lungs with cellular resolution for providing new insights into pulmonary delivery and biokinetics of NM/NPs in the lung.

The first goal of this study is therefore to develop an *ex vivo* imaging method that allows for visualization of the spatial localization of nanoparticles (NPs) as surrogate for nanomedicine (NM) with cellular resolution and accurate dosimetry of NP distribution in entire *murine* lungs. To this end, optical tissue clearing on *ex vivo* murine lung using a modified 3DISCO protocol is performed, which renders the lung tissue transparent. Subsequently, the nondissected whole lung is imaged with light sheet fluorescence microscopy (LSFM). Leveraging tissue autofluorescence in the green channel (*i.e.*, 480 nm) and NPs with a red fluorescence label- (*i.e.*, 640 nm), this imaging modality (*ex vivo* tissue-cleared LSFM) was established for quantitative 3D co-mapping of (label-free) lung morphology and biodistribution of NPs in whole murine lungs. The next goal of this study is to combine *ex vivo* tissue-cleared LSFM (and some other fluorescence imaging modalities) with *in vivo* propagation-based PCXI (PB-PCXI) to comprehensively decipher the characteristics and mechanisms of different pulmonary NP delivery routes in the context of delivery dynamics, regional distribution, dosimetry, and cellular localization. The Munich Compact Light Source (MuCLS) was used to produce a sufficiently coherent high energy X-ray beam to obtain time-resolved (ca. 1 Hz) edge-enhanced *in vivo* images of the nasal cavity or the lung via propagation-based PB-PCXI during the process of application of NPs acting as contrast agent

¹⁰⁶. Combined with *ex vivo* CT and epifluorescence imaging of the whole and sliced lung this multimodal imaging platform has unveiled the mechanisms and specific features of the process of pulmonary drug delivery and spatial distribution profile of NPs throughout murine lungs down to cellular resolution for three widely used pulmonary application routes in preclinical research, namely nasal aspiration, intratracheal instillation, and ventilator-assisted aerosol inhalation.

3. Materials and methods

All the experimental substances and methods described here can be found in the attached two publications in detail (PRP1 and PRP2).

3.1 Materials

Since two imaging modalities (X-ray based imaging and fluorescent imaging) were applied in this study, it requires the use of substances with specific X-ray absorbing or fluoroactivity. For X-ray based imaging modalities (PB-PCXI and CT), an iodine-based contrast agent (370 mg/ml, Ultravist-370) and three kinds of metal particles were used, namely Roti®-MagBeads (iron oxide magnetic particles, volume median diameter (VMD): 893 nm, 10 mg/mL, Carl Roth GmbH, Karlsruhe, Germany), gold NPs (VMD: 20 nm), and Qdot 800 ITK™ carboxyl quantum dots (QDs emission at 800 nm; VMD: 18nm, Invitrogen, Ltd., Paisley, UK).

For fluorescence-based imaging, polystyrene NPs with the embedded fluorescent dye SkyBlue (excitation/emission (ex/em) =670 nm/710 nm; VMD: 480 nm; 10 mg/mL; Kisker Biotech GmbH, Steinfurt, Germany), melamine resin fluorescence (MF) NPs (ex/em= 636 nm/686 nm; VMD: 498 nm, 25mg/mL, microParticles GmbH, Berlin, Germany), and QDs were used. Gold NPs were synthesized in the lab and all the other materials are purchased from the respective company.

3.2 Size measurement of particle suspensions

Hydrodynamic diameter measurements of all particle suspensions were carried out with dynamic light scattering (DLS) using a Malvern Zeta Sizer Nano instrument (Malvern Instruments Ltd., Malvern, UK) (PRP1 Figure S2 and PRP2 Figure S1). It is noteworthy that the enhancement of approximately 50% in VMD of melamine and polystyrene NPs (from about 480 nm to 770 nm) when transferring them from water to iodine solution (PRP2, Figure S1) possibly results from the agglomeration induced by iodine suspension, while the NP fluorescence signal was not affected and remained stable for more than a week after mixing (PRP2, Figure S3).

3.3 Animal handling and methods of pulmonary substance delivery

Wildtype C57BL/6 mice (female and male, age 9-25 weeks, 19-30 g) were housed in individually ventilated cages (IVC-Racks; Bio-Zone, Margate, UK) supplied with filtered air in a 12-h light/12-h dark cycle. Mice were provided with food (standard chow) and water ad

libitum. All procedures involving animal handling and experiments were performed in accordance with protocols approved by the Regierung von Oberbayern (District Government of Upper Bavaria, AZ55.2–1-54-2532-108.13). After various means of pulmonary delivery (details in the following sections), mice were sacrificed immediately by exsanguination and transcidentally perfused and the mouse lungs were excised and dried and inflated or optically cleared and 3D imaging using LSFM.

3.3.1 Regular intratracheal instillation (PRP1)

As previous description⁷⁷, animals were intubated by a nonsurgical technique using a 20G cannula intratracheal inserted into the trachea after mice were anesthetized using a mixture of ketamine and xylazine via the intraperitoneal injection. Mice were kept in a horizontal position and a 50 μ L NP suspension with different concentrations for each type of NPs was quickly instilled via the syringe through the cannula to the lung (the whole instillation process occurs within 1 s and it thus has a delivery rate of $>50 \mu\text{l/s}$).

3.3.2 Ventilator-assisted aerosol inhalation 1.0 (PRP1)

Animals were deeply anesthetized by intraperitoneal injection with a triple combination of midazolam (5 mg/kg body weight), medetomidine (0.5 mg/kg body weight), and fentanyl (0.05 mg/kg body weight). Similar to the regular instillation process, mice were kept in a horizontal position and intubated with one side of a 20G cannula and the other side was connected to a mechanical ventilator (flexiVent FX system, Scireq Inc., Canada), enabling accurate control its respiration during aerosol inhalation. The ventilator was equipped with a nebulizer (Aeroneb Lab Small, Aerogen Inc., Galway, Ireland) for the generation of liquid aerosol droplets containing NP suspensions. For each mouse, 20, 40, or 60 μ L of MF suspension (12.5 mg/mL) was filled into the nebulizer, which was active for 40 ms per breath during mechanical ventilation with a protocol of 400 μ L tidal volume, 120 breaths/min, and an inhalation–exhalation time ratio of 2:1.

3.3.3 Intratracheal slow-instillation (PRP2)

Three methods of pulmonary particle delivery (slow instillation, ventilator-assisted aerosol inhalation, and intranasal aspiration) were imaged by using PB-PCXI. To allow either a lateral projection (*e.g.*, through the trachea) or an anteroposterior projection (*e.g.*, of the lungs), the mice should be fixed in an head-high upright (vertical) position, which is somehow different from the above-mentioned approaches in which the mice were laid in the

horizontal position. The setting for intratracheal slow-instillation delivery was very similar to that described in earlier studies^{49, 106-107}. Animals were mechanically ventilated using a FlexiVent ventilator (flexiVent FX system, Scireq Inc., Canada) with the protocol of 30 mL/kg tidal volume, 90 breaths/min, and an inhalation-inflation (breath-hold)-exhalation time ratio of 1:1:1. The liquid was introduced by a heat thinned PE10 polyethylene tube that was passed through the flexible wall of the ventilator inspiratory tube. The inner PE tube was thin enough unable to block the intubated cannula permitting simultaneous mechanical ventilation and liquid delivery. The NP liquid delivery via slow-instillation was remotely controlled by a syringe pump (UltraMicroPump III and Micro4 controller, World Precision Instruments, Sarasota, FL) that enables controlled liquid delivery and consecutive imaging during the whole instillation process. As listed in Table 1, 100 μ L NP mixtures (Sky Blue-iodine liquid with final dilution factors of 1: 20 for Sky Blue and 1:4 for iodine, melamine-iron oxide liquid with final dilution factors of 1: 20 for melamine and 1:4 for iron oxide NPs) or sole QDs (in 1: 20 dilution) were continuously delivered over the syringe pump through inner tubing to the trachea in approximately 24 s (delivery rate: 4.2 μ L/s). The used exposure time of 200 ms (except 100 ms for QDs) with sufficient signal-to-noise ratio was synchronized with the ventilated breath frequency. The PB-PCXI images were taken at a frame rate of up to 1.5 fps (frames per second) during the breath-hold which extremely reduced the motion noise in each breath-cycle.

To study the small volume delivery (4 μ L in 5 s, *i.e.*, 0.8 μ L/s) with and without surfactant (Alveofact 45 mg/mL, Lyomark Pharma GmbH, Germany), the identical set-up of slow-instillation delivery was used as 100 μ L liquid delivery. The only differences are that the exposure time was reduced to 100 ms to eliminate the unavoidable motion blur and the mice were spontaneously breathing so the ventilator was replaced with a non-contact fibre optic displacement sensor (RC-60, Philtec, MD) that was configured to detect respiratory motion and deliver an electrical trigger signal for image capture.

3.3.4 Ventilator-assisted aerosol inhalation 2.0 (PRP2)

For ventilator-assisted aerosol inhalation 2.0, an analogous setup and protocol as utilized for 100 μ L slow-instillation (80 breath/min, 30 mL/kg tidal volume, 200 ms exposure time, and the image shooting acquisition occurred during breath-hold phase in each breath cycle) was applied in this study. Only the inner PE10 polyethylene tube was removed and the ventilator was equipped with a nebulizer (Aeroneb Lab Small, Aerogen Inc., Galway, Ireland) for the

generation and transport of liquid aerosol droplets via the inspiratory tubing to the mouse lung. Since about 4-5% of applied aerosols were predicted to reach the deep lung and over 50% of the aerosols deposited in the ventilation tubing or exhaled out during nebulization¹⁸, a large amount of liquid should be filled in the nebulizer. It turns out that 150 μL NP-iodine mixture is the maximum liquid volume that can be nebulized without at least partially blocking the ventilation tubing by forming the big droplets. The nebulizer was active for 40 ms during inhalation per breath and has an output rate of 0.26 mL/min. Within 80 breath/min ventilation, it needs around 10.8 min (870 breaths) to nebulize 150 μL liquid and only 5.6 μL of contrast agent can be deposited to the deep lung (3.7% of applied dose is deposited in the lung). In case of an extremely low dose of iodine arrived at deep lung, a 2nd nebulization of 75 μL or 150 μL NP-iodine liquid was carried out. The aerosol delivery rate to the lung is 8.6 nL/s (= 0.0086 $\mu\text{L}/\text{s}$ = 5.6 $\mu\text{L}/10.8$ min). After each run the tubing of the ventilator was dried, the nebulizer was cleaned and refilled with NP-iodine suspension. For this type of application, a mixture of 1:5 iodine and 1:16 polystyrene NP suspension in distilled water was used.

3.3.5 Intranasal aspiration (PRP2)

For intranasal aspiration, an identical protocol was utilized as depicted by Gradl *et al.*¹⁰⁷. Briefly, a mixture of gold NP (1:2 stock dilution) and polystyrene-Sky Blue NPs (1:10 stock dilution) suspensions was added into a syringe pump, so that the controlled liquid delivery from outside the imaging hutch can be achieved. Here an 80 μL mixture of the gold-polystyrene NP liquid was spontaneously inhaled via the mouse nose. The exposure time of PB-PCXI was maintained at 100 ms with a frame rate 1.5 fps.

3.3.6 Other routes

Beside the means of pulmonary delivery mentioned above, oropharyngeal aspiration and nose-only exposure were performed and their 3D NP distribution profiles at single-cell resolution were also revealed in this study. Briefly, for oropharyngeal aspiration, a 50 μL MF NP solution (1:50 stock suspension) was dropped on the top of pharynx when the mouse was mildly anesthesia. The liquid can be directly aspirated to the lung during the next breath. For the nose-only inhalation exposure, a 2 mL of 1:10 MF suspension was aerosolized (the residual volume is about 0.86 mL in the nose-only system) and only part of liquid aerosols (1.14 mL) could be transported to the six channels with each port attached to a mouse nose. The nebulization time is expected to be 7 min.

3.4 *In vivo* propagation-based phase contrast X-ray imaging (PB-PCXI)

All X-ray based imaging experiments were performed at an inverse Compton scattering source - the Munich Compact Light Source (MuCLS) located at the Technical University of Munich (TUM) in Garching, Germany. The source itself, was developed and installed by Lyncean Technologies Inc. (Fermont, USA) ¹⁰⁸⁻¹⁰⁹, and the X-ray beamline infrastructure was designed and developed by TUM researchers. The source delivers a quasi-monochromatic and low divergence (4 mrad) X-ray beam. 25 keV X-rays with flux up to $2 \cdot 10^{10}$ ph/s were used. The working principle of PB-PCXI is to use free space propagation of a partial spatial coherent beam (typically around 1 m) after penetrating a sample to introduce additional contrast. As the x-ray wavefield propagates from the sample to the detector the sample-associated phase modulations of the X-ray wavefront are converted into intensity modulations, which can be directly measured by a high-resolution X-ray detector. Here the propagation distance (sample-to-detector distance) was chosen to 1 m. The images were recorded by an Andor Zyla 5.5 sCMOS camera (2560×2160 pixels), combined with a 20 μm thick Gadox scintillator (Gd₂O₂S:Tb) (CRYTUR, spol. s r.o., Czech Republic) deposited on a 2:1 fiber optic taper, resulting in 13 μm detector pixel-size. The source-to-sample distance was 4 m, leading to a geometric magnification of $M = 1.25$, an effective pixel size of 10.4 μm and a beam diameter of about 16 mm. As the X-ray beam has a fixed horizontal orientation, mice need to be positioned in a head-high position. Therefore, mice were placed in a specially designed mouse holder on a x-y-z rotation stage to facilitate positioning in the X-ray beam.

The pseudo-colored images in Figure 3-4 (PRP2) are a composition of the raw PB-PCXI images (grayscale) overlaid with the colored difference image ⁴⁹, from which a pre-delivery image was subtracted to highlight the location of the contrast fluid similar to the analysis performed in Donnelley *et al.*¹¹⁰. Images were aligned before color coding via a cross-correlation based image registration.

3.5 *Ex vivo* lung computed tomography

Followed by mice sacrifice and lung perfusion and isolation, some of the harvest lungs were moderately dried and inflated at a constant air pressure of 20-23 cm water at the lowest power in a microwave oven (SEVERIN, MW7803; 10% power; 90 Watt). Prior to fluorescence-based imaging, the *ex vivo* lung CT was first carried out on the isolated, dried, and inflated lung. A total of 2049 projections over 360 degrees were scanned and reconstructed with a

standard fbp-reconstruction analysis. The 3D images were generated by using AVIZO or Bitplane Imaris (<http://www.bitplane.com/imaris/imaris>).

3.6 *Ex vivo* whole-lung and lung-slice fluorescence imaging

The *ex vivo* whole lung fluorescence imaging (WLF) was performed for the lungs at different time points during optical tissue clearing using an IVIS (*in vivo* imaging system, Lumina II, Caliper/Perkin Elmer, USA) equipped with optical filters suitable for the various fluorescent NPs (for polystyrene-Sky Blue and MF NPs at an $ex/em = 640\text{ nm}/Cy5.5$ and for QDs $ex/em = 640\text{ nm}/ICG$). The fluorescence intensity and the 2D projected geometric area of NP-loaded whole-lung at continuous time points during tissue clearing were determined by using the Living Imaging 4.0 (Caliper). The variations of fluorophore intensity and lung area reveal the chemical resistance of NPs and area shrinkage factor of the lung, respectively.

The dried and inflated lungs were also imaged by WLF and were further imaged by the lung-slice fluorescence imaging (LSFM), in which fluorescence imaging was performed at single lung slice of a whole lung sample after consecutive cutting. Briefly, the dried lungs were embedded in polyurethane foam (PU foam Pattex Ultraweiss, Pattex, Germany) and sliced progressively perpendicular to the lung axis at an interval of 1 mm. After each slicing step, fluorescence and white light images of the 1 mm slice and the block face were captured with IVIS using optical filter of $ex/em = 640\text{ nm}/Cy5.5$. Both sides (top view and bottom view) of each 1 mm slice were scanned. For quantification of NP doses in slow-instilled or inhaled lungs with method of lung slice fluorescent imaging (LSFI), an intensity-dose standard curve was established using 3 blank lungs and 4 NP-loaded lungs after regular instillation process (50 μL 1:10 diluted or 100 μL 1:20 diluted SkyBlue NPs). To yield the absolute fluorescent signal induced by NPs, the autofluorescence signal in each NP-treated lung should be subtracted from the directly measured fluorescent signal. The fluorophore dose in a whole lung should be principally proportional to the sum of the absolute fluorescence intensities from all 1 mm slices. After yielding the desired fluorescence intensity-dose conversion curve, quantitative measurement of the deposited dose in those lungs could be achieved. The NP deposition in each/whole part (left/right/whole lung) was carried out with the method of WLF. To compare the fluorophore intensity normalized to geometric area in each part, the absolute fluorescence intensity was first obtained after subtraction of the background intensity.

3.7 *Ex vivo* tissue-clearing LSFM

Whole-lung samples were experienced an optical tissue clearing with a modified version of the 3DISCO protocol⁴⁶. Briefly, three organic solvents namely tetrahydrofuran (THF, Sigma 186562- 1L), dichloromethane (DCM, Sigma 270997-1 L), and dibenzyl ether (DBE, Sigma 108014-1KG) were used and the treatment procedures as following: 1) dehydration in 10 ml of 50% v/v THF/H₂O overnight, 50% THF/H₂O 1 h, 70% THF/H₂O 4 h, 80% THF/H₂O 4 h, 100% THF 1 h, 100% THF overnight, and 100%THF 1 h with slightly shaking; 2) lipid removal DCM around 30 min until lung samples sank to the bottom; 3) matching the refractive index of lung sample with DBE without shaking more than 2 h until imaging and the cleared lungs can be stored in DBE in long term at room temperature.

Tissue-cleared transparent lung samples were scanned with a LSFM (Ultramicroscope II, LaVision Biotec) equipped with a sCMOS camera (Andor Neo) and a 2× objective lens (Olympus MVPLAPO 2×/0.5 NA) equipped with an Olympus MVX-10 zoom body, which provided zoom-out and -in ranging from 0.63x up to 6.3x. For LSFM of the whole-lung, light sheet scans were generated with 0.63× zoom magnification (lens + zoom, 1.26X actual magnification) with specific ex/em bandpass filters for polystyrene-Sky Blue and MF NPs (ex/em=640/690 nm) and QDs (ex/em=640/795 nm) with a step size of 10-20 μm depending on the sample size. Lung tissue autofluorescence was generally scanned with optical filters of ex/em=545/605 nm. An exposure time of 150 ms and full laser power were typically applied to LSFM with the light sheet at various xy width and numerical aperture (NA) to adapt with the sample size. High magnification scans were usually carried out with smaller step sizes *e.g.*, 2-5 μm. Samples were submerged in DBE during LSFM image acquisition.

3.8 Image processing and analysis

3.8.1 Determination of lung morphology

The LSFM images presented in the figures include both 2D single slice images and 3D images with maximum intensity projection (MIP) in which a method for visualization of 3D data that displays only the voxels with maximum intensity along each optical ray passing through the image stack in the projection image¹¹¹. Some basic lung morphometric parameters like bifurcation angle and airway diameter were manually segmented and measured in 3D using Imaris. The alveolar mean chord length (MCL) was calculated directly by setting up random test lines consisting of solid lines and dashed lines superimposed on 2D

images using ImageJ as previously described¹¹²⁻¹¹³. The airway diameters and MCL of unfilled lungs should be corrected for deformation effects due to the deflated state of the lung and shrinkage during tissue clearing. For tissue shrinkage factor during optical clearing, we converted the IVIS measured shrinkage of the 2D image of the lung to 1D by taking the square root of the 2D shrinkage factor. The 1D deflation correction factor accounting the deflation state of the lung was determined from the volume ratio of the inflated (0.8 mL agar + 0.3 mL residual lung volume) and deflated (0.3 mL) lung yielding 1.54 ($= (1.1/0.3)^{1/3}$). The 0.3 mL residual lung volume of a collapsed lung was used based on the Yi *et al.*, results⁴³⁻⁴⁴. More details about the conversion and calculation can be found in method part of the paper (Yang *et. al.* 2018)¹⁸.

3.8.2 Establishment of the intensity-dose conversion curve for particle dosimetry

Quantitative analysis of the images recorded by LSFM requires elaborate judgement of the instrument biases, variations of lung optical properties, *etc.* To achieve the quantitative assessment, the absolute fluorophore intensity in each NPs treated lung was calculated following correction of the measurement bias for each lung (*e.g.*, the tissue autofluorescence differentiation) and subtraction of the background tissue autofluorescence (detailed in SI method, PRP1). The fluorescence NP dose in a whole lung is principally proportional to the sum of the absolute fluorescence signals measured from all LSFM slices. The conversion factor of the fluorophore dose and the absolute fluorophore intensity can be determined by preparing various instilled lungs with known but different amounts of NPs (50 μ L 1:25, 1:50, 1: 100, and 1:200 dilutions of MF stock solution). After yielding a linear relationship (standard curve) between the fluorescence intensity and particle dose, accurate dosimetry of the deposited dose in mouse lungs after inhalation exposure could be achieved. The inhaled NPs dose in the lungs of mice via intubated inhalation exposure was determined by gravimetric analysis (here inhaled about $36.0 \pm 8.5\%$ of the applied dose) and but only a very small amount of inhaled dose can be transported to the lung.

3.8.3 C/P and lobe-wise distribution analysis

The particle regional deposition in the lung was determined on two scales, a two-region (central *versus* peripheral region) and a lobe-wise approach. For the widely used two-region method in images usually scanned by nuclear medical imaging, the central region is defined as the circumference shaped matched inner 50% of each lung slice, and the entire lung area in each image (slice) was determined by intensity thresholding. Area-normalized particle dose

in two regions was then determined in single image (slice) summed up all slices or from a 3D MIP image of an entire lung. Then the deposition ratio of central to peripheral intensity normalized to the respective area can be calculated as below formula. Of note, to obtain the absolute fluorescent signals induced by the particles in the central or peripheral regions of the lung, the total fluorescent correction and tissue autofluorescence subtraction have been first performed.

$$C/P = \frac{I_c/I_p}{A_c/A_p}$$

Here, I_c and A_c refer to the absolute particle fluorescence signal and the area, respectively in the central region of lung slices. I_p and A_p mean the absolute particle fluorescence signal and the area, respectively in the peripheral region of the lung slices. The slice-by-slice analysis was performed on every fourth slice of each lung stack excluding the top and bottom slices since they predominantly contain peripheral regions. The final C/P ratio obtained from averaging over all slices depicts the uniformity of the particle deposition. C/P close to unity indicates an even particle distribution in the lung, while C/P larger than unity denotes preferential central airway deposition.

Furthermore, lobe-wise analysis was also carried out to unveil the homogeneity of particle distribution among five lung lobes for both application methods. Relying on the recognition of the space between two adjacent lobes, the individual lobe can be manually differentiated and segmented in LSM images. Subsequently, the fractional deposition of particles on all five lung lobes and the trachea was obtained using ImageJ. Particle deposition evenness was determined as volume- (Cavalieri principle for estimation of lung/lobe volume)¹¹⁴ normalized intensity signal for individual lobe after correction of total fluorescence and subtraction of tissue autofluorescence. The deposition fraction normalized to volume is then calculated from

$$Dep_v = \frac{I_l/I_t}{V_l/V_t}$$

where I_l and V_l refer to the particle-induced fluorescence intensity and the volume, respectively in a specific lobe. Analogous I_t and V_t are particle-induced fluorescence intensity and the volumes, respectively in the total lung (without trachea). Dep_v is close to 1,

indicating that particle dose deposited a specific lobe is equal to the fractional lung volume of this lobe. Values lower and larger than unity suggest reduced or preferential deposition of particle in this particular lobe.

3.9 Quantitative fluorescence analysis of particle dose in lung homogenates

To determine the total particle tissue burden in the whole lung, trachea, and esophagus, a reference method relying on the quantitatively fluorescent dosimetry of particle dose in homogenized tissue was utilized as previously described⁴⁷. Briefly, tissue samples were homogenized by a homogenizer (Ultra Torrax, 20000 rpm) at a 1:10 ratio of tissue to 0.1 M PBS buffer. A fluorescence intensity- dose standard curve was established by using a series of known doses of fluorescent particle added into the blank tissue enabling quantification of the particle dose in different tissue samples.

3.10 Statistical Analysis

All X-ray based images were flat field and dark current corrected. X-ray images and videos were analyzed and generated using ImageJ (<https://imagej.nih.gov/ij/>). Fluorescence images including both WLF and LSF and their respective analysis of NP dosimetry were carried out with the Living Imaging 4.0 Software (Caliper). The 2D and 3D images and videos obtained from LSF were processed using ImageJ and Bitplane Imaris. All data were presented as mean \pm standard deviation (SD) and plotted using SigmaPlot version 12.0 (Systat Software GmbH, Germany). Normality was determined using the Shapiro–Wilk test and a visual assessment of histograms. Comparison of results between two groups for normally distributed data was carried out using a student t-test with two-sided and for nonparametric data with Mann-Whitney rank-sum test. Comparisons among multiple groups were performed using a one-way analysis of variance (ANOVA) followed by pairwise multiple comparison procedures (Holm-Sidak method). Significances are defined as 0.05 ($P < 0.05$, *), 0.01 ($P < 0.01$, **), and 0.001 ($P < 0.001$, ***). $N \geq 3$.

4. Results

4.1 Summary of the work PRP1

Three-Dimensional Quantitative Co-Mapping of Pulmonary Morphology and Nanoparticle Distribution with Cellular Resolution in Nondissected Murine Lungs

This study describes and validates (in murine lungs) the first single-modality imaging technique for NP distribution in the lung with the following new features.

- Staining-free 3D morphology imaging and complete morphometric analysis of murine lungs (from the trachea, through the entire airway tree down to the alveolar ducts and sacs including blood vessels).
- Co-mapping of lung morphology and (fluorescent) NP distribution throughout the entire murine lung with accurate NP dosimetry.
- Whole-lung fluorescence imaging with cellular resolution in non-dissected *ex vivo* murine lungs.

Here, the 3DISCO tissue clearing protocol was optimized for lung tissue and a method was developed for quantitative lung morphometry and dosimetry of (fluorescent) NPs with light sheet fluorescence microscopy (LSFM). We also introduce a time-efficient and reliable method for assessing both the preservation of lung morphology (or correction thereof) and the optical stability of fluorescent dyes during tissue clearing, since the chemically harsh process of optical tissue clearing renders some of the available fluorophores unstable and may cause shrinkage/swelling of lung tissue. Finally, the validity of the morphometric and dosimetric methods presented here was demonstrated by good agreement with previously reported literature data on lung morphometry and lobe-specific NP dose (quantum dots, melamine resin) after inhalation or intratracheal instillation of NPs into murine lungs. Tissue-cleared LSFM imaging on these nondissected lungs presented here closes the technological gap between whole-lung *in vivo/ex vivo* imaging techniques (MRI, PET, IVIS, *etc.*), which only depict gross anatomical distribution of NPs, and 2D stereological methods, which provide high resolution NP localization but no 3D information on the whole lung scale.

My contributions are about performing the animal exposure, optimization of tissue clearing methods for lung, designing the methods for the testing the stability of fluorescent tracers and tissue shrinkage during the tissue clearing, lung imaging using LSFM, imaging process and video manipulation, quantitative dosimetry analysis, figure preparation, and manuscript writing and revisions.

Three-Dimensional Quantitative Co-Mapping of Pulmonary Morphology and Nanoparticle Distribution with Cellular Resolution in Nondissected Murine Lungs

Lin Yang,^{†,‡,||} Annette Feuchtinger,[§] Winfried Möller,^{†,‡} Yaobo Ding,^{†,‡} David Kutschke,^{†,‡} Gabriele Möller,[#] Johannes C. Schittny,[¶] Gerald Burgstaller,^{†,‡} Werner Hofmann,[□] Tobias Stoeger,^{†,‡} Daniel Razansky,^{⊥,||} Alex Walch,[§] and Otmar Schmid^{*,†,‡}

[†]Comprehensive Pneumology Center (CPC-M), Member of the German Center for Lung Research (DZL), Munich, 81377, Germany

[‡]Institute of Lung Biology and Disease, Helmholtz Zentrum München–German Research Center for Environmental Health, Neuherberg, 85764, Germany

[§]Research Unit Analytical Pathology, Helmholtz Zentrum München, Neuherberg, 85764, Germany

[⊥]Institute for Biological and Medical Imaging (IBMI), Helmholtz Zentrum München, Neuherberg, 85764, Germany

^{||}Faculty of Medicine, Technical University of Munich, Munich, 80333, Germany

[#]Department Genome Analysis Center, Institute of Experimental Genetics, Helmholtz Zentrum München, Neuherberg, 85764, Germany

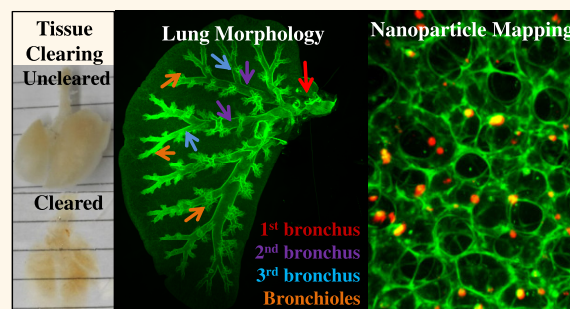
[¶]Institute of Anatomy, University of Bern, CH-3012 Bern, Switzerland

[□]Department of Chemistry and Physics of Materials, University of Salzburg, Salzburg, A-5020, Austria

Supporting Information

ABSTRACT: Deciphering biodistribution, biokinetics, and biological effects of nanoparticles (NPs) in entire organs with cellular resolution remains largely elusive due to the lack of effective imaging tools. Here, light sheet fluorescence microscopy in combination with optical tissue clearing was validated for concomitant three-dimensional mapping of lung morphology and NP biodistribution with cellular resolution in nondissected *ex vivo* murine lungs. Tissue autofluorescence allowed for label-free, quantitative morphometry of the entire bronchial tree, acinar structure, and blood vessels. Co-registration of fluorescent NPs with lung morphology revealed significant differences in pulmonary NP distribution depending on the means of application (intra-tracheal instillation and ventilator-assisted aerosol inhalation under anesthetized conditions). Inhalation exhibited a more homogeneous NP distribution in conducting airways and acini indicated by a central-to-peripheral (C/P) NP deposition ratio of unity (0.98 ± 0.13) as compared to a 2-fold enhanced central deposition ($C/P = 1.98 \pm 0.37$) for instillation. After inhalation most NPs were observed in the proximal part of the acini as predicted by computational fluid dynamics simulations. At cellular resolution patchy NP deposition was visualized in bronchioles and acini, but more pronounced for instillation. Excellent linearity of the fluorescence intensity–dose response curve allowed for accurate NP dosimetry and revealed *ca.* 5% of the inhaled aerosol was deposited in the lungs. This single-modality imaging technique allows for quantitative co-registration of tissue architecture and NP biodistribution, which could accelerate elucidation of NP biokinetics and bioactivity within intact tissues, facilitating both nanotoxicology studies and the development of nanomedicines.

KEYWORDS: 3D whole lung imaging, pulmonary nanoparticle delivery, 3DISCO, optical tissue clearing, acinar deposition, airway deposition



The superb physicochemical properties of manufactured nanomaterials (NMs) greatly facilitate their increasingly widespread use in medicine and industry, which has led to exponential growth of NM-containing industrial

Received: October 2, 2018

Accepted: December 19, 2018

Published: December 19, 2018

products over the past decades.^{1,2} Large-scale manufacturing of NMs substantially increased the risks for human health especially but not limited to occupational settings,³ resulting in the release of new guidelines by the World Health Organization (WHO) to protect workers from the potential risks of NMs.⁴ In particular, respiratory inhalation of NMs and/or nanosized ambient particulate matter is a major public concern mainly associated with cardiovascular and pulmonary morbidity and mortality.^{5,6} Meanwhile, a number of novel-designed nanomaterial-based drugs (nanomedicines such as liposomes and polymers) are currently being evaluated at the preclinical level or have even reached the clinical settings.^{7–9} Consequently, extensive scientific efforts have been focused on understanding the fate of NMs in the organism and the underlying pathomechanisms of disease (or diagnostic and therapeutic effects) after respiratory delivery of NMs.^{10,11}

Intratracheal instillation and inhalation of NMs was most widely used in animal and human studies on the fate and toxicity of NMs.^{11–13} NMs were proved to be able to reach deep into the lung alveolar region and translocate from the lungs to circulation and from there to secondary organs, resulting in dose-dependent oxidative stress and inflammation, which often scales well with organ-delivered surface area dose.^{14–16} Most of these studies have been performed with spherical NMs, henceforth referred to as nanoparticles (NPs). Inhaled gold NPs were preferentially found at sites of vascular inflammation in both diseased rodents and humans examined using high-resolution inductively coupled plasma mass spectrometry (ICP-MS) and Raman microscopy.¹⁷ Thus, distribution, localization, and dosimetry of NPs within whole organs and even whole organisms are of paramount importance for understanding the link between physicochemical characteristics of NPs and associated health effects.^{18–20} Currently available *in vivo* imaging techniques offer gross anatomical distribution of NPs using, for example, X-ray computed tomography, magnetic resonance imaging (MRI), *in vivo* imaging system (IVIS), positron emission tomography (PET), single photon emission computed tomography (SPECT), and photoacoustic imaging.^{2,9} However, these modalities are often unable to resolve biological interactions of NPs with tissue and are limited to visualizing NP localization at cellular resolution. To achieve this goal, several common *ex vivo* assays, including transmission electron microscopy (TEM), 2D stereological methods, flow cytometry, and ICP-MS, were applied to examine and/or quantify NP localization and distribution at cellular resolution, but the information on 3D tissue architecture was totally destroyed.^{20–22} Currently, no available technique is able to both visualize the spatial distribution of NPs and quantify their accumulated dose in entire organs (*e.g.*, lungs) with cellular resolution.

Moreover, understanding the spatial distribution and biokinetics of NPs with cellular resolution at the whole organ level has also significant implications for NP-based drug delivery (*e.g.*, nanomedicines).^{8,23} For instance, the delivery of nanomedicines into diseased regions of the lungs *via* inhalation is of central importance for therapeutic efficacy and pharmacokinetics. 3D imaging of whole diseased organs could provide both qualitative and quantitative data on nanomedicine delivery to the sites of disease (*e.g.*, lung cancer or alveolar region for the treatment of lung emphysema), and thus verify the targeting efficacy of novel-designed nanomedicines.^{2,9,24}

As mentioned above, current imaging methods with cellular resolution rely on tissue sectioning. Alternatively, in order to observe the 3D imaging maintaining the integrity of tissue

architecture, tissues ideally should be imaged as a whole organ or whole body without sectioning. However, biological tissues generally have strong light absorption and light scattering, which hamper light penetration, leading to low resolution and imaging depth.²⁵ Recently, the concept of optical tissue clearing attracted major interest, as it essentially renders tissues transparent, enabling 3D imaging of intact tissue using confocal laser microscopy and two-photon microscopy.^{25,26} The more recent emergence of light sheet fluorescence microscopy (LSFM) has revolutionized several fields of research, primarily neurobiology and embryology, since this 3D imaging method allows unraveling of molecular and cellular events at the whole organ level (*e.g.*, the brain and embryo).^{27,28} Allowing multiwavelength imaging of endogenous fluorescence proteins, immune-labeled biomolecules, and intravenously delivered probes, LSFM permits 3D imaging of tissue structure such as vascular system, neurons, axons, glomerulus, *etc.*, offering more accurate data of tissue morphology and physiological or pathological state compared to the traditional 2D histomorphological method.^{29,30} High scattering effects in the lung due to the millions of air–tissue interfaces have made the lung a particularly elusive inner organ for LSFM even for small rodent models (mice). Hence, unlike the liver and spleen, there are currently no LSFM data on co-registration of 3D lung morphology and quantitative NP distribution throughout the entire murine lung.³¹

This study aims to co-register the lung architecture and quantitative distribution of pulmonary applied NPs in non-dissected (whole) and unstained murine lungs by using LSFM after 3DISCO²⁵ tissue clearing (as a time-saving and high-quality clearing method). This study provides a label-free 3D visualization and morphometric analysis of the complete epithelial architecture of an entire murine lung combined with quantitative dosimetry of fluorescently labeled NPs at the whole-organ level with cellular resolution. This revealed insights into the effect of different routes of NP application (intratracheal instillation and inhalation) on the pulmonary NP deposition profile.

RESULTS

The method presented here allows for simultaneous 3D mapping of label-free lung morphology and pulmonary distribution of fluorescent NPs. This requires bichannel imaging of optically cleared lungs with one channel optimized for tissue autofluorescence and the other tailored toward the fluorescence spectrum of the NPs under investigation.

3D Visualization and Quantitative Analysis of Whole Lung Morphology. 3D lung morphology and airway architecture were generated from tissue autofluorescence imaged using the excitation and emission (ex/em) filters at 545 and 605 nm, respectively. The degree of transparency of a cleared lung after undergoing the refined 3DISCO protocol is evident from [Figure 1a](#). An example of selected images obtained from sequential planewise illumination of the whole lung using LSFM is depicted in [Figure 1b](#). 3D reconstruction of the entire stack of images allowed for clear identification of the entire airway structure down to generation 16 to 21 and even beyond into the alveolar structure and blood vessels ([Figure 1c](#) and [Video S1](#)). To categorize the airway segments of the monopodial lung structure of a mouse, an “order”-based terminology as introduced by Wallau *et al.*³² is more suitable than generation-based numbering schemes, which are more suitable for dichotomous lungs (*e.g.*, from humans). In an order-based lung structure, a daughter airway segment can be assigned

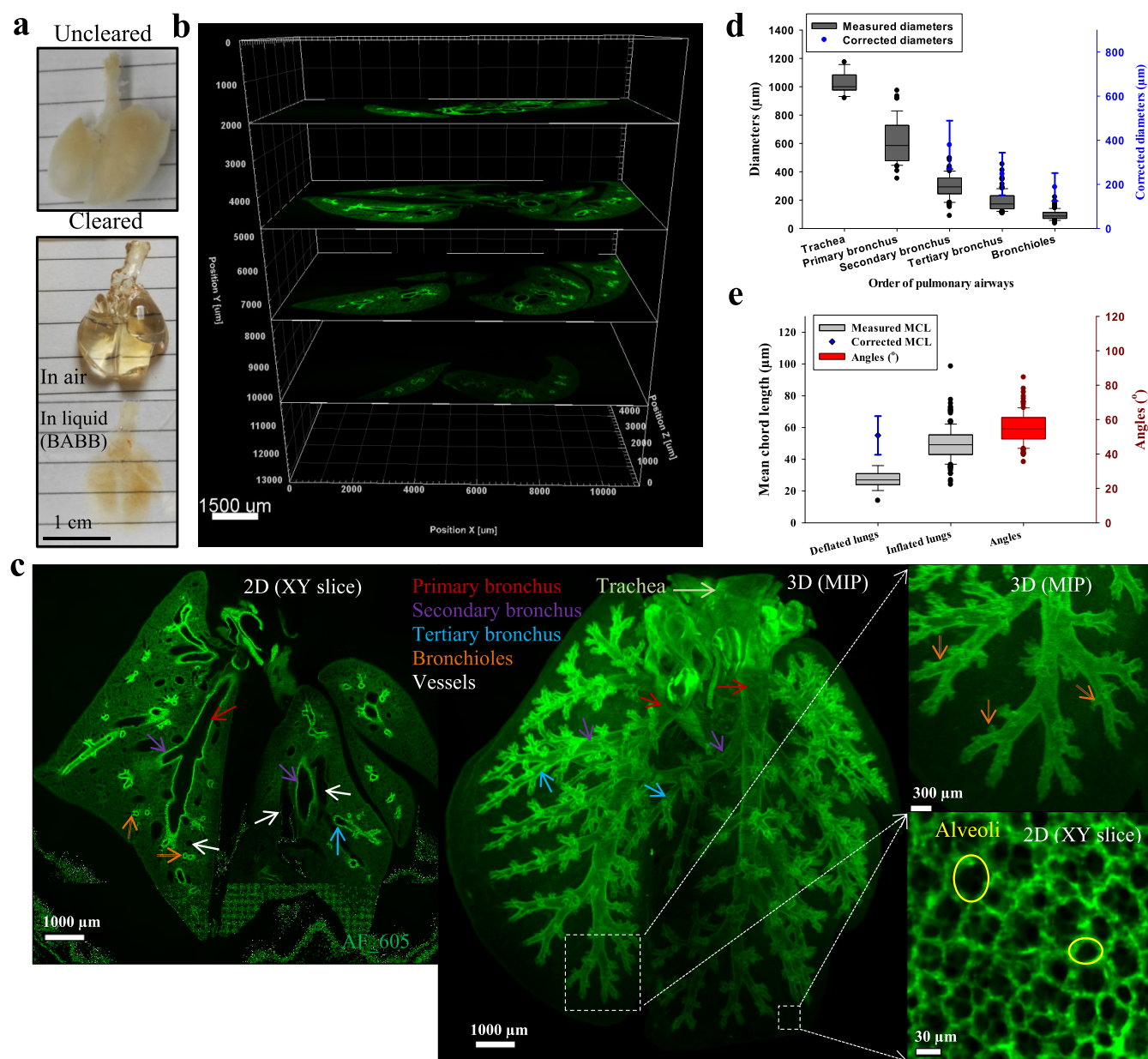


Figure 1. Three-dimensional (3D) visualization and quantitative morphometry of a whole murine lung using light sheet fluorescence microscopy (LSFM) after tissue clearing in the tissue autofluorescence channel (ex/em = 545/605 nm). (a) Whole mouse lung prior to (uncleared) and after tissue clearing (in air and in BABB solvent). (b) Z-stack of sequential images recorded as the lung is illuminated *via* stepwise-shifted light sheets along the Z-dimension. The resulting images cover the entire width of the lung (>1 cm) with no loss of image quality near the center, the point of maximum light attenuation. (c) Representative images of a single (2D) light sheet and a 3D reconstruction of the whole lung using maximum intensity projection over the entire image stack, which clearly exhibit the full anatomical information from the trachea, over the primary bronchus down to the small (terminal) bronchioles and even the blood vessels. The typical alveolar honeycomb structure can also be visualized when imaging at cellular resolution using LSFM. (d) Originally measured and deflation- and shrinkage-corrected (3D) diameters of the branches of the pulmonary bronchial tree (from trachea to small bronchioles) are presented. (e) Originally measured and (deflation-/shrinkage-) corrected mean chord lengths (MCL) of the alveolar region, as well as the branching angles of the entire bronchial tree in deflated lungs, and MCL in inflated lungs (no deflation-/shrinkage-correction as the lung was filled with agar) are displayed.

the same order as its parent segment if its diameter is closer to that of its parent segment or significantly larger than its sister segments. Otherwise, all daughter segments receive an order greater than that of their parent segment (Figure 1c). Of note, the original distribution of NPs is expected to be preserved in deflated or unfilled lungs, since potential redistribution of NPs due to wash-down effects when filling the lung is avoided, while the airway diameters of deflated lungs should be corrected for deformation (shrinkage) effects from the bronchioles to the

alveoli due to the lack of cartilage. Moreover, lung shrinkage also occurs during tissue clearance, but this effect is expected to be limited to secondary bronchi and higher order generations due to the massive presence of cartilage in the trachea and primary bronchi. Data for originally measured and deflation-corrected diameters of the affected airways (secondary, tertiary bronchus, small bronchioles) and alveolar mean chord length (MCL) are presented in Figure 1d and e for both inflated and deflated lungs. The MCL in the inflated lungs filled with 0.8–1 mL of agar

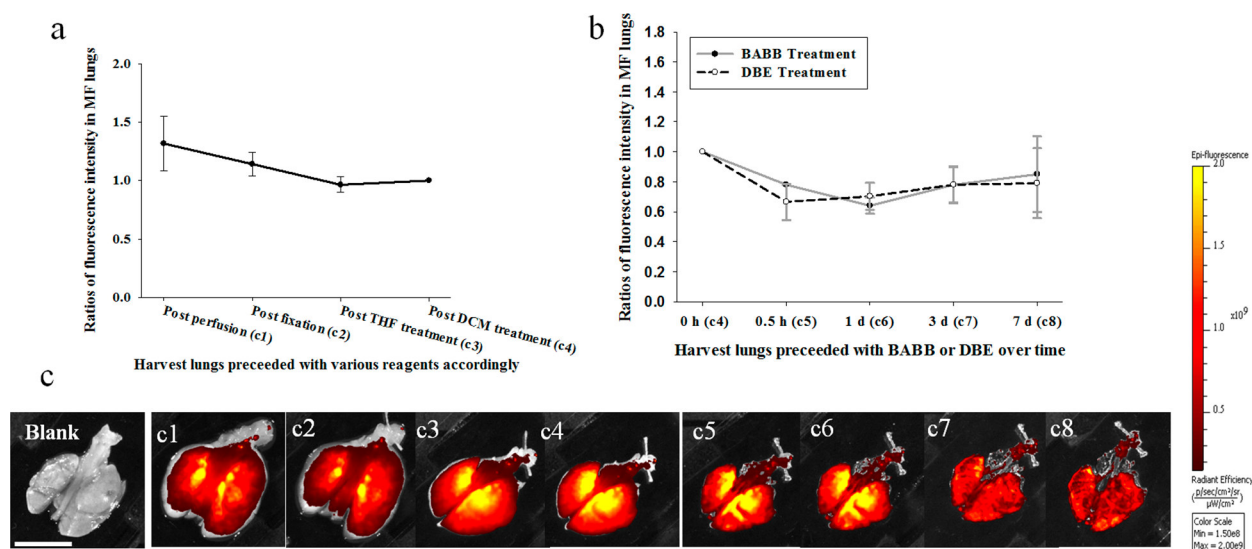


Figure 2. Analysis of fluorophore (MF NPs) stability in lungs at different stages of the 3DISCO optical clearance protocol using the *in vivo* imaging system (IVIS). The fluorescence intensity at each step was normalized to that after DCM treatment, starting after lung perfusion, over water and lipid removal (a) to refractive index matching with BABB or DBE (b). (c) Representative *ex vivo* lung images (c1–c8) from mice receiving 25 μg of MF *via* intratracheal instillation measured by IVIS, indicating that the fluorescence of MF is relatively stable during the first day of the protocol and preserved up to 7 days (storage in BABB or DBE), despite the occurrence of lung shrinkage. The left lung of panel c (a, blank lung) represents no fluorescence can be observed under the same scale of NP-specific ex/em channel as the treated lung. Scale bar: 1 cm.

(corresponds to near full inflation of the lung) was determined to be $49.7 \pm 10.9 \mu\text{m}$, which agrees with the $55.0 \pm 12.1 \mu\text{m}$ obtained from the deflated lung after applying the deformation correction due to the low inflation state. This MCL value is consistent with literature values ranging from 30 to 70 μm in healthy adult mice for varying states of lung inflation.^{33,34} Moreover, the branching angle of airway bifurcations averaged over all airway orders of four lungs was found to be $55.0^\circ \pm 14.2^\circ$ (for WS7BL/6 mice), which is consistent with the angles around 10° to 100° found in first six airway generations of C57BL/6 mice,³⁵ but slightly higher but less broadly distributed than $45.6^\circ \pm 24.3^\circ$ observed in adult BALB/c mice using contrast-enhanced micro-CT.³⁶

The paramount role of excellent lung perfusion for high-quality tissue clearance is evident from lung morphology images (autofluorescence channel). Residual blood due to poor transcatheter perfusion of the lung will inhibit light penetration, resulting in “dark regions” near the center of the lung (Figure S1a). Since laser light with larger wavelength is less attenuated and therefore penetrates deeper into tissue, red (or near-infrared) light allows for more uniformly illuminated images of the 3D whole lung morphology, even for less than perfectly cleared lungs (Figure S1b,c). After surface rendering using Imaris, the airway structure becomes even more evident in the red than in the green channel (Figure S1d).

In summary, organic solvent-based clearing combined with LSFM imaging preserves the integrity of the lung architecture and thus offers the potential for providing higher accuracy 3D lung morphometry *versus* conventional sectioning-based, 2D stereological methods.

Effects of Tissue Clearing on Fluorescence Stability of NPs. In general, the 3DISCO clearing protocol involves tissue dehydration, lipid removal, and matching of the refractive index (RI), which is accomplished by treatment with three organic solvents, tetrahydrofuran (THF), dichloromethane (DCM), and dibenzyl ether (DBE). This rather harsh chemical treatment regimen could eradicate the activity of cell-produced fluo-

rescence reporter dyes (*e.g.*, fluorescence proteins) and fluorescence-labeled NPs (*e.g.*, by digestion of the polystyrene latex matrix protecting the Sky Blue dye). In this study a time-saving and accurate method was developed for fast checking the stability of fluorescence dyes and tissue shrinkage during and after tissue clearing using an IVIS system, which allowed for *ex vivo* imaging of whole murine lungs before and after each step of the clearing procedure. This *ex vivo* imaging method is superior to standard *in vitro* incubation of fluorophores with each organic solvent, as fluorophores may not dissolve/disperse in and thus separate from organic solvents, leading to inaccurate and biased information. In this study, three types of fluorescent NPs with volume median diameters between 17.6 and 480 nm (Sky Blue (diameter: $480.5 \pm 114.5 \text{ nm}$), melamine resin (MF) NPs ($474.3 \pm 124 \text{ nm}$), and quantum dots (QDs, $17.6 \pm 6.7 \text{ nm}$), see Figure S2 for size distributions) were intratracheally instilled into mice, and lungs were harvested, perfused, and spectrophotometrically measured using the IVIS. This analysis of fluorophore stability revealed that the fluorescence intensity of MF NPs was statistically insignificantly decreased during tissue clearing and no significant difference was found between the mixture of benzyl alcohol and benzyl benzoate (BABB) and DBE treatment up to 7 days, indicating that the fluorescence activity of MF NPs is well preserved during the tissue clearing process (Figure 2a and b). Also, the fluorescence intensity of lungs instilled with MF and QDs at a dose of 62.5 $\mu\text{g}/\text{lung}$ and 40 pmol/lung, respectively, was over 10-fold higher than the autofluorescence of blank lungs in the NP-specific optical channels (Figure S3a and b), which provides a sufficient signal-to-background ratio for quantitative NP dosimetry with LSFM imaging as shown below. Moreover, long-term fluorescence stability of MF NPs after 3DISCO processing was observed for up to weeks and even months (Figure 2b and c). In contrast, Sky Blue was degraded *ca.* 150-fold (according to IVIS) by tissue clearing, resulting in signal-to-background ratios of about 1.5 even for a very high dose of 100 $\mu\text{g}/\text{lung}$, which was too low for reliable NP dosimetry (data not shown). It is also noteworthy

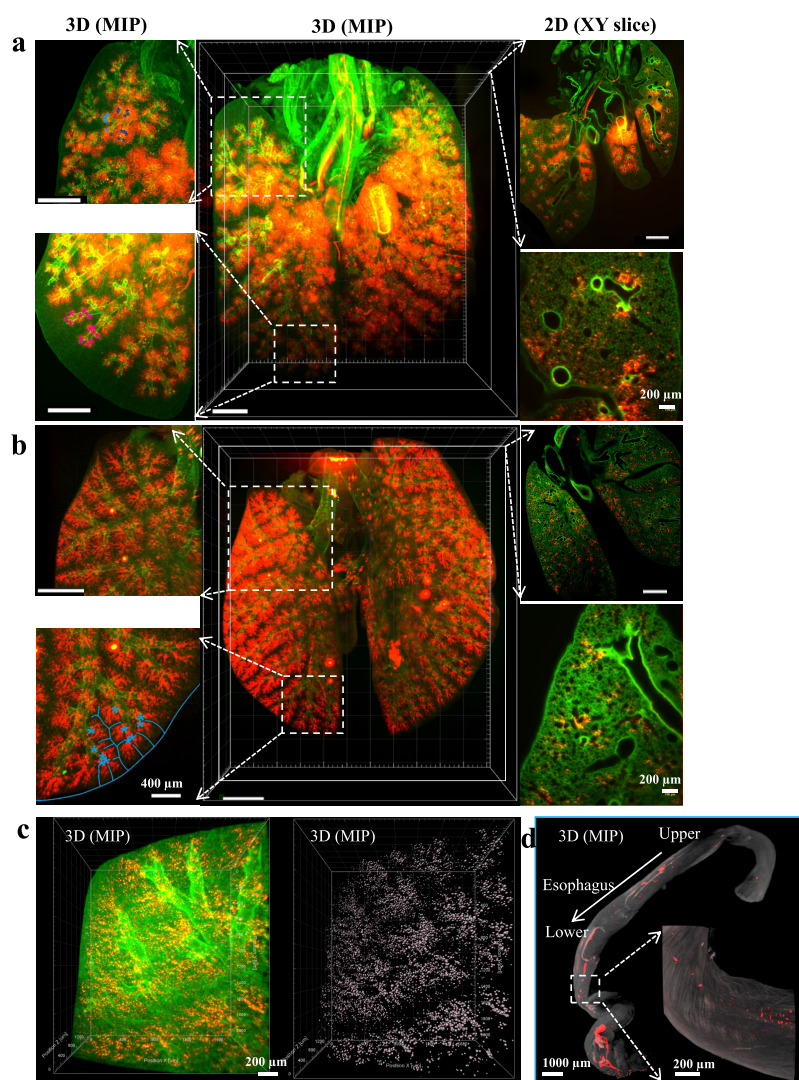


Figure 3. 3D mapping of melamine resin (MF) NP distribution pattern in (non-dissected) whole murine lungs after pulmonary NP delivery *via* instillation and inhalation. Distribution of MF (red) in a Z-stack image of a whole lung (3D MIP) and in a single slice (2D *xy* slice) with respect to tissue structure (autofluorescence, green) after different application routes (panel a: instillation; panel b: inhalation). NPs are observed to accumulate along the whole bronchial tree and into the acini. A much more homogeneous NP distribution pattern was detected for inhalation (panel b) as compared to the patchier deposition pattern for instillation (panel a). After instillation preferential central acini were heavily loaded and relative homogeneously filled with NPs (dark blue asterisks in upper right panel of a), and most of the peripheral acini received only very small amounts of NP (magenta asterisks in lower right panel in a). After inhalation the deposited amount per acinus was much more homogeneous and similar in central or peripheral regions of the lungs (central panel in b). However, the NP deposition inside individual acini was very inhomogeneous: While the proximal regions received most of the NPs, the distal regions showed little deposition (light blue asterisks lower right panel in b). (c) At cellular resolution even for inhalation preferential proximal localization of NPs inside acini was further revealed (left) independent of the lung region, as illustrated by spot ($5.5\ \mu\text{m}$) rendering (right). (d) 3D visualization of MF (red) transported and accumulated in the esophagus (gray) immediately ($<3\ \text{min}$) after administration. Undesignated scale bars: $1500\ \mu\text{m}$. The fluorescence intensity scale in the different images/panels varies for optimized overlay representation.

that the lungs shrunk after THF treatment by about 37–44% in the projected area with no further shrinkage after 1 day of DBE and/or BABB treatment (Figure S4).

3D Lung Mapping of MF Distribution with Cellular Resolution after Intratracheal Instillation and Inhalation Application. Numerous studies have been performed on NP–lung interaction after pulmonary delivery of NMs *via* intratracheal instillation and inhalation. However, potential differences in the distribution of NPs throughout the murine lung depending on the application route are still not sufficiently described. The specific capabilities of tissue clearance reduce tissue–light interactions (absorption, scattering) and allow for co-imaging of (label-free) lung morphology and particle

distribution throughout the entire murine lung with cellular resolution (tissue penetration of light is over a few centimeters). In particular, overlaying maximum intensity projection (MIP) images of the NP distribution with the 3D lung structure reveals insightful information regarding the NP deposition pattern. This can be seen in the representative images obtained after intratracheal instillation or inhalation of MF (Figure 3a and b). Not surprisingly, MF was found deposited along the bronchial tree starting from the trachea down to the terminal bronchioles and into the acini for both application routes (Figure 3 and Videos S2 and S3). An acinus is defined as the airways distal of the terminal bronchioles. In mice these are the alveolar ducts and sacculi distal of the bronchio–alveolar duct

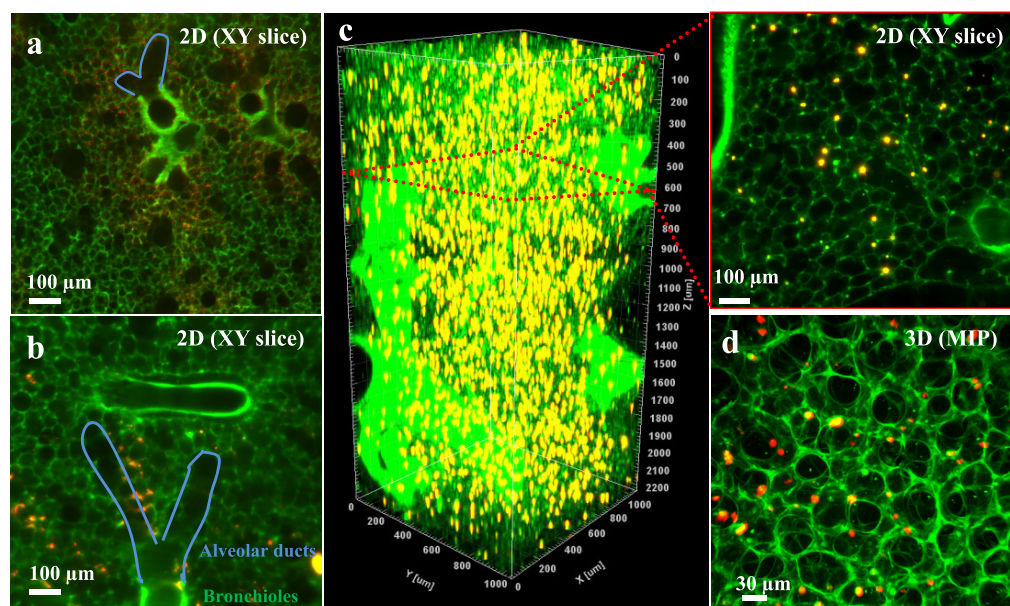


Figure 4. Visualization of NP deposition (red/yellow) with respect to alveolar tissue architecture (autofluorescence, green) at cellular resolution in deflated and inflated lungs. Cellular localization of MF NPs in the lungs scanned by LSFM, showing MF distributed into the terminal bronchioles (green), alveolar ducts (blue solid lines), and proximal alveoli of the acini immediately after both instillation (a) and inhalation (b). 3D images of MF distribution using LSFM (c) and confocal microscopy (d) at single-cell resolution in an inflated murine lung at 24 h after instillation, indicating the NPs were formed in relatively bigger agglomerates, which are likely due to phagocytic uptake and confinement by alveolar macrophages. LSFM allows for label-free deeper imaging of cleared tissue (*z*-direction: 2–5 mm) than confocal microscopy (50–80 μm).

junction. The 3D distribution pattern of NPs in the airways and acini varied significantly for different application routes. Inhalation exhibited a much more homogeneous NP distribution pattern as compared to the patchier and preferentially central and upper airway and central alveolar deposition pattern for instillation (Figures 3a,b and S5). Moreover, for inhalation extremely high NP doses were deposited at the end of the trachea and in certain regions of the lower airways appearing as circular drops (ca. 100–200 μm), which are possibly due to redistribution of deposited bulk liquid due to partial blocking of the airway (Figure S5). These features were not as evident for instillation application. When zoomed in or examined under higher magnification (Figure 3c), MF NPs were found to be mainly located in the small (or terminal) bronchioles but less accumulated in larger airways for both routes of delivery. Acinar deposition was quite different for the two forms of application. While after instillation the centrally located acini receive high doses, which were deposited all over the acini, the peripheral acini receive much lower doses, which were deposited in the entrance area of the acini (Figure 3a, as also shown by the central/peripheral scale; see below). After inhalation centrally and peripherally located acini received similar doses, which were predominately located in their proximal half (Figure 3b). Figure 4a and b shed more light on NP deposition in the alveolar septum and smaller bronchioles at cellular resolution after both applications. At this high level of resolution the NP distribution was not homogeneous in the alveolar region (inside acini). At 24 h after instillation we were able to visualize the 3D NP localization in intact lung tissue covering a volume of $1 \times 1 \times 2 \text{ mm}^3$ (and even bigger volumes like $5 \times 5 \times 5 \text{ mm}^3$ are possible, data not shown) without fading of fluorescence intensity as a result of highly reduced light attenuation in optically cleared tissue (Figure 4c and Video S4). Confocal imaging can also provide excellent label-free 3D images of NP distribution

(Figure 4d and Video S5), while it is limited by imaging depth (around 60 μm) due to the low autofluorescence of alveoli (indistinct signal over lumen). The NPs had formed larger agglomerates 24 h after both applications as compared to NPs at 0 h (Figure 4 and Figure S6), which is likely due to phagocytic uptake and confinement by alveolar macrophages.³⁷ Spot rendering of MF with Imaris revealed an apparent average NP diameter of approximately 5.5 μm immediately after inhalation (Figure 3c). This image analysis is unreliable for instilled NPs due to the patchy distribution of NPs in instilled lungs, limiting the localization of NPs by intensity gating. Moreover, existence of NPs in the esophagus indicated that NPs can be cleared within a few minutes toward the digestive tract by either mucociliary clearance or coughing (Figure 3d and Video S6).³⁸

Quantitative Analysis of Dose and Regional Deposition of Inhaled MF. It became evident that each lung had a different autofluorescence level due to differences in the optical properties of the lungs, in lung volume, and LSFM instrument uncertainties (despite that the same settings of LSFM were used for all lungs). Here, the average of measured total fluorescence intensity from blank lungs was $(11.1 \pm 3.33) \times 10^{10}$, and the relatively high standard deviation of 30.2% demonstrates the variations in tissue-induced fluorescence due to lung and instrument variations. Therefore, the correction of the total fluorescence level in each NP-treated lung and subtraction of the lung-specific autofluorescence, which may also depend on the quality of tissue clearance, is a prerequisite for accurate dosimetry from LSFM data (details in SI Method 1). After correction, the average fluorescence signal from blank lungs was $(10.2 \pm 1.84) \times 10^{10}$ with a standard deviation of 18%, representing the substantially improved measurement stability. Also, Figure 5a shows the linearity of a standard curve obtained from mice instilled with known NP doses ($R^2 > 0.99$). This is further proven by the gradually enhanced mean fluorescence

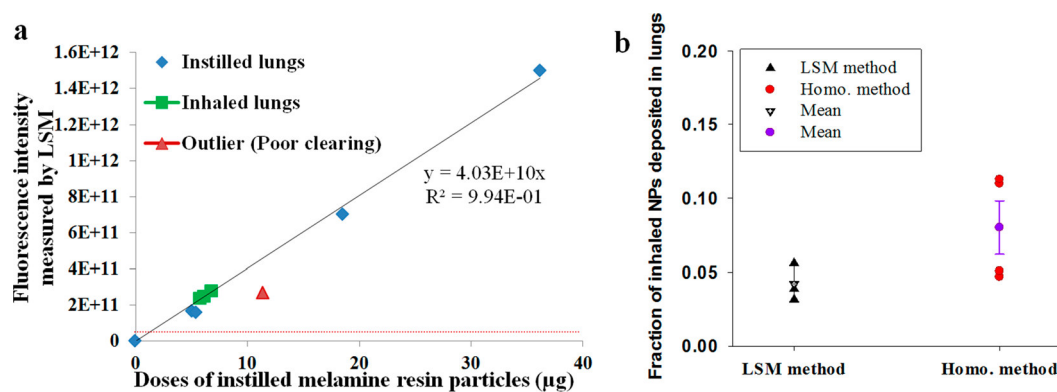


Figure 5. Establishment of the fluorescence intensity–dose correlation curve and quantitative dosimetry of inhaled doses in mouse lungs after inhalation. MF doses in inhaled lungs were determined from the linear fluorescence intensity–dose standard curve ($R^2 = 0.99$) obtained from instilled lungs with known MF doses generated from all LSM slices of the lungs (a). Poor quality of optical tissue clearing mitigates the measured NP-induced intensity, which explains the outlier of the instilled lung. The limit of detection is defined as 3-fold standard deviation (3σ) of autofluorescence about the mean autofluorescence level, which is represented by the red dashed line (a). The fraction of inhaled NPs deposited in lungs determined by the LSM method is in agreement with that from the standard fluorescence-based dosimetry method in lung homogenates (b). Abbreviations: homo: homogenization; LSMF: light sheet fluorescence microscopy.

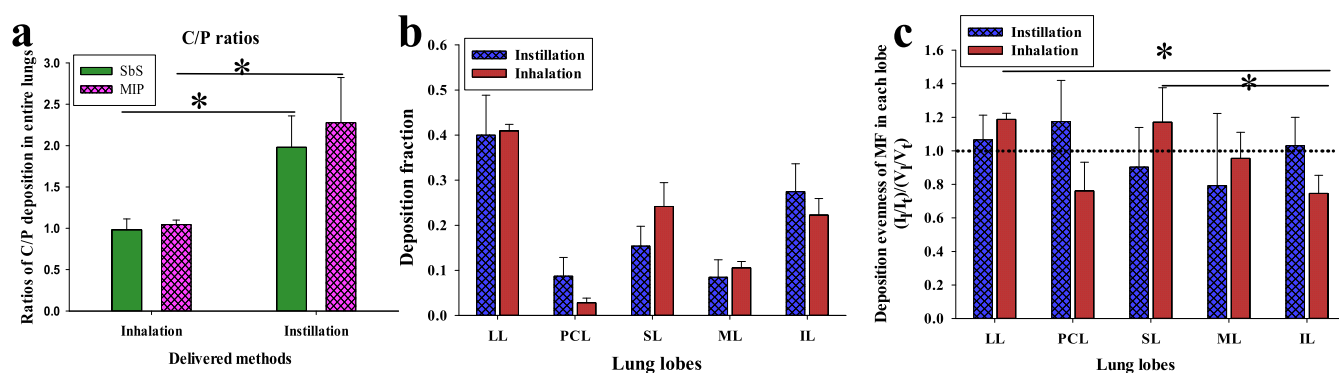


Figure 6. Quantitative analysis of MF spatial deposition in the lungs of mice after instillation and inhalation application routes. (a) Ratio of central to periphery (C/P) deposition analysis: C/P fluorescence intensity was normalized to the C/P area ratio. Lobewise deposition fraction (b, fractional MF dose in each lobe) and lobewise MF dose normalized to lobe volume (c) were analyzed for both application routes, showing that the variability in deposition fraction is consistent with lobe volume (ventilation volume). Abbreviations: Sbs: slice by slice analysis; MIP: maximum intensity projection analysis of a whole lung; LL: left lung; PCL: postcaval lobe; SL: superior lobe; ML: middle lobe; IL: inferior lobe.

intensity in MIP images containing increasing doses of MF (12.5, 25, 50 μg), as seen in Figure S5a. Poor clearing of tissue due to, for example, incomplete removal of blood during perfusion results in poor light penetration, and hence blurring reduced fluorescence intensity from the NPs, as seen as an outlier of the instilled lung in Figure 5a. The limit of detection is defined as 3-fold standard deviation (3σ) of autofluorescence about the mean autofluorescence level, which serves as a zero point.³⁹ This yields a detection limit for MF of 1.37 μg , where the 3σ intensity level was converted into mass dose using the calibration curve shown in Figure 5a. Similarly, the autofluorescence-corrected intensity signal from inhaled lungs can be used to calculate the lung deposited dose. For these three lungs investigated here we found 5.96–7.01 μg , which corresponds to $4.2\% \pm 1.3\%$ of the inhaled dose (the dose in trachea was excluded). This value was not significantly different from the $8.0\% \pm 1.8\%$, which was measured by a more accurate dosimetry method utilizing tissue homogenization (Figure 5b).⁴⁰

Quantitative assessment of the uniformity of NP distribution was performed on two scales, a central/peripheral scale (C/P; ca. 50%:50% in area) and a lobewise level, as described in the Materials and Methods section. The C/P ratio is widely used in clinical lung deposition studies using radiometric imaging.⁴¹

Here we found that inhalation resulted in a very uniform NP distribution as indicated by the C/P of 0.98 ± 0.13 , while instillation was characterized by a 2-fold enhanced central deposition (C/P = 1.98 ± 0.37) as determined by slice-by-slice analysis (Figure 6a). Interestingly, identical C/P ratios were obtained when analyzing not the whole slices of a Z-stack but only the MIP images overlaid onto the 2D projection of lung morphology (Figure S5). A more refined, lobewise analysis revealed that around 40% of the delivered NPs reached the left lung (single lobe) for both routes of application with larger variability for instillation. The remainder of about 60% deposited in the four lobes of the right lung with large lobe-specific variabilities (Figure 6b). These differences were largely consistent with differences in lobe volume (see Figure S7b for volume values). Especially instillation of NPs resulted in a volume-scaled NP distribution, as indicated by volume-normalized deposition fractions of unity within experimental uncertainties (Figure 6c). Similar results were found for inhalation of NPs, with somewhat larger deviations from unity, but still in agreement with unity for each lobe. In instilled lungs there was no significant difference in deposition fraction among all lobes, while in inhaled lungs there were elevated levels of NPs in the superior lobe and middle lobe relative to the

inferior lobe (Figure 6c). Fractional deposition of MF NPs in lung lobes and trachea (Figure S7a) for both application routes were also accomplished by this imaging method.

DISCUSSION

Accurate and spatially resolved delivery of NPs in the lungs of animal models is essential for toxicological and drug efficacy studies. Depending on the site of delivery, NPs may induce different types and levels of biological response.^{2,9,38} For instance, efficacy of a nanomedicine for lung emphysema requires delivery into the alveolar region (acini), while drugs for asthma may be more efficient if delivered to the conducting airways.⁴² Unlike the bronchial region, the acini are considered more vulnerable against inhaled NPs since it is not protected by a thick mucus layer.⁴³ Moreover, the kinetics of NPs is known to be highly dependent on the site of deposition,⁴⁴ with alveolar deposition being conducive to translocation into the bloodstream and prolonged residence time in the lung.^{45,46} In spite of the significance of NP distribution in the lung, currently available analytical methods are limited in terms of lung morphology characterization and/or NP dosimetry, especially on the whole-organ level.

The spatially resolved lung imaging method presented here addresses these issues by combining the reduction of light–tissue interactions *via* optical tissue clearing with LSFM. One of the key elements of this method is a clearing protocol for whole organs which has to be not only highly efficient with respect to time consumption and quality of optical transparency but also gentle enough to maintain tissue integrity and high quantum yield of fluorescent traces under the chemically harsh conditions of tissue clearance procedures. Here the 3DISCO²⁵ clearing protocol with modifications was used, as it was considered the most effective and time-saving organic solvent-based method (high degree of transparency within hours to days) among the recently developed optical tissue clearing methods including aqueous-based clearing methods (*e.g.*, CUBIC, SeeDB, FRUIT) and hydrogel-based clearing methods (*e.g.*, CLARITY, PACT/PARS).²⁶ Tissue clearing has been carried out in both human and animal lungs^{28,47} for studies on, for example, the development of human embryo lung airways and branches^{48–50} and macrophage infiltration in murine lung tumors.²⁴ However, there are only very few reports regarding the visualization of the distribution of NPs in intact (nonsliced) organs. For instance the CLARITY protocols have been applied to study NP localization in cleared organs other than lungs (*e.g.*, liver, spleen),^{31,51} and NPs were found mainly retained inside the vessels of a small part of liver tissue (thickness: 1 mm). Compared to the protocols presented here, CLARITY protocols not only are more complicated and time-consuming (days to weeks) but also damage or partially destroy the structural integrity of the organ.⁵² A general limitation of the tissue clearing technology is that it requires the availability of fluorescence proteins/biomolecules, dyes, and/or particles that maintain fluorescence intensity during the entire clearing protocol. For resilience testing of fluorescence tracers an easy-to-use and yet reliable *ex vivo* imaging method utilizing a low-resolution epifluorescence imaging system (IVIS) was introduced here for simultaneous testing of both fluorophore stability and tissue shrinkage/expansion during each step of the clearing protocol. In this study, three different types of NPs were tested, and metal- and resin-based NPs (QDs and MF) were found to be sufficiently stable, while polystyrene latex NPs lost their fluorescence intensity. Degradation or bleaching of fluorescence dyes can be

minimized by low-bleaching tissue clearing protocols (*e.g.*, aqueous-based clearing protocol CUBIC). There are more than 10 types of clearing protocols reported in the literature, but to the best of our knowledge most of them have not been tested for NPs, yet. We envision that *ex vivo* tissue imaging using IVIS will be a useful and robust method for selecting suitable dyes and determining tissue shrinkage/expansion during various clearing processes in future research. Moreover, this method may prove to be valuable for optimization of clearance protocols with respect to dye stability and tissue integrity.

Quantitative morphometry of the entire lung with high resolution is a challenge for both *in vivo* and *ex vivo* imaging modalities even for small animals such as mice. Simultaneous characterization of both the honeycomb arrangement of millions of alveoli and the intricate structure of the bronchial tree requires high resolution down to <10 μm combined with a large field of view up to centimeters for mice and up to tens of centimeters for humans. Basic structural parameters of the lung such as airway diameter and branching angle, MCL, and wall thickness are commonly used for diagnosing lung disease in both preclinical research and clinical settings.⁵³ For instance constricted airways are a hallmark of asthma, enlarged MCL indicates lung emphysema, and appearance of both features is known to be associated with chronic obstructive pulmonary disease (COPD).^{54,55} By far the most widely used method for lung morphometry with cellular resolution is the design-based 2D stereological methods (histomorphometry and immunofluorescence).⁵³ This approach, typically performed in HE-stained lung sections under a light microscope, allows for quantitative measurements of MCL, alveolar surface to volume ratio, wall thickness, and other parameters using a coherent test line system based on point and intersection counting utilization of the computer-assisted stereological toolbox (CAST).³³ While this method offers colocalization of NPs and tissue structure at cellular resolution, it is time-consuming due to tissue slicing, staining, and slice-by-slice microscopy, resulting in at least partial loss of 3D information. For optically cleared and transparent murine lungs LSFM allows for planewise imaging of the entire, nondissected murine lung at high resolution within a relatively short period of time (tens of minutes to hours depending on resolution). Recently, X-ray-based computed tomography (CT) is widely used for morphometric analysis in both animal models and patients due to its noninvasive and time-saving procedures.^{36,56} However, CT methods (*in vivo* or *ex vivo*) are limited in terms of resolution; they typically do not reach cellular dimensions except for *ex vivo* μCT imaging of fixed lung samples, with a resolution down to a few micrometers.⁵⁷ However, for animal models *ex vivo* LSFM imaging is much more conducive to bioactivity and functional imaging than μCT due to the much wider selection of probes with fluorescence activity than radioactivity. Thus, this study presents a label-free visualization of the entire 3D lung structure with cellular resolution and offers the morphometric analysis of both the entire bronchial tree and the alveolar structure in adult mice based on LSFM data. Airway morphometry and nerve populations in optically cleared lungs were previously visualized and computer modeled using immunostaining and BABB clearing by Scott *et al.*⁴⁷ However, the tissue deformation effect was ignored, which is essential for accurate lung morphological analysis due to the occurrence of lung deformation when the lung is out of the body (lower inflation state) and lung tissue shrinkage during BABB or 3DISCO clearing.^{28,58} The validity of a tissue shrinkage factor correcting for changes in lung

morphology due to inflation state was verified by matching the airway diameters of collapsed, unfilled *ex vivo* lungs with agar-filled, almost fully inflated lungs. In addition, it was shown that the morphometric data on airway diameters (from first order, $1048.5 \pm 94.0 \mu\text{m}$, to fourth order, $188.0 \pm 63.2 \mu\text{m}$), branching angle ($55.0^\circ \pm 14.2^\circ$), and alveolar dimension (MCL: $\sim 50 \mu\text{m}$) for W57BL/6 mice are in good agreement with literature values.^{33,35,36} Hence, tissue clearing and LSFM potentially provide the additional insights for whole lung morphometric analysis with cellular resolution including visualization and quantification of bronchial tree, alveolar sacs, and vasculature system. The use of tissue/cell-specific probes (e.g., antibodies, dyes) may even allow for cell-specific imaging on the whole-lung level.³⁰

This study further demonstrates that 3DISCO tissue clearing combined with multiwavelength LSFM allows for co-registration of NPs and lung morphology, thus yielding a 3D visualization of the NP distribution within the whole murine lungs at cellular resolution. The merit of this technique has been demonstrated by a comparison of the pulmonary NP distribution after instillation and inhalation of NPs. The accurate dosimetry of fluorescent NPs in the lung was obtained from LSFM data, as demonstrated by the linear dose–intensity curve obtained for instilled murine lungs with known NP doses. Application of this dose–intensity curve to lungs receiving an unknown NP dose *via* ventilator-assisted inhalation revealed that $4.2\% \pm 1.3\%$ of the inhaled aerosol was deposited into the lungs, which is not statistically significantly different than the $8.0\% \pm 1.8\%$ measured with an accepted reference method for lung dosimetry, namely, quantitative fluorescence analysis in lung homogenates.⁴⁰ Finally, LSFM images provided both qualitative and quantitative evidence for the expected finding that inhalation of aerosolized NPs results in more uniformly distributed pulmonary NP distribution than instillation. In addition to the obviously more patchy NP deposition in instilled lungs (Figure 3a and b) the quantitative analysis of the ratio of centrally and peripherally deposited NP dose showed that instillation resulted in about a 2-fold enhanced central deposition relative to peripheral deposition ($C/P \approx 2$), while inhalation provided a uniform distribution of NPs ($C/P \approx 1$). This is to be expected, since liquid bolus application is not expected to reach the peripheral lung regions as well as inhalation of aerosolized NPs, which is known to result in C/P ratios near unity not only in animal models but also in humans.⁴¹ The order of NP deposition among lobes and *ca.* 40% inhaled aerosols reached in the left lung was determined by the lobewise deposition analysis, which is also consistent with the previous findings that used fluorescent (compressed) lung imaging.^{59,60} Furthermore, after inhalation the acinar deposition showed a strong proximal to distal gradient, where roughly the proximal half received most of the NPs and the distal one much less to no NPs (Figure 3b). This pattern is of particular interest, because it was predicted by computational fluid dynamics simulations that the proximally located alveolar ducts serve as a filter for particles and strongly decrease any distal deposition.⁶¹ Our data represent the visualizations of the predicted deposition pattern in living animals, and they verify the simulation *in vivo*. It is obvious that any uneven distribution of NP deposition is highly relevant for therapeutic and toxic effects. We note that some aspects of the NP deposition pattern reported here for mechanically ventilated, deeply anesthetized mice are likely to be different for nonventilated, spontaneously breathing or more mildly anesthetized mice, but the general trend of more spatially

uniform NP deposition *via* inhalation *versus* intratracheal instillation has also been found in spontaneously inhaling animals.^{59,60}

These features represent substantial progress over previously used *in vivo* and *ex vivo* optical imaging modalities, which were mainly suitable for the semiquantitative determination of dose and biodistribution of NPs in the tissue due to limitations with respect to strong tissue autofluorescence and poor spatial resolution.⁹ For example, cryo-slicing fluorescence imaging³⁹ can be used for quantitative dosimetry and 3D distribution in murine lungs, but with much worse resolution than possible with LSFM. Other nonoptical imaging techniques for detection of NP biodistribution, quantification, and biokinetics are available at the *in vivo* (e.g., X-ray-based imaging, SPECT, PET, MRI) and *ex vivo* levels (e.g., TEM, SEM, flow cytometry, 2D stereology), as summarized in recent reviews.^{2,9,21,62} Application of those *in vivo* methods usually requires expensive instrumentation and the use of radiolabeling and/or contrast agents while providing limited spatial resolution. This greatly restricts observation of biological processes such as cellular uptake of NPs as well as generation of inflammation and reactive oxygen species, which is within reach of the method presented here. On the other hand, the *ex vivo* histological methods listed above allow for cellular resolution, but they are time-consuming, not suitable for whole-organ imaging, and insufficient for NP dosimetry. The imaging method for label-free lung morphometry analysis combined with quantitative NP distribution with cellular resolution on a tissue section overcomes some of these limitations, offering deep insights into 3D mapping of NP distributions in large tissue sections and organs with up to *ca.* 2 cm thickness, exceeding by far previously reported penetration depths.³¹ Optical visualization of ultrafine NP and agglomerates (<100 nm diameter) is always challenging using fluorescence microscopy, as explained by two recent reviews.^{21,62} We also note that not only fluorescence but alternative optical modalities such as light scattering can provide 3D imaging of metal NPs in intact and transparent tissues.⁶³ Future studies should exploit multiple staining probes for multifunctional biological response analysis with time-resolved LSFM to further refine this methodology for NP biokinetics, toxicology, and efficacy studies, facilitating the development of nanotoxicology and nanomedicine.

CONCLUSION

In this study, we presented and validated an *ex vivo* whole-tissue imaging method for 3D quantitative co-visualization of (label-free) airway morphology and biodistribution of fluorescent nanoparticles with cellular resolution in murine lungs. Moreover, *ex vivo* whole murine lung imaging using epifluorescence imaging (here: IVIS) was introduced as a time-efficient and reliable method for analysis of the preservation of fluorescent dyes and lung morphology during the chemically harsh procedure of optical tissue clearing. Here 3DISCO tissue clearing and bispectral light sheet fluorescence microscopy were combined to co-visualize the label-free, entire 3D lung architecture (trachea to alveolar sacs) and pulmonary distribution of fluorescent NPs in nondissected, whole murine lungs (with an imaging depth of 1–2 cm for wavelengths of 500–750 nm). The method allows for quantitative NP dosimetry and reveals clear differences in the biodistribution of NPs applied to the lungs as bulk liquid suspension *via* intratracheal instillation or as a cloud of droplets (aerosol) *via* ventilator-assisted inhalation under anesthetized conditions on various resolution levels ranging from central-to-peripheral, to

lobewise, to cellular. Taken together, the approach presented here represents a robust method for single-modality analysis of combined 3D lung morphometry and quantitative biodistribution analysis of fluorescent probes (molecular, NP-bound) for the advanced analysis of biodistribution, biokinetics, and bioresponse analysis of NPs in whole murine lungs or whole-tissue sections and even small organisms.

MATERIALS AND METHODS

Materials. Three types of commercial fluorescence-labeled NPs were used for the experiments, namely, polystyrene NPs with the embedded fluorescence dye Sky Blue (ex/em = 670 nm/710 nm; volume median diameter (VMD): 481 nm; Kisker Biotech GmbH, Steinfurt, Germany), MF fluorescence particles (MF, ex/em = 636 nm/686 nm; VMD: 474 nm, microParticles GmbH, Berlin, Germany), and Qdot 800 ITK carboxyl quantum dots (QDs with the maximum emission spectrum around 800 nm; VMD: 18 nm, Invitrogen, Ltd., Paisley, UK). The Syke Blue NPs (stock suspension: 10 mg/mL) were found to be unstable in the 3DISCO tissue clearing process and will therefore not appear in any of the images presented below. The MF NPs (stock suspension: 25 mg/mL) were prepared *via* an acid-catalyzed polycondensation reaction of melamine resin precondensates in the presence of selected fluorescent dyes in the aqueous phase. QDs (stock solution: 8 μ M) were made from the crystals of a semiconductor material (CdSeTe), shelled with a ZnS layer, and further coated with a polymer layer with carboxyl surface groups. Hydrodynamic diameter measurement of all three NPs was performed with dynamic light scattering (DLS) using a Malvern Zeta Sizer Nano instrument (Malvern Instruments Ltd., Malvern, UK).

Animal Handling. Mice were housed in individually ventilated cages (IVC-Racks; Bio-Zone, Margate, UK) supplied with filtered air in a 12 h light/12 h dark cycle (lights on from 06:00–18:00). The animals were provided with food (standard chow) and water *ad libitum*. All procedures involving animal handling and experiments were carried out in accordance with protocols approved by the Regierung von Oberbayern (District Government of Upper Bavaria).

Wild-type C57BL/6 mice (age 16–25 weeks, 6 males and 15 females, weight 20–30 g) were used for these experiments. Twenty-one mice were randomly divided into four groups: MF group (7 mice for instillation and 3 mice for inhalation); QDs group (3 female mice for instillation); Sky Blue group (3 female mice for instillation); and vehicle control group (3 females and 2 males without NPs treatment). For instillation, mice were anesthetized by the intraperitoneal injection of a ketamine and xylazine mixture and intubated by a nonsurgical technique using a 20G cannula inserted into the trachea, as previously described.^{39,64} For intubated-ventilated inhalation exposure, the animals were deeply anesthetized by intraperitoneal injection with a triple combination of medetomidine (0.5 mg/kg bodyweight), midazolam (5 mg/kg bodyweight), and fentanyl (0.05 mg/kg bodyweight) and cannula intubated as described for instillation. The cannula was attached to a mechanical ventilator for mice (flexiVent system, SciReq Inc., Canada) to control their respiration during aerosol inhalation. The flexiVent was equipped with a nebulizer (Aeroneb Lab, small droplet diameter (2.5–4.0 μ m), Aerogen Inc., Ireland) for the generation of liquid aerosol droplets consisting of NP suspensions. For each mouse, the nebulizer was filled with 20, 40, or 60 μ L of a 12.5 mg/mL MF suspension (1:2 dilution of stock suspension) and the nebulizer was active for 40 ms per breath during ventilation of the mouse with 120 breaths/min, 400 μ L tidal volume, and an inhalation–exhalation time ratio of 2:1. The mouse was sacrificed immediately after NP application by exsanguination (to avoid clearance of NPs from the respiratory tract) and then transcidentally perfused with 20 mL of 0.1 M phosphate-buffered saline (PBS) at room temperature for flushing out all of the blood from the lung. Subsequently, the perfusion liquid was switched to the fixation solution 4% paraformaldehyde (PFA) in 0.1 M PBS (10 mL) and then the whole lung plus the esophagus were removed and postfixed in 4% PFA overnight. The harvested organ was kept in 0.1 M PBS until further processing (imaging). Notably, 2 of 7 instilled mice were sacrificed at 24 h after application of MF NPs. Both mice were

transcidentally perfused with 20 mL of 0.1 M PBS, and then their lungs were filled with 4% PFA for 2 h fixation *via* the cannula-intubated trachea. Subsequently, the PFA was withdrawn and refilled through the cannula with 0.8–1 mL of warm, 0.1 M PBS-equilibrated 2% agar, which was subsequently cooled to stiffen the lung tissue and thus maintain the inflated state of the lungs.⁵⁴

Ex Vivo Whole-Lung Imaging Using IVIS. To examine the fluorescence stability of the NPs and the morphometric integrity of the lung during optical tissue clearance, an efficient, simple, and time-saving (less than 1 min for an *ex vivo* lung imaging) *ex vivo* imaging was performed using the IVIS (Lumina II, Caliper/PerkinElmer, USA). Briefly, the entire lung was placed on a holder located centrally in the IVIS with NP-specific excitation and emission filters (for Sky Blue and MF ex/em = 640 nm/Cy5.5 and for QDs ex/em = 640 nm/ICG) for various time points during the tissue clearance procedures. For each time point the fluorescence intensity and the 2D projected geometric area of the lung were determined from the fluorescence/white light images with the Living Imaging 4.0 software (Caliper). The variations in fluorescence intensity and the projected lung area (as a measure of lung morphometry) revealed the degree of resilience of the NPs against chemical degradation during the 3DISCO clearing protocol and morphometric stability (expressed as area shrinkage factor of lung), respectively.

Tissue Clearing and 3D Imaging. Whole-lung clearing was performed according to a modified version of the 3DISCO protocol.²⁵ Briefly, samples were dehydrated in 10 mL of 50% v/v tetrahydrofuran/H₂O overnight (THF, Sigma 186562-1L), 50% THF/H₂O 1 h, 70% THF/H₂O 4 h, 80% THF/H₂O 4 h, 100% THF 1 h, 100% THF overnight, and 100% THF 1 h with slight shaking. Samples were gently dried and then incubated in DCM (Sigma 270997-1L) around 30–40 min until they sank to the bottom of the 50 mL conical tube (Corning, Falcon 352070). Finally, samples were incubated without shaking in BABB, a mixture of 1:2 v/v benzyl alcohol (BA, Sigma 305197-1L) and benzyl benzoate (BB, Sigma B6630-1L), or in DBE (Sigma 108014-1KG) for at least 2 h until imaging and could then be stored in DBE/BABB at room temperature.

Whole-lung samples were imaged with an LSM (Ultramicroscope II, LaVision Biotec) equipped with a sCMOS camera (Andor Neo) and a 2 \times objective lens (Olympus MVPLAPO 2 \times /0.5 NA) equipped with an Olympus MVX-10 zoom body, which provided zoom-out and -in ranging from 0.63 \times up to 6.3 \times . For whole lungs of mice treated with Sky Blue or MF NPs, light sheet scans were generated with 0.63 \times zoom magnification (lens+zoom, 1.26 \times actual magnification) with different excitation and emission bandpass filters (ex/em = 640(30) nm/690(50) nm for Sky Blue and MF NPs; ex/em = 640(30) nm/795(50) nm for QDs; ex/em = 545(30) nm/605(70) nm for tissue autofluorescence for lung morphology measurement) with a step size of 10 or 20 μ m depending on sample size. Samples were generally imaged with a exposure time of 150 ms, at 100% laser power (80% laser power only used when epifluorescence was overqualified) with the light sheet (thickness 4–24 μ m) at different *xy* widths and numerical apertures (NA) depending mainly on the magnification of the image. Samples were also imaged at magnifications of 8 \times (Figure 3c) and 12.6 \times (Figure 4) using a 4–5 μ m Z-step. The LSM imaging time for a whole lung usually takes between tens of minutes and a few hours depending on various parameters including sample size (here stack size *ca.* 6–10 mm), magnification, light beam (dual or single), and step size. For refractive index matching, the imaging chamber of the LSM was filled with BABB or DBE, the final clearing solvent used for tissue clearing.

Image Processing and Analysis. The images shown in the figures including single-slice images and maximum intensity projection (a method for 3D data visualization that displays only the voxels with maximum intensity along each optical ray passing through the image stack in the projection image⁶⁵) images were processed by ImageJ (<https://imagej.nih.gov/ij/>). 3D volume images and movies with 3D manipulation were generated using Bitplane Imaris (<http://www.bitplane.com/Imaris/Imaris>). Lung morphometry such as airway diameter and bifurcation angle was manually segmented and calculated in 3D using Imaris. The alveolar MCL was estimated directly by setting

up random test lines consisting of solid lines and dashed lines superimposed on 2D images using ImageJ as described in the literature.^{33,53} The airway diameters and MCL of unfilled lungs should be corrected for deformation effects due to tissue shrinkage during optical clearing and differences in inflation state of the lung. The (1D) shrinkage factor of the former (1.27 for collapsed lung), which was only applied to airspaces from the second-order bronchus to more distal regions (strong cartilage in more proximal regions), was determined from the square root of the 2D area shrinkage factor as measured from IVIS images of the lung before and after tissue clearing. The deflation correction factor, which was applied to the bronchioles and MCL, was determined from the volume ratio of the inflated (0.8 mL agar + 0.3 mL residual lung volume) and deflated lung (0.3 mL),^{59,60} yielding 1.54 ($= (1.1/0.3)^{1/3}$). So the total correction factor applied to the collapsed lung is 1.27 for second- and third-order bronchi and 1.96 ($= 1.27 \times 1.54$) for bronchioles and MLC. Surface rendering of the mouse bronchial tree was derived from the autofluorescence signal of the airways of blank (unexposed) lungs in all ex/em channels, and spot rendering of NPs in Figure 3c with a filter size of 5.5 μm were also prepared using Imaris.

Establishment of the Intensity–Dose Standard Curve for NP Dosimetry. Quantitative analysis of the images recorded by LSFM requires accurate assessment of various sources of error including instrument biases and variations of lung optical properties. In order to achieve reliable NP dosimetry, the absolute fluorophore intensity in each NP-treated lung was calculated following total fluorescence correction and subtraction of tissue-induced autofluorescence signal (for detailed descriptions see SI method 1). The dose of fluorescent NPs in a whole lung should be principally proportional to the sum of the absolute fluorescence intensities from all LSFM slices. The conversion factor of the corrected absolute fluorophore intensity to the fluorophore dose can be determined by preparing instilled lungs with known but different amounts of NPs (50 μL of 1:200, 1:100, 1:50, and 1:25 dilutions of MF stock solution). After yielding the desired fluorescence intensity–dose conversion curve (here a linear relationship was obtained), quantitative measurement of the deposited dose in the lungs of mice *via* inhalation exposure could be achieved. The inhaled NP dose in the lungs of mice *via* intubated inhalation exposure was determined by differential gravimetric analysis of the nebulizer including connecting tubing to the mouse prior to and after nebulization (here $36.0 \pm 8.5\%$ of invested dose can be inhaled), and but only a small fraction of inhaled dose can reach the lung (Figure 4b).

C/P and Lobewise Distribution Analysis. The regional deposition of NPs in the lung was investigated on two scales, a two-region (central and peripheral region) and a lobewise approach. For the clinically widely used two-region approach, the area-normalized NP dose in a central and peripheral area is determined from single lung slices added over all slices or from a maximum intensity projection of the entire lung. The central region is defined as the circumference-shaped matched inner 50% of each lung slice, and the entire lung area in each image (slice) was determined by intensity thresholding. Subtraction of the fluorescence intensity of the central region from that of the total lung region yields the peripheral lung intensity, and the ratio of central to peripheral intensity was analyzed after total fluorescence correction and subtraction of tissue autofluorescence (details in SI method 2) and then normalized to the respective areas according to

$$C/P = \frac{I_c/I_p}{A_c/A_p}$$

where I_c and I_p refer to the absolute NP fluorescence intensities from the central and peripheral regions of lung slices, respectively. A_c and A_p are the areas in the center and periphery, respectively. Slice-by-slice A_c and A_p analysis was performed on every fourth slice of each lung stack excluding the top and bottom slices of a stack, which contained predominantly peripheral regions. The overall C/P ratio determined by averaging over all analyzed slices indicates the homogeneity of the dose deposition. C/P close to unity denotes a homogeneous fluorophore

distribution in the lung, whereas C/P larger than unity indicates preferential central airway deposition.

Moreover, lobewise analysis was also performed to reveal the uniformity of NP distribution among lung lobes for both application routes. First, the entire region outside the lung was automatically set to zero (intensity thresholding), and then the region of interest representing the individual lobe was selected manually based on recognition of the space between two adjacent lobes. Subsequently, the fractional deposition of NPs on all five lung lobes and the trachea was obtained using ImageJ. Uniformity of MF deposition was described as volume- (lung/lobe volume estimated using the Cavalieri principle)⁶⁶ normalized intensity signal for each lobe after total fluorescence correction and lobe-specific subtraction of tissue autofluorescence. The volume-normalized deposition fraction is calculated from

$$\text{Dep}_v = \frac{I_l/I_t}{V_l/V_t}$$

where I_l and I_t refer to the NP-triggered fluorescence intensity from a specific lobe (here: 5 lobes) and the total lung, respectively. Analogous V_l and V_t are the volumes of a specific lobe and the total lung (without trachea), respectively. Dep_v is close to 1 if the NP dose reaching a specific lobe is equal to the fractional lung volume of this lobe. Values larger and lower than unity indicate preferential or reduced NP deposition in this specific lobe.

Fluorescence-Based Analysis of NP Dose in Lung Homogenates. As a reference method for NP dosimetry, we also determined the NP tissue burden in the total lung (all five lobes together), trachea, and esophagus according to a previously described method relying on quantitative fluorescence analysis in homogenized tissue.⁴⁰ In brief, tissue samples were homogenized in a homogenizer (Ultra Torrax, 20000 rpm) at a 1:10 (m/v) ratio of tissue to 0.1 M PBS buffer. A standard curve relating fluorescence intensity and NP concentration in lung homogenates was established by using a series of known doses of MF added into the homogenates of blank lung tissue allowing for quantification of the NP dose in the tissue.

Statistical Analysis. The statistical analysis was performed using SigmaPlot version 12.0 (Systat Software GmbH, Germany). Normality was determined using the Shapiro–Wilk test and a visual assessment of histograms. Comparison results from two groups for normally distributed and non-normally distributed data were carried out using a two-sided Student's *t* test and a Mann–Whitney rank sum test, respectively. Comparisons among multiple groups were performed using a one-way analysis of variance (ANOVA) followed by a pairwise multiple comparison procedures (Holm–Sidak method). All data were presented as mean \pm SD. Significances are defined as 0.05 ($P < 0.05$, *) and 0.01 ($P < 0.01$, **).

ASSOCIATED CONTENT

Supporting Information

The Supporting Information is available free of charge on the ACS Publications website at DOI: 10.1021/acsnano.8b07524.

Videos on co-visualization of lung morphology and nanoparticle distribution (ZIP)

Additional information including video captions (PDF)

AUTHOR INFORMATION

Corresponding Author

*E-mail: otmar.schmid@helmholtz-muenchen.de. Tel: +49-89-3187-2557. Fax: +49-89-3187-2400.

ORCID

Lin Yang: 0000-0003-0469-9288

Author Contributions

L.Y., A.F., W.M., Y.D., D.K., G.M., J.C.S., G.B., W.H., T.S., D.R., A.W., and O.S. conceived and designed experiments. L.Y., A.F., W.M., Y.D., and D.K. carried out experiments. A.F. and G.B.

assisted in imaging using light sheet microscopy and confocal microscopy, respectively. J.C.S. and W.M. contributed to the interpretation of imaging data. L.Y., A.F., and O.S. analyzed data and drafted the manuscript. All authors read and approved the final manuscript.

Notes

The authors declare no competing financial interest.

ACKNOWLEDGMENTS

This research was (partially) supported through the EU Horizon 2020 project SmartNanoTox, grant agreement no. 686098, and Swiss National Science Foundation, grant no. 310030_175953. We thank the China Scholarship Council (CSC) for providing the fellowship for L.Y. (201506820008).

REFERENCES

- (1) Wagner, V.; Dullaart, A.; Bock, A. K.; Zweck, A. The Emerging Nanomedicine Landscape. *Nat. Biotechnol.* **2006**, *24*, 1211–1217.
- (2) Pelaz, B.; Alexiou, C. H.; Alvarez-Puebla, R. A.; Alves, F.; Andrews, A. M.; Ashraf, S.; Balogh, L. P.; Ballerini, L.; Bestetti, A.; Brendel, C.; Bosi, S.; Carril, M.; Chan, W. C. W.; Chen, C. Y.; Chen, X. D.; Chen, X. Y.; Cheng, Z.; Cui, D. X.; Du, J. Z.; Dullin, C.; et al. Diverse Applications of Nanomedicine. *ACS Nano* **2017**, *11*, 2313–2381.
- (3) Ding, Y.; Kuhlbusch, T. A. J.; Van Tongeren, M.; Jimenez, A. S.; Tuinman, I.; Chen, R.; Alvarez, I. L.; Mikolajczyk, U.; Nickel, C.; Meyer, J.; Kaminski, H.; Wohlleben, W.; Stahlmecke, B.; Clavaguera, S.; Riediker, M. Airborne Engineered Nanomaterials in the Workplace—a Review of Release and Worker Exposure During Nanomaterial Production and Handling Processes. *J. Hazard. Mater.* **2017**, *322*, 17–28.
- (4) WHO. *WHO Guidelines on Protecting Workers from Potential Risks of Manufactured Nanomaterials*; Geneva, 2017; 94.
- (5) Lelieveld, J.; Evans, J. S.; Fnais, M.; Giannadaki, D.; Pozzer, A. The Contribution of Outdoor Air Pollution Sources to Premature Mortality on a Global Scale. *Nature* **2015**, *525*, 367–371.
- (6) Traboulsi, H.; Guerrina, N.; Iu, M.; Maysinger, D.; Ariya, P.; Baglolo, C. J. Inhaled Pollutants: The Molecular Scene Behind Respiratory and Systemic Diseases Associated with Ultrafine Particulate Matter. *Int. J. Mol. Sci.* **2017**, *18*, 243.
- (7) Mura, S.; Nicolas, J.; Couvreur, P. Stimuli-Responsive Nanocarriers for Drug Delivery. *Nat. Mater.* **2013**, *12*, 991–1003.
- (8) Chan, W. C. W. Nanomedicine 2.0. *Acc. Chem. Res.* **2017**, *50*, 627–632.
- (9) Kunjachan, S.; Ehling, J.; Storm, G.; Kiessling, F.; Lammers, T. Noninvasive Imaging of Nanomedicines and Nanotheranostics: Principles, Progress, and Prospects. *Chem. Rev.* **2015**, *115*, 10907–10937.
- (10) Stoeger, T.; Takenaka, S.; Frankenberger, B.; Ritter, B.; Karg, E.; Maier, K.; Schulz, H.; Schmid, O. Deducing *in Vivo* Toxicity of Combustion-Derived Nanoparticles from a Cell-Free Oxidative Potency Assay and Metabolic Activation of Organic Compounds. *Environ. Health Perspect.* **2009**, *117*, 54–60.
- (11) Ganguly, K.; Etehadieh, D.; Upadhyay, S.; Takenaka, S.; Adler, T.; Karg, E.; Krombach, F.; Kreyling, W. G.; Schulz, H.; Schmid, O.; Stoeger, T. Early Pulmonary Response Is Critical for Extra-Pulmonary Carbon Nanoparticle Mediated Effects: Comparison of Inhalation Versus Intra-Arterial Infusion Exposures in Mice. *Part. Fibre Toxicol.* **2017**, *14*, 19.
- (12) Bakand, S.; Hayes, A. Toxicological Considerations, Toxicity Assessment, and Risk Management of Inhaled Nanoparticles. *Int. J. Mol. Sci.* **2016**, *17*, 929.
- (13) Pacurari, M.; Lowe, K.; Tchounwou, P. B.; Kafoury, R. A Review on the Respiratory System Toxicity of Carbon Nanoparticles. *Int. J. Environ. Res. Public Health* **2016**, *13*, 325.
- (14) Choi, H. S.; Ashitate, Y.; Lee, J. H.; Kim, S. H.; Matsui, A.; Insin, N.; Bawendi, M. G.; Semmler-Behnke, M.; Frangioni, J. V.; Tsuda, A. Rapid Translocation of Nanoparticles from the Lung Airspaces to the Body. *Nat. Biotechnol.* **2010**, *28*, 1300–1304.
- (15) Schmid, O.; Stoeger, T. Surface Area Is the Biologically Most Effective Dose Metric for Acute Nanoparticle Toxicity in the Lung. *J. Aerosol Sci.* **2016**, *99*, 133–143.
- (16) Maynard, A. D.; Kuempel, E. D. Airborne Nanostructured Particles and Occupational Health. *J. Nanopart. Res.* **2005**, *7*, 587–614.
- (17) Miller, M. R.; Raftis, J. B.; Langrish, J. P.; McLean, S. G.; Samutrtai, P.; Connell, S. P.; Wilson, S.; Vesey, A. T.; Fokkens, P. H. B.; Boere, A. J. F.; Krystek, P.; Campbell, C. J.; Hadoke, P. W. F.; Donaldson, K.; Cassee, F. R.; Newby, D. E.; Duffin, R.; Mills, N. L. Inhaled Nanoparticles Accumulate at Sites of Vascular Disease. *ACS Nano* **2017**, *11*, 4542–4552.
- (18) Schmid, O.; Cassee, F. R. On the Pivotal Role of Dose for Particle Toxicology and Risk Assessment: Exposure Is a Poor Surrogate for Delivered Dose. *Part. Fibre Toxicol.* **2017**, *14*, 52.
- (19) Kreyling, W. G.; Hirn, S.; Möller, W.; Schleh, C.; Wenk, A.; Celik, G.; Lipka, J.; Schaffler, M.; Haberl, N.; Johnston, B. D.; Sperling, R.; Schmid, G.; Simon, U.; Parak, W. J.; Semmler-Behnke, M. Air-Blood Barrier Translocation of Tracheally Instilled Gold Nanoparticles Inversely Depends on Particle Size. *ACS Nano* **2014**, *8*, 222–233.
- (20) Yang, L.; Kuang, H.; Zhang, W.; Wei, H.; Xu, H. Quantum Dots Cause Acute Systemic Toxicity in Lactating Rats and Growth Restriction of Offspring. *Nanoscale* **2018**, *10*, 11564–11577.
- (21) Vanhecke, D.; Rodriguez-Lorenzo, L.; Clift, M. J. D.; Blank, F.; Petri-Fink, A.; Rothen-Rutishauser, B. Quantification of Nanoparticles at the Single-Cell Level: An Overview About State-of-the-Art Techniques and Their Limitations. *Nanomedicine* **2014**, *9*, 1885–1900.
- (22) Yang, L.; Kuang, H.; Zhang, W.; Aguilar, Z. P.; Wei, H.; Xu, H. Comparisons of the Biodistribution and Toxicological Examinations after Repeated Intravenous Administration of Silver and Gold Nanoparticles in Mice. *Sci. Rep.* **2017**, *7*, 3303.
- (23) Dawidczyk, C. M.; Kim, C.; Park, J. H.; Russell, L. M.; Lee, K. H.; Pomper, M. G.; Searson, P. C. State-of-the-Art in Design Rules for Drug Delivery Platforms: Lessons Learned from Fda-Approved Nanomedicines. *J. Controlled Release* **2014**, *187*, 133–144.
- (24) Cuccarese, M. F.; Dubach, J. M.; Pfirschke, C.; Engblom, C.; Garris, C.; Miller, M. A.; Pittet, M. J.; Weissleder, R. Heterogeneity of Macrophage Infiltration and Therapeutic Response in Lung Carcinoma Revealed by 3d Organ Imaging. *Nat. Commun.* **2017**, *8*, 14293.
- (25) Erturk, A.; Becker, K.; Jahrling, N.; Mauch, C. P.; Hojer, C. D.; Egen, J. G.; Hellal, F.; Bradke, F.; Sheng, M.; Dodt, H. U. Three-Dimensional Imaging of Solvent-Cleared Organs Using 3disco. *Nat. Protoc.* **2012**, *7*, 1983–1995.
- (26) Feuchtinger, A.; Walch, A.; Dobosz, M. Deep Tissue Imaging: A Review from a Preclinical Cancer Research Perspective. *Histochem. Cell Biol.* **2016**, *146*, 781–806.
- (27) Stelzer, E. H. K. Light-Sheet Fluorescence Microscopy for Quantitative Biology. *Nat. Methods* **2015**, *12*, 23–26.
- (28) Susaki, E. A.; Ueda, H. R. Whole-Body and Whole-Organ Clearing and Imaging Techniques with Single-Cell Resolution: Toward Organism-Level Systems Biology in Mammals. *Cell Chem. Biol.* **2016**, *23*, 137–157.
- (29) Renier, N.; Wu, Z.; Simon, D. J.; Yang, J.; Ariel, P.; Tessier-Lavigne, M. Idisco: A Simple, Rapid Method to Immunolabel Large Tissue Samples for Volume Imaging. *Cell* **2014**, *159*, 896–910.
- (30) Klingberg, A.; Hasenberg, A.; Ludwig-Portugall, I.; Medyukhina, A.; Mann, L.; Brenzel, A.; Engel, D. R.; Figge, M. T.; Kurts, C.; Gunzer, M. Fully Automated Evaluation of Total Glomerular Number and Capillary Tuft Size in Nephritic Kidneys Using Lightsheet Microscopy. *J. Am. Soc. Nephrol.* **2017**, *28*, 452–459.
- (31) Sindhvani, S.; Syed, A. M.; Wilhelm, S.; Glancy, D. R.; Chen, Y. Y.; Dobosz, M.; Chan, W. C. Three-Dimensional Optical Mapping of Nanoparticle Distribution in Intact Tissues. *ACS Nano* **2016**, *10*, 5468–5478.
- (32) Wallau, B. R.; Schmitz, A.; Perry, S. F. Lung Morphology in Rodents (Mammalia, Rodentia) and Its Implications for Systematics. *J. Morphol.* **2000**, *246*, 228–248.

- (33) Knudsen, L.; Weibel, E. R.; Gundersen, H. J.; Weinstein, F. V.; Ochs, M. Assessment of Air Space Size Characteristics by Intercept (Chord) Measurement: An Accurate and Efficient Stereological Approach. *J. Appl. Physiol.* **2010**, *108*, 412–421.
- (34) Soutiere, S. E.; Mitzner, W. On Defining Total Lung Capacity in the Mouse. *J. Appl. Physiol.* **2004**, *96*, 1658–1664.
- (35) Thiesse, J.; Namati, E.; Sieren, J. C.; Smith, A. R.; Reinhardt, J. M.; Hoffman, E. A.; McLennan, G. Lung Structure Phenotype Variation in Inbred Mouse Strains Revealed through *in Vivo* Micro-Ct Imaging. *J. Appl. Physiol.* **2010**, *109*, 1960–1968.
- (36) Counter, W. B.; Wang, I. Q.; Farncombe, T. H.; Labiris, N. R. Airway and Pulmonary Vascular Measurements Using Contrast-Enhanced Micro-Ct in Rodents. *Am. J. Physiol.-Lung C* **2013**, *304*, L831–L843.
- (37) Geiser, M. Update on Macrophage Clearance of Inhaled Micro- and Nanoparticles. *J. Aerosol Med. Pulm. Drug Delivery* **2010**, *23*, 207–217.
- (38) Kreyling, W. G.; Möller, W.; Holzwarth, U.; Hirn, S.; Wenk, A.; Schleh, C.; Schaffler, M.; Haberl, N.; Gibson, N.; Schittny, J. C. Age-Dependent Rat Lung Deposition Patterns of Inhaled 20 Nanometer Gold Nanoparticles and Their Quantitative Biokinetics in Adult Rats. *ACS Nano* **2018**, *12*, 7771–7790.
- (39) Barapatre, N.; Symvoulidis, P.; Möller, W.; Prade, F.; Deliolanis, N. C.; Hertel, S.; Winter, G.; Yildirim, A. O.; Stoeger, T.; Eickelberg, O.; Ntziachristos, V.; Schmid, O. Quantitative Detection of Drug Dose and Spatial Distribution in the Lung Revealed by Cryoslicing Imaging. *J. Pharm. Biomed. Anal.* **2015**, *102*, 129–136.
- (40) van Rijt, S. H.; Bolukbas, D. A.; Argyo, C.; Wipplinger, K.; Naureen, M.; Datz, S.; Eickelberg, O.; Meiners, S.; Bein, T.; Schmid, O.; Stoeger, T. Applicability of Avidin Protein Coated Mesoporous Silica Nanoparticles as Drug Carriers in the Lung. *Nanoscale* **2016**, *8*, 8058–8069.
- (41) Möller, W.; Felten, K.; Meyer, G.; Meyer, P.; Seitz, J.; Kreyling, W. G. Corrections in Dose Assessment of 99mTc Radiolabeled Aerosol Particles Targeted to Central Human Airways Using Planar Gamma Camera Imaging. *J. Aerosol Med. Pulm. Drug Delivery* **2009**, *22*, 45–54.
- (42) Dolovich, M. B.; Dhand, R. Aerosol Drug Delivery: Developments in Device Design and Clinical Use. *Lancet* **2011**, *377*, 1032–1045.
- (43) Button, B.; Cai, L. H.; Ehre, C.; Kesimer, M.; Hill, D. B.; Sheehan, J. K.; Boucher, R. C.; Rubinstein, M. A Periciliary Brush Promotes the Lung Health by Separating the Mucus Layer from Airway Epithelia. *Science* **2012**, *337*, 937–941.
- (44) Semmler-Behnke, M.; Takenaka, S.; Fertsch, S.; Wenk, A.; Seitz, J.; Mayer, P.; Oberdorster, G.; Kreyling, W. G. Efficient Elimination of Inhaled Nanoparticles from the Alveolar Region: Evidence for Interstitial Uptake and Subsequent Reentrainment onto Airway Epithelium. *Environ. Health Perspect.* **2007**, *115*, 728–733.
- (45) Kreyling, W. G.; Semmler-Behnke, M.; Seitz, J.; Scymczak, W.; Wenk, A.; Mayer, P.; Takenaka, S.; Oberdorster, G. Size Dependence of the Translocation of Inhaled Iridium and Carbon Nanoparticle Aggregates from the Lung of Rats to the Blood and Secondary Target Organs. *Inhalation Toxicol.* **2009**, *21*, 55–60.
- (46) Möller, W.; Felten, K.; Sommerer, K.; Scheuch, G.; Meyer, G.; Meyer, P.; Haussinger, K.; Kreyling, W. G. Deposition, Retention, and Translocation of Ultrafine Particles from the Central Airways and Lung Periphery. *Am. J. Respir. Crit. Care Med.* **2008**, *177*, 426–432.
- (47) Scott, G. D.; Blum, E. D.; Fryer, A. D.; Jacoby, D. B. Tissue Optical Clearing, Three-Dimensional Imaging, and Computer Morphometry in Whole Mouse Lungs and Human Airways. *Am. J. Respir. Cell Mol. Biol.* **2014**, *51*, 43–55.
- (48) Belle, M.; Godefroy, D.; Couly, G.; Malone, S. A.; Collier, F.; Giacobini, P.; Chedotal, A. Tridimensional Visualization and Analysis of Early Human Development. *Cell* **2017**, *169*, 161–173.
- (49) Susaki, E. A.; Tainaka, K.; Perrin, D.; Yukinaga, H.; Kuno, A.; Ueda, H. R. Advanced Cubic Protocols for Whole-Brain and Whole-Body Clearing and Imaging. *Nat. Protoc.* **2015**, *10*, 1709–1727.
- (50) Tainaka, K.; Kubota, S. I.; Suyama, T. Q.; Susaki, E. A.; Perrin, D.; Ukai-Tadenuma, M.; Ukai, H.; Ueda, H. R. Whole-Body Imaging with Single-Cell Resolution by Tissue Decolorization. *Cell* **2014**, *159*, 911–924.
- (51) Sindhvani, S.; Syed, A. M.; Wilhelm, S.; Chan, W. C. Exploring Passive Clearing for 3d Optical Imaging of Nanoparticles in Intact Tissues. *Bioconjugate Chem.* **2017**, *28*, 253–259.
- (52) Murray, E.; Cho, J. H.; Goodwin, D.; Ku, T.; Swaney, J.; Kim, S. Y.; Choi, H.; Park, Y. G.; Park, J. Y.; Hubbert, A.; Mccue, M.; Vassallo, S.; Bakh, N.; Frosch, M. P.; Wedeen, V. J.; Seung, H. S.; Chung, K. Simple, Scalable Proteomic Imaging for High-Dimensional Profiling of Intact Systems. *Cell* **2015**, *163*, 1500–1514.
- (53) Hsia, C. C.; Hyde, D. M.; Ochs, M.; Weibel, E. R. An Official Research Policy Statement of the American Thoracic Society/European Respiratory Society: Standards for Quantitative Assessment of Lung Structure. *Am. J. Respir. Crit. Care Med.* **2010**, *181*, 394–418.
- (54) Sanderson, M. J. Exploring Lung Physiology in Health and Disease with Lung Slices. *Pulm. Pharmacol. Ther.* **2011**, *24*, 452–465.
- (55) John, G.; Kohse, K.; Orasche, J.; Reda, A.; Schnelle-Kreis, J.; Zimmermann, R.; Schmid, O.; Eickelberg, O.; Yildirim, A. O. The Composition of Cigarette Smoke Determines Inflammatory Cell Recruitment to the Lung in Copd Mouse Models. *Clin. Sci.* **2014**, *126*, 207–221.
- (56) Barre, S. F.; Haberthur, D.; Cremona, T. P.; Stampanoni, M.; Schittny, J. C. The Total Number of Acini Remains Constant Throughout Postnatal Rat Lung Development. *Am. J. Physiol.-Lung C* **2016**, *311*, L1082–L1089.
- (57) Vasilescu, D. M.; Gao, Z. Y.; Saha, P. K.; Yin, L. L.; Wang, G.; Haefeli-Bleuer, B.; Ochs, M.; Weibel, E. R.; Hoffman, E. A. Assessment of Morphometry of Pulmonary Acini in Mouse Lungs by Non-destructive Imaging Using Multiscale Microcomputed Tomography. *Proc. Natl. Acad. Sci. U. S. A.* **2012**, *109*, 17105–17110.
- (58) Muhlfeld, C.; Hegermann, J.; Wrede, C.; Ochs, M. A Review of Recent Developments and Applications of Morphometry/Stereology in Lung Research. *Am. J. Physiol. Lung Cell Mol. Physiol.* **2015**, *309*, L526–L536.
- (59) Yi, D.; Price, A.; Panoskaltis-Mortari, A.; Naqwi, A.; Wiedmann, T. S. Measurement of the Distribution of Aerosols among Mouse Lobes by Fluorescent Imaging. *Anal. Biochem.* **2010**, *403*, 88–93.
- (60) Yi, D.; Naqwi, A.; Panoskaltis-Mortari, A.; Wiedmann, T. S. Distribution of Aerosols in Mouse Lobes by Fluorescent Imaging. *Int. J. Pharm.* **2012**, *426*, 108–115.
- (61) Hofemeier, P.; Koshiyama, K.; Wada, S.; Sznitman, J. One (Sub-)Acinus for All: Fate of Inhaled Aerosols in Heterogeneous Pulmonary Acinar Structures. *Eur. J. Pharm. Sci.* **2018**, *113*, 53–63.
- (62) Drasler, B.; Vanhecke, D.; Rodriguez-Lorenzo, L.; Petri-Fink, A.; Rothen-Rutishauser, B. Quantifying Nanoparticle Cellular Uptake: Which Method Is Best? *Nanomedicine* **2017**, *12*, 1095–1099.
- (63) Syed, A. M.; Sindhvani, S.; Wilhelm, S.; Kingston, B. R.; Lee, D. S. W.; Gommerman, J. L.; Chan, W. C. W. Three-Dimensional Imaging of Transparent Tissues Via Metal Nanoparticle Labeling. *J. Am. Chem. Soc.* **2017**, *139*, 9961–9971.
- (64) Gotz, A. A.; Rozman, J.; Rodel, H. G.; Fuchs, H.; Gailus-Durner, V.; de Angelis, M. H.; Klingenspor, M.; Stoeger, T. Comparison of Particle-Exposure Triggered Pulmonary and Systemic Inflammation in Mice Fed with Three Different Diets. *Part. Fibre Toxicol.* **2011**, *8*, 1.
- (65) Brown, D. G.; Riederer, S. J. Contrast-to-Noise Ratios in Maximum Intensity Projection Images. *Magn. Reson. Med.* **1992**, *23*, 130–137.
- (66) Michel, R. P.; Cruz-Orive, L. M. Application of the Cavalieri Principle and Vertical Sections Method to Lung: Estimation of Volume and Pleural Surface Area. *J. Microsc.* **1988**, *150*, 117–136.



RightsLink®



Home



Help



Email Support



Sign in



Create Account

Three-Dimensional Quantitative Co-Mapping of Pulmonary Morphology and Nanoparticle Distribution with Cellular Resolution in Nondissected Murine Lungs



Author: Lin Yang, Annette Feuchtinger, Winfried Möller, et al

Publication: ACS Nano

Publisher: American Chemical Society

Date: Feb 1, 2019

Copyright © 2019, American Chemical Society

PERMISSION/LICENSE IS GRANTED FOR YOUR ORDER AT NO CHARGE

This type of permission/license, instead of the standard Terms & Conditions, is sent to you because no fee is being charged for your order. Please note the following:

- Permission is granted for your request in both print and electronic formats, and translations.
- If figures and/or tables were requested, they may be adapted or used in part.
- Please print this page for your records and send a copy of it to your publisher/graduate school.
- Appropriate credit for the requested material should be given as follows: "Reprinted (adapted) with permission from (COMPLETE REFERENCE CITATION). Copyright (YEAR) American Chemical Society." Insert appropriate information in place of the capitalized words.
- One-time permission is granted only for the use specified in your request. No additional uses are granted (such as derivative works or other editions). For any other uses, please submit a new request.

[BACK](#)[CLOSE WINDOW](#)

4.2 Summary of the work PRP2

Multimodal Precision Imaging of Pulmonary Nanoparticle Delivery in Mice: Dynamics of Application, Spatial Distribution, and Dosimetry

A quantitative *in vivo/ex vivo* preclinical imaging platform with high temporal (~ 1 Hz) and 3D spatial resolution (down to cellular resolution) is developed and validated for pulmonary delivery of various NPs by specifically prepared mouse lungs. The platform provides comprehensive and unprecedented insight into the dynamic process of NP delivery to animal models (here mice).

Main accomplishments:

- The potential of this platform was demonstrated by applying different types of NPs (polystyrene, melamine, iron oxide, gold, quantum dots) at different doses into different regions of the lung utilizing the three most widely used modes of preclinical pulmonary NP delivery (intratracheal instillation, nasal aspiration, ventilator-assisted aerosol inhalation).
- Our study reveals the underlying mechanisms of pulmonary delivery which led to a more in-depth and quantitative understanding of the reasons for the observed *ex vivo* NP deposition profile for each of these application modes.
- This study also provides the first detailed performance characteristics of ventilator-assisted aerosol inhalation for improved pulmonary NP delivery in terms of dose rate, dose-controlled and efficiency.
- While this study focused on pulmonary NP delivery, it is also applicable to other delivery routes and the fluorescence imaging mode can also be employed for bioactivity studies (by virtue of bioactive probes). As such this imaging platform will enhance the theranostics capabilities for NPs in mice to leverage the design/development of novel-designed NM and studies on toxicity and biokinetics of NPs.

My contributions are about the experimental design and conceive, animal preparation, X-ray imaging support (X-ray imaging was performed by our TUM collaborators as indicated in the publication), all *ex vivo* fluorescence imaging performance, X-ray and fluorescent imaging process and video manipulation, quantitative fluorescent dosimetry analysis, figure preparation, and manuscript writing and revisions.

Multimodal Precision Imaging of Pulmonary Nanoparticle Delivery in Mice: Dynamics of Application, Spatial Distribution, and Dosimetry

Lin Yang, Regine Gradl, Martin Dierolf, Winfried Möller, David Kutschke, Annette Feuchtinger, Lorenz Hehn, Martin Donnelley, Benedikt Günther, Klaus Achterhold, Axel Walch, Tobias Stoeger, Daniel Razansky, Franz Pfeiffer, Kaye S. Morgan, and Otmar Schmid*

Targeted delivery of nanomedicine/nanoparticles (NM/NPs) to the site of disease (e.g., the tumor or lung injury) is of vital importance for improved therapeutic efficacy. Multimodal imaging platforms provide powerful tools for monitoring delivery and tissue distribution of drugs and NM/NPs. This study introduces a preclinical imaging platform combining X-ray (two modes) and fluorescence imaging (three modes) techniques for time-resolved in vivo and spatially resolved ex vivo visualization of mouse lungs during pulmonary NP delivery. Liquid mixtures of iodine (contrast agent for X-ray) and/or (nano)particles (X-ray absorbing and/or fluorescent) are delivered to different regions of the lung via intratracheal instillation, nasal aspiration, and ventilator-assisted aerosol inhalation. It is demonstrated that in vivo propagation-based phase-contrast X-ray imaging elucidates the dynamic process of pulmonary NP delivery, while ex vivo fluorescence imaging (e.g., tissue-cleared light sheet fluorescence microscopy) reveals the quantitative 3D drug/particle distribution throughout the entire lung with cellular resolution. The novel and complementary information from this imaging platform unveils the dynamics and mechanisms of pulmonary NM/NP delivery and deposition for each of the delivery routes, which provides guidance on optimizing pulmonary delivery techniques and novel-designed NM for targeting and efficacy.

1. Introduction

Lung diseases are among the leading causes of deaths worldwide. According to the World Health Organization^[1] the chronic obstructive pulmonary disease (COPD) and lung cancer have even been rising from the fourth and ninth in 2000 to the third and sixth of most deadly disease in 2016, respectively. For treatment of lung diseases, direct application of the drug to the lung via aerosol inhalation is widely used due to its high therapeutic index, i.e., high efficacy at the site of disease and low side effects in secondary organs. Currently, inhalation therapy is a cornerstone for the treatment of pulmonary infections, asthma, COPD, and cystic fibrosis, but also treatment of lung cancer or even nonpulmonary disease such as diabetes is within reach.^[2,3] Also nanotechnology enabled drugs (nanomedicines (NMs)) offer new diagnostic and therapeutic options for cancer and other diseases leveraging their unique features for controlled release, reduced drug toxicity, prolonged

L. Yang, W. Möller, D. Kutschke, Dr. T. Stoeger, Dr. O. Schmid
Comprehensive Pneumology Center (CPC-M)
Member of the German Center for Lung Research (DZL)
Munich 81377, Germany
E-mail: otmar.schmid@helmholtz-muenchen.de

L. Yang, W. Möller, D. Kutschke, Dr. T. Stoeger, Dr. O. Schmid
Institute of Lung Biology and Disease
Helmholtz Zentrum München-German Research Center
for Environmental Health
Neuherberg 85764, Germany

 The ORCID identification number(s) for the author(s) of this article can be found under <https://doi.org/10.1002/sml.201904112>.

© 2019 The Authors. Published by WILEY-VCH Verlag GmbH & Co. KGaA, Weinheim. This is an open access article under the terms of the Creative Commons Attribution License, which permits use, distribution and reproduction in any medium, provided the original work is properly cited.

DOI: 10.1002/sml.201904112

L. Yang, Prof. D. Razansky
Faculty of Medicine
Technical University of Munich
Munich 80333, Germany

R. Gradl, Dr. M. Dierolf, Dr. L. Hehn, B. Günther, Dr. K. Achterhold,
Prof. F. Pfeiffer, Dr. K. S. Morgan
Chair of Biomedical Physics
Department of Physics
Technical University of Munich
Garching 85748, Germany

R. Gradl, Dr. M. Dierolf, B. Günther, Dr. K. Achterhold, Prof. F. Pfeiffer
Munich School of BioEngineering
Technical University of Munich
Garching 85748, Germany

R. Gradl, Prof. F. Pfeiffer, Dr. K. S. Morgan
Institute for Advanced Study
Technical University of Munich
Garching 85748, Germany

residence, and/or targeted delivery.^[4–6] Consequently, numerous NM formulations are already in clinical use or are currently undergoing clinical trials.^[7,8] In spite of this success a recent study reported that only about 0.7% of the applied dose of intravenously administered nanoparticles (NPs) accumulates at the tumor sites in animal models,^[9] suggesting that targeting delivery of NM is still a major subject of both preclinical and clinical studies.

To better understand and optimize drug/NM delivery to the sites of disease within the lung, it is of central importance to quantitatively monitor the dynamic process of pulmonary drug delivery in the context of deposited dose, initial biodistribution, site-specific localization, biokinetics, and therapeutic efficacy (bioactivity) of NM. Noninvasive imaging techniques including magnetic resonance imaging (MRI), single photon emission computed tomography (SPECT), positron emission tomography (PET), photoacoustic (PA) imaging, ultrasound (US), X-ray-based imaging modalities (phase-contrast X-ray imaging (PCXI) and computed tomography (CT)), and optical imaging (e.g., in vivo imaging system (IVIS)) each provide different advantages in imaging drug/NM distribution, release, and efficacy.^[10,11] MRI provides both morphological and functional information (e.g., target site of NM) in the human lung but is limited by poor spatial resolution (≈ 1 mm), slow image acquisition, and low sensitivity in the lungs of small animals.^[12,13] Nuclear medical imaging including PET and SPECT offers high sensitivity, high imaging depth, and sufficient dosimetric accuracy for quantitative biodistribution and biokinetics studies in the lung. Since those techniques often need a radiolabeled probe and suffer from poor spatial resolution and lack of anatomical information,

hybrid imaging techniques have been proposed to overcome the latter limitations (e.g., joint use of SPECT-CT).^[10] Taking advantage of the combined spectral selectivity of molecular excitation by laser light and high resolution of ultrasound detection,^[14] PA imaging is an emerging nondestructive hybrid technique (optics and acoustics) that allows deeper tissue visualization of fluorescent agents compared to optical imaging. Similar to US, PA can provide anatomical and dynamic imaging, but it is of limited use for the lung due to restricted ultrasound propagation.^[15] Consequently, the penetration depth of light, sensitivity, and quantification ability offered by PA imaging are not sufficient for determination of NM biodistribution and pharmacodynamics in the lungs. X-ray-based approaches (PCXI and CT) have been recently applied to monitor the pulmonary fluid delivery dynamics and deposition^[16–18] and lung pathophysiological state^[19] with high temporal and spatial resolution. The major challenges posed by X-ray modalities are that they are incapable of assessing NM bioactivity and for visualizing NM at cellular resolution. Leveraging the wide range of bioactive optical probes noninvasive optical imaging could resolve the bioactivity issue, but it suffers from poor spatial resolution and low dosimetric accuracy due to strong tissue scattering and absorption of light. There is no single imaging modality that allows for detection of the dynamics of pulmonary drug delivery, regional distribution profile, accurate dosimetry, and cellular localization of NM in intact organ/tissue of animal models.

Multimodal hybrid imaging techniques such as PET-CT and SPECT-MRI are increasingly used as they provide deeper insight into targeting and distribution profile of NM in terms of detection sensitivity, anatomical information, and spatially resolved dosimetry.^[10,11,20] However, most studies have focused on determining the delivery and therapeutic efficacy of NM to xenograft tumor models in murine models,^[21,22] while there is still a lack of understanding of pulmonary drug delivery. In spite of a large number of novel-designed NMs with enhanced pharmacokinetic and pharmacodynamic properties,^[7] such as non-mucoadhesive particles (particles that do not adhere to mucus) prolonging lung retention for sustained release of drugs in the lung,^[23] monitoring the controlled pulmonary delivery of NM in real-time with subsequent analysis of regional spatial distribution, accurate dosimetry, and cellular localization of NM in the lung is still a major unmet need.

This study therefore aims to decipher the dynamics of pulmonary delivery of NPs as well as their regional distribution, dosimetry, and cellular localization by multimodal imaging leveraging X-ray and fluorescence-based imaging techniques. Lung tissue usually produces low contrast in conventional X-ray images, but the visibility of the lungs can be enhanced using phase-contrast techniques that exploit the phase shift introduced by a sample. For weakly absorbing materials such as soft tissue and air, the difference in the phase shift is significant, which leads to contrast enhancement. Propagation-based phase-contrast X-ray imaging (PB-PCXI) was chosen here since this technique requires only a single exposure (compared to, e.g., grating-based phase-contrast imaging), so it is ideal for imaging dynamic processes.^[24] Furthermore, it is a simple technique, because the only change with respect to conventional absorption imaging is an increased sample-to-detector distance and increased source coherence. This coherence requirement

Dr. A. Feuchtinger, Prof. A. Walch
Research Unit Analytical Pathology
Helmholtz Zentrum München
Neuherberg 85764, Germany

Dr. L. Hehn, Prof. F. Pfeiffer
Department of Diagnostic and Interventional Radiology
Klinikum rechts der Isar
Technical University of Munich
München 81675, Germany

Dr. M. Donnelley
Robinson Research Institute and Adelaide Medical School
University of Adelaide
Adelaide 5000, Australia

Dr. M. Donnelley
Respiratory and Sleep Medicine
Women's and Children's Hospital
North Adelaide, SA 5006, Australia

Prof. D. Razansky
Institute for Biological and Medical Imaging (IBMI)
Helmholtz Zentrum München
Neuherberg 85764, Germany

Prof. D. Razansky
Faculty of Medicine and Institute of Pharmacology and Toxicology
University of Zurich
Zurich CH-8057, Switzerland

Prof. D. Razansky
Institute for Biomedical Engineering and Department of Information
Technology and Electrical Engineering
ETH Zurich
Zurich 8093, Switzerland

Dr. K. S. Morgan
School of Physics and Astronomy
Monash University
Clayton, Victoria 3800, Australia

Table 1. Main characteristics and hence complementarity of the propagation-based phase contrast X-ray imaging (PB-PCXI), computed tomography (CT), whole lung fluorescence imaging (WLF), lung slice fluorescence imaging (LSFI), and light sheet fluorescence microscopy (LSFM) at a glance. Strengths are graded low (+) to high (+++).

Imaging method	In vivo/ex vivo	Dimension	Resolution	Fidelity	Anatomical information	Dosimetry	Technical complexity	Contrast agents
PB-PCXI	In vivo	2D + time	+	+++	+	++	+++	Iodine ^{M1} , iron oxide particles ^{M2} , gold NPs, QDs
CT	Ex vivo	3D	++	+++	++	+	++	
WLF	Ex vivo	<2D ^{a)}	+	++	+	++	+	SkyBlue NPs ^{M1} , melamine NPs ^{M1,2} , quantum dots
LSFI	Ex vivo	2D/3D	+	++	++	+++	++	
LSFM	Ex vivo	2D/3D	+++	++	+++	+++	++	

M1: mixture 1 (iodine + SkyBlue NPs/melamine NPs); M2: mixture 2 (iron oxide + melamine NPs). ^{a)}Penetration depth is ≈1 mm (depending on wavelength)—only fraction of murine lung is imaged.

usually limits the use of PB-PCXI to synchrotron facilities.^[25] In this study the Munich Compact Light Source (MuCLS) was used to produce a sufficiently coherent X-ray beam to obtain edge-enhanced images via PB-PCXI. The acquired images include attenuation and phase information, with the attenuation effects rendering the bones and highly absorbing contrast agents visible, and the phase effects rendering the lungs and airways visible.^[26] Here, PB-PCXI was applied to the in vivo real-time monitoring of controlled NP-liquid delivery to different regions of the lung, and subsequent ex vivo CT and fluorescence imaging (here epifluorescence imaging of the whole or dried-sliced lung or tissue-cleared light sheet fluorescence microscopy (LSFM)^[27]) further provided the 3D NP distribution profile throughout the entire lung in both a qualitative and a quantitative manner. The advantages and limitations of each of these techniques are discussed and we demonstrate the potential of this multimodal imaging platform for resolving mechanisms of pulmonary drug delivery and specific features of the NP distribution profile observed for three of the most widely used preclinical modes of pulmonary application, namely, intratracheal instillation, ventilator-assisted aerosol inhalation, and nasal aspiration.

2. Results

The multimodal imaging approaches presented here provide unprecedented concomitant insights into dose, distribution, and mechanism of pulmonary delivery of drugs at high temporal and spatial resolution. In vivo PB-PCXI allows for non-invasive time-resolved monitoring of the dynamic process of drug/nanoparticle delivery, while fluorescence-based ex vivo imaging (IVIS and tissue-cleared LSFM) offers quantitative dosimetry and accurate 3D localization of fluorescent tracers (here NPs) with cellular resolution at one time point. Each of these methods requires the presence of either X-ray contrast agents or fluoroactive substances. Here a variety of NPs and molecular substances are used, including the clinically approved iodine as well as gold NPs, iron oxide particles,

quantum dots (QDs) for X-ray imaging, as well as QDs and polystyrene-SkyBlue and melamine resin NPs for fluorescence-based imaging (Table 1). Except for QDs, which are both X-ray absorbing and fluorescent, all other substances require co-application of two contrast agents. The insoluble particles used here have a diameter between 18 and 900 nm with a relatively narrow size distribution (geometric standard deviation < 1.4; Figure S1, Supporting Information).

A schematic overview of the various imaging modalities is presented in Figure 1. During the pulmonary delivery process time-resolved in vivo PB-PCXI was performed and mice were sacrificed immediately after completion of delivery, lungs were perfused (removal of blood), and then excised. Subsequent ex vivo imaging was performed on the very same lungs using either LSFM on tissue-cleared lungs or X-ray imaging (CT scan) followed by two IVIS fluorescence imaging modalities on dried lungs, namely, whole lung fluorescence imaging (WLF) and lung slice fluorescence imaging (LSFI).

2.1. Time-Resolved In Vivo Monitoring of Controlled Pulmonary NP Delivery with PB-PCXI

For analysis of the mechanisms involved in pulmonary drug delivery (here: iodine-NP) the temporal evolution of drug accumulation in the different regions of the lung was monitored for various forms of drug application in real time by PB-PCXI. The intratracheal instillation and X-ray imaging setup is depicted in Figure 1a. As described by Gradl et al.,^[24] mice were fixed in an upright position, mechanically ventilated, and an iodine-polystyrene NP suspension was instilled slowly into the lungs using a remotely controlled syringe pump. This permits delivery of a known amount of liquid at a controllable and constant rate (here 4.2 $\mu\text{L s}^{-1}$, i.e., 100 μL within 24 s). Triggered by the ventilator, one image per breath was captured during an end-inspiratory breath-hold phase, which minimizes inflation/deflation-induced blurring effects.^[24] This allowed for time-resolved visualization of the pulmonary NP delivery process. Since intratracheal instillation is typically

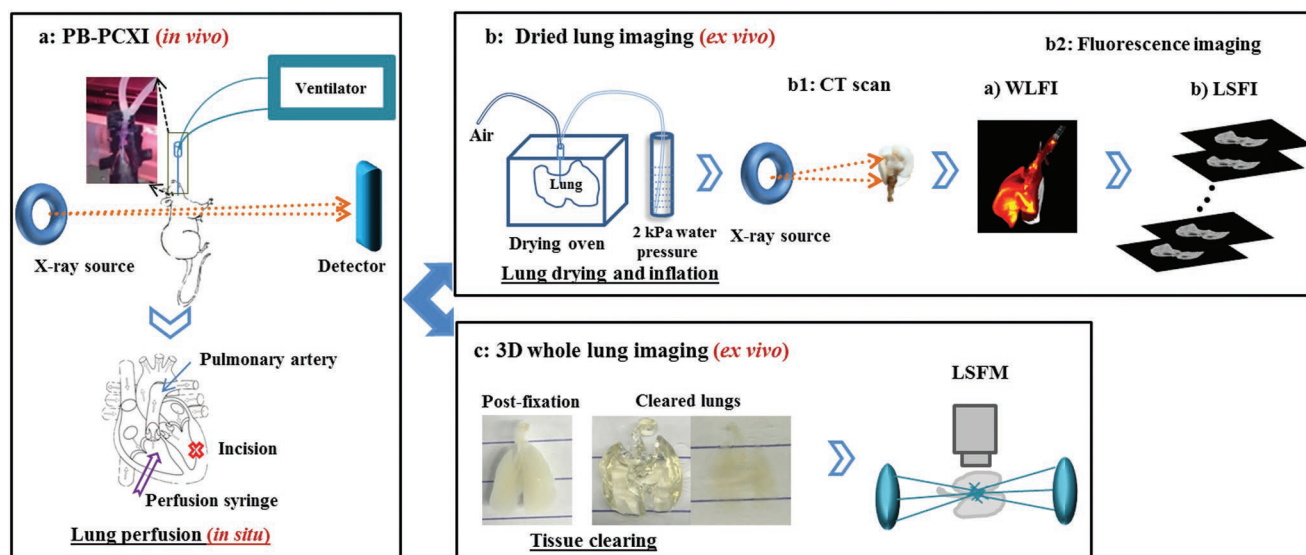


Figure 1. Schematic workflow of multimodal imaging platform from in vivo propagation-based phase contrast X-ray imaging (PB-PCXI) to either ex vivo light sheet fluorescence microscopy (LSFM) or ex vivo lung slice fluorescence imaging (LSFI). Those imaging processes involved in the data acquisition (in vivo PB-PCXI a); ex vivo computed tomography (CT), ex vivo whole lung fluorescence imaging (WLFMI) and LSFI b); and ex vivo LSFMI c)) and sample processing (in situ lung perfusion (a), ex vivo lung drying and inflation (b), and ex vivo lung tissue clearing (c)) were applied in this study.

performed by rapid manual emptying of a syringe (within less than 1 s), we thus refer to the instillation process used here as “slow-instillation.”

Figure 2a shows the X-ray images obtained with this setup. The rib cage and spinal cord of the mouse (dark structures) as well as the lung (bright area within the rib cage) enclosing

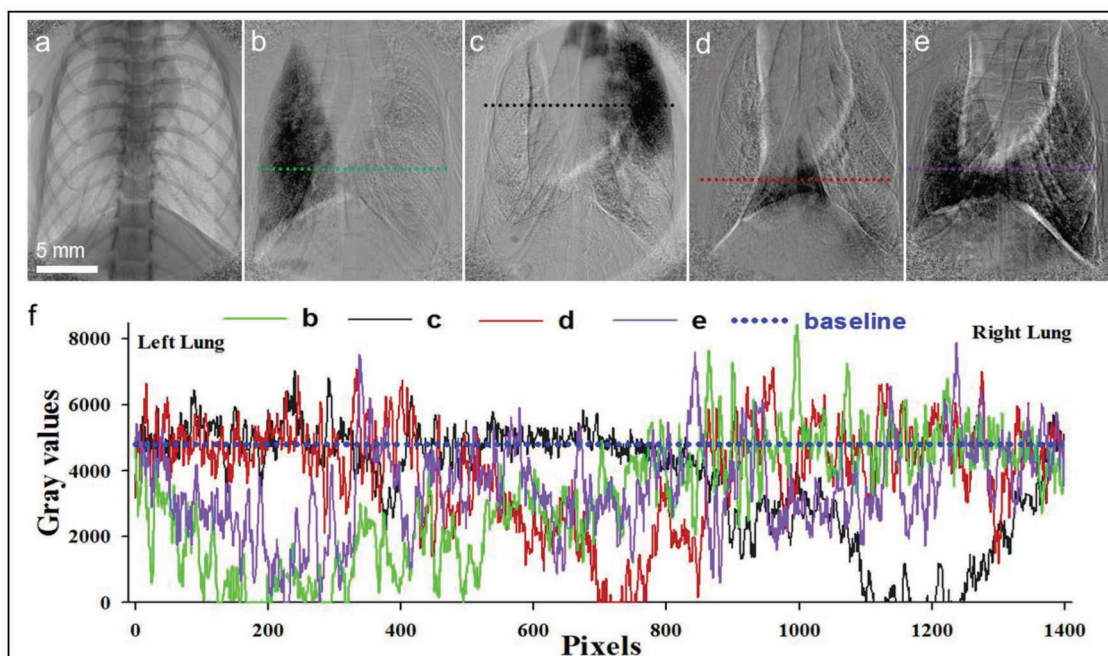


Figure 2. Controlled iodine-nanoparticle liquid delivery to the left/right or whole lung via slow-instillation can be visualized in vivo using PB-PCXI. a) A raw X-ray image directly captured during instillation of 100 μ L iodine-polystyrene NP liquid to the mouse lung. b) Same as panel (a), but a pre-delivery image is subtracted, clearly enhancing the visibility of the iodine-polystyrene NP liquid in the left half of the lung. c–e) Difference images as well, but for different experiments delivering the iodine-polystyrene NP liquid to the upper right lung, lower right lung, and entire lung, respectively, by controlling the position/depth of intubation cannula. f) Pixel-by-pixel intensity profiles along the linear trajectories across the 2D lung images (along the colored dashed lines in panels (b)–(e)) demonstrate that massive decreases in pixel intensity (compared to baseline in blue) result from the substantial deposition of iodine, while the fluctuations in the signal are due to, e.g., imperfect subtraction of the pre-delivery image.

the heart (dark region in the top center of the lung region) are clearly visible. By subtraction of the predelivery image from each image during substance delivery a difference image is obtained, which reduces the “background” signal from the rib cage, spine, and heart (Figure 2b). Consequently, this difference image more clearly shows the pulmonary distribution of the iodine-NP liquid, which in this case was directed to the left half of the lung by placing the intubation cannula beyond the first bronchial bifurcation (separating the left and right half of the lung). Moreover, the subtraction image also highlights the position of the main bronchi and boundaries of the lung, which provides guidance on localization of the delivered iodine-NP solution which is useful for data interpretation. Figure 2c–e displays equivalent images for different delivery experiments via intratracheal instillation directed to the right upper, right lower, and whole lung, respectively, via proper positioning of the inserted cannula. Moreover, intensity profiles along (linear) trajectories across the 2D lung images depicted in Figure 2e illustrate the variability of the gray-scale signal for the different regions of these lungs, where lower signals correspond to regions of higher iodine dose (high X-ray absorption), indicating the major locations of iodine-NP liquid (Figure 2f). This pixel-by-pixel analysis (pixel size: 10.4 μm) reveals massive loss of X-ray intensity in regions of substantial iodine deposition, while the fluctuations in signal originate from artifacts due to, e.g., imperfect background subtraction partially due to unavoidable slight position changes of the breathing mouse during the course of the substance delivery process.

Time-resolved *in vivo* visualization of the dynamic process of liquid delivery via intratracheal instillation to the lung (see Videos S1 and S2 in the Supporting Information for left and whole lung delivery) reveals that the main delivery mechanism is not only gradual spreading of the liquid from the point of entry (trachea/primary bronchus) to the more distal parts of the lung, but also by recurring liquid accumulation in and blocking of one of the airways followed by rupturing of the liquid blockage during breathing activity. This results in secondary spray/aerosol formation, which provides an efficient mechanism for bulk liquid reaching the distal parts of the lung.

2.2. Ex Vivo Multimodal Imaging of NP Distribution in the Lungs

After *in vivo* PB-PCXI each lung underwent *ex vivo* imaging using either LSFM or CT scanning followed by WLFI and LSF (Figure 1b,c). Both imaging modes are mutually exclusive, since the former requires wet fixation and optical tissue clearing, while the latter involves drying of the lung. Since the last *in vivo* PB-PCXI image corresponds to the *ex vivo* images, the agreement between *in vivo* PB-PCXI and *ex vivo* imaging modalities can be assessed. **Figure 3** presents an example of this data set after slow-instillation of 100 μL iodine-NP solution. The pseudocolored PB-PCXI difference image that is overlaid with a directly obtained image clearly indicates two main regions of iodine-NP deposition, one in the upper right lung and the other around the diaphragm (Figure 3a and Video S3, Supporting Information). 3D reconstructed *ex vivo* lung from a CT scan of the same subject depicts a qualitatively consistent

distribution profile with preferential right superior lobe targeting and some near-diaphragm postcaval lobe deposition (Figure 3b and Video S4, Supporting Information). This distribution pattern is also found by WLFI (Figure 3c and Figure S2, Supporting Information) and LSF (Figure 3d).

Ex vivo fluorescence LSF allows for quantitative analysis of the regional targeting of fluorescence substances. Lungs from nine independent slow-instillation experiments were stratified for preferentially left and right as well as uniform (global) NP deposition in the lung. The ratios of the fluorescence intensities from the right and left lung, which are normalized to their respective right and left lung volume to account for the effect of volume-dependent lung ventilation,^[27,28] reveal that for global delivery the ratio is equal to unity and a 3.7-fold preferential targeting of the right (3.7) and left ($3.7 = 1/0.27$) half of the lung was accomplished, respectively (Figure 3e). Finally, the delivered dose was determined from quantitative fluorescence analysis using dose-intensity conversion curves based on two reference lungs containing known amounts of polystyrene-SkyBlue NPs (using regular intratracheal instillation) and three nontreated lungs for tissue-autofluorescence correction.^[27,29] In this context it is important to note that the presence of iodine did not affect the fluorescence signal from SkyBlue NPs (Figure S3, Supporting Information). In the present experiments, 50 and 100 μL were applied via intratracheal slow-instillation at a constant delivery rate of ($4.2 \mu\text{L s}^{-1}$) and $72.98 \pm 36.21\%$ and $79.9 \pm 24.1\%$ of the nominal dose was delivered to the lung, respectively (Figure 3f), where for one of the 50 μL lungs almost nothing (<7%) reached the lung probably due to accidental withdrawal of the intubation cannula during the delivery procedure. Hence, no significant difference in deposited fraction of applied dose/volume was found for different volumes via slow-instillation (between 50 and 100 μL). It also reveals that slow-instillation of 50 μL liquid yields the same fractional deposition as reported for regular instillation $77.2 \pm 14.2\%$ (50 μL in <1 s; no data for 100 μL are available).^[29] Quantitative analysis with any of the other imaging modalities is difficult due to substantial tissue attenuation for whole lung fluorescence imaging and challenges in separating X-ray contrast seen from the treatment and the X-ray contrast seen from the living anatomy.

In summary, this analysis shows that *in vivo* X-ray and *ex vivo* X-ray and fluorescence imaging approaches show qualitatively consistent pulmonary deposition patterns for intratracheal slow-instillation, which indicates co-localization of X-ray and fluorescence-active agents. Moreover, LSF allows for quantitative dosimetry analysis of fluorescent NPs. The data presented here also show that positioning of the intubation cannula beyond the first bifurcation of the bronchial tree allows for regional targeting of liquid substances into the left or right half of the lung, but deliberate selection of either the right or left half is difficult. Finally, regular and slow-instillation provide similar substance delivery efficiency ($\approx 75\%$) with somewhat better dose reproducibility for regular instillation.

2.3. Visualization of Small-Volume Slow-Instillation by Multimodal Imaging

Visualization of extremely small amounts of bulk liquid (4 μL) delivery throughout the entire murine lung with $\approx 1000 \mu\text{L}$ total

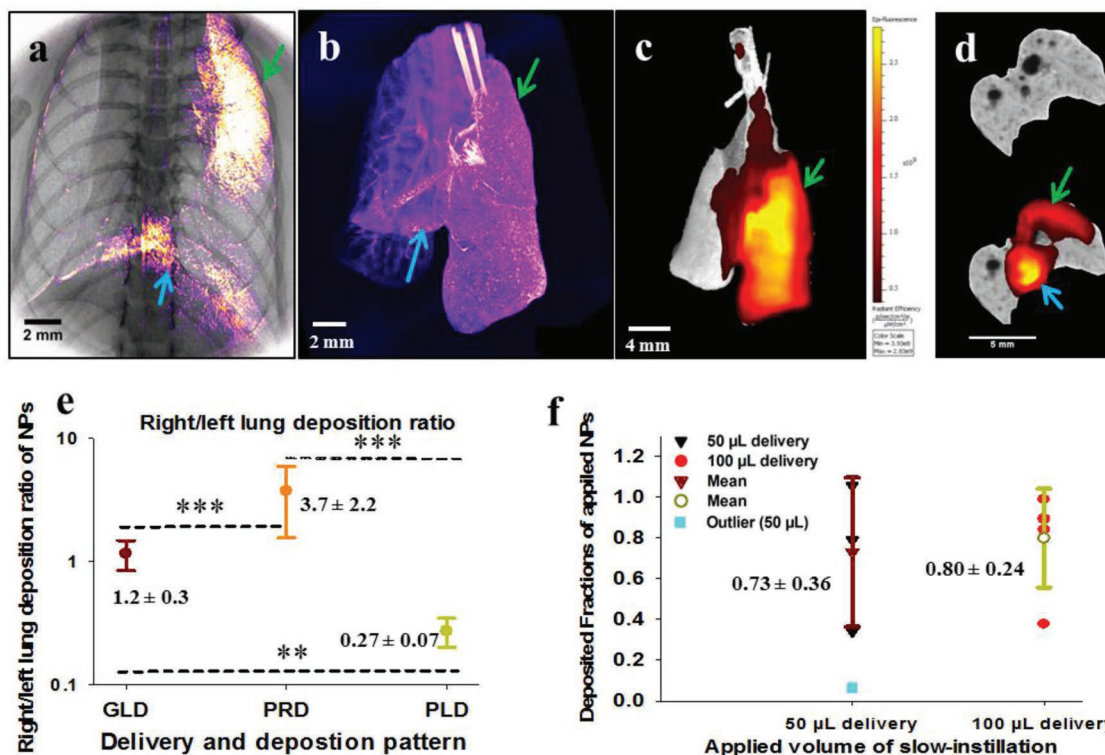


Figure 3. In vivo and ex vivo imaging modalities show consistent end-delivery distribution of an intratracheally slow-instilled iodine-nanoparticle suspension in the lungs (posterior view). a) A pseudocolored difference image (analogous to Figure 2b) overlaid with a directly obtained X-ray image (analogous to Figure 2a) allows for co-mapping of lung morphology and iodine-polystyrene NP deposition, indicating preferential delivery to the superior and postcaval lobe of the right lung (green and blue arrows, respectively). b) Matching bi-lobe delivery was also observed from an ex vivo CT scan. Ex vivo fluorescence images obtained from c) WLFI and d) LSF further indicate the success of right lung delivery. Due to tissue-induced light attenuation, the fluorescence signal from the near diaphragm postcaval lobe is not visible in posterior view (c) but clearly evident in anterior view (Figure S2c, Supporting Information). e) Right/left deposition ratios of NPs normalized to the respective right/left lung volume ratio were measured quantitatively with WLFI, displaying the success of preferential right or left delivery (PRD or PLD) and global lung delivery (GLD). f) Quantitative determination of the dose/volume of liquid delivered to the whole lung using the LSF data for 50 or 100 µL of applied liquid.

lung volume (600 cm² epithelial surface area) via intratracheal instillation is notoriously difficult. It has been reported that addition of lung surfactant could facilitate pulmonary delivery both in terms of speed of dispersion and uniformity of distribution as surfactant is known to reduce surface tension of the applied bulk liquid.^[30] In this case, the mouse was intubated for syringe-assisted slow-instillation, but breathing spontaneously and in vivo X-ray image acquisition (100 ms per breath) near the end of inhalation was triggered by monitoring the motion of the chest with an optical displacement sensor.^[31] In vivo PB-PCXI revealed that delivery of 4 µL of iodine-polystyrene NP liquid resulted in highly localized, small puddles of liquid into either the right or left lung, but not to both sides (Figure 4a and Video S5, Supporting Information). Only the proximal bronchial region was reached and addition of surfactant did not affect delivery speed or localization of the liquid as shown in Figure 4d and Video S6 (Supporting Information). The small amounts of iodine delivered to the lungs were below the detection limit of ex vivo CT as seen from Figure 4b,e. On the other hand, ex vivo WLFI was able to detect the fluorescence signal in the left half of the lung (red in Figure 4c,f) confirming the distribution observed with in vivo PB-PCXI. Quantitative dosimetry based on LSF (Figure 4g) revealed no statistically

significant effect of lung surfactant on the delivered dose fraction of 4 µL iodine-NP liquid (with and without surfactant: 0.71 ± 0.19 and 0.53 ± 0.28 , respectively). In fact this delivery fraction is also consistent with the corresponding values for 50 and 100 µL of liquid instillation (Figure 3f).

2.4. Real-Time Monitoring of Particle Delivery by PB-PCXI: Gold, Iron Oxide, and QDs Delivery

In the experiments reported above iodine was added to the NP suspension, since the polystyrene NPs cannot be detected by X-ray analysis. Substances with a high atomic number or density, such as iodine, lanthanide, gold, or bismuth-based materials, are preferable to be used as X-ray contrast agents because of their high absorption cross section.^[32] Recently, utilization of NP-based X-ray contrast agents has been intensively discussed for diagnostic and molecular imaging, as NPs provide the potential of high loading of contrast agents and the possibilities of surface modification enhancing cell/organ-specific targeting. Traditionally, gold NPs have been used as X-ray contrast agents for, e.g., imaging tumor targeting of NPs via proper surface functionalization after intravenous injection in vivo.^[33]

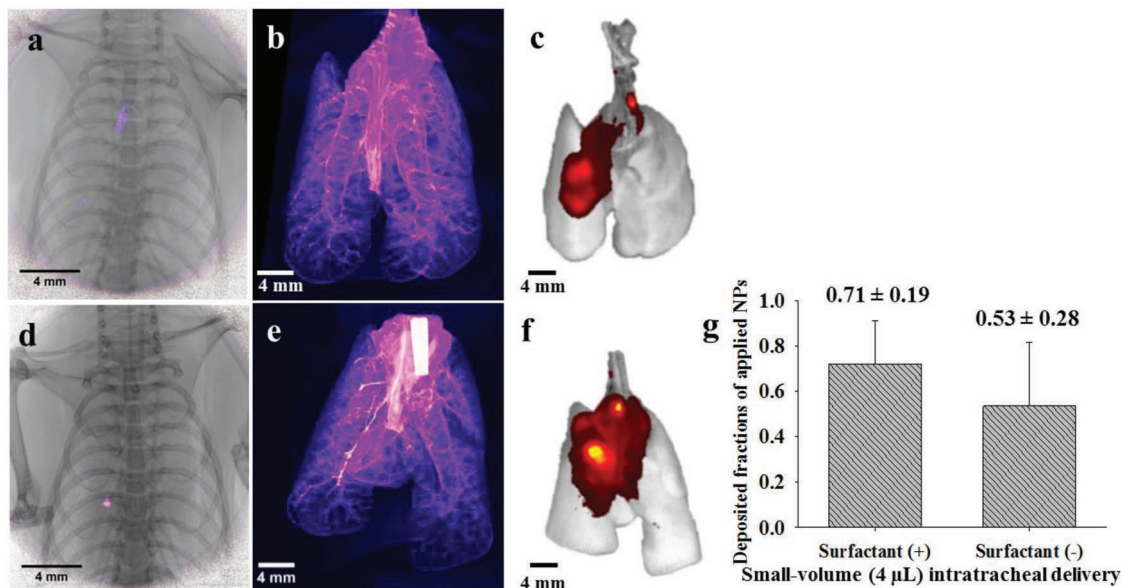


Figure 4. Determination of small-volume (4 μL) intratracheal slow-instillation of iodine-NP suspension a–c) in the absence and d–f) presence of alveolar surfactant by multimodal imaging. Representative 2D images with *in vivo* PB-PCXI show the highly localized delivery of 4 μL iodine-polystyrene NP liquid without (a) or with (d) surfactant. The X-ray signal is below the detection limit of 3D reconstructed images from *ex vivo* CT ((b) and (e)), while 2D images obtained from *ex vivo* WFLI exhibit the proximal bronchial distribution of iodine-polystyrene NP liquid ((c) and (f)), albeit more diffuse than in (a) and (d) due to tissue-induced light scattering. The presence of surfactant had no effect on the speed of liquid dispersion and uniformity of distribution. g) The deposited fractions of 4 μL slow-instillation without or with surfactant based on LSF1 data.

However, gold NPs have rarely been used as X-ray contrast agent for pulmonary delivery. This study visualizes the dynamic process of pulmonary delivery of three types of particles (two out of the three are NPs) in real time using *in vivo* PB-PCXI.

Figure S4 (Supporting Information) shows five consecutive PB-PCXI frames revealing the temporal evolution of the NP delivery process during nasal aspiration of 40 μL gold NP suspension (delivered to one nostril of the mouse with a rate of 0.16 $\mu\text{L s}^{-1}$). The pseudocolored difference images highlight the location of the NP suspension. The gold NP suspension initially forms an increasing drop at the tip of the syringe and—once large and close enough to the nostril—the droplet is suddenly inhaled (aspirated) and deposited in the left half of the nasal airways and eventually draining down passed the glottis into the trachea into the left primary bronchus as observed in Video S7 (Supporting Information) and even into the deep lung. The sequence of images in Figure 5a,b displays the temporal evolution of NP delivery into the deep lung via intratracheal slow-instillation of 100 μL of a mixture of iron oxide and (fluorescent) melamine particles and pure QDs, respectively. Clearly, the iron oxide particles (2.5 mg mL^{-1}) were delivered quite uniformly throughout the targeted left half of the lung (Figure 5a), albeit the image contrast is not as good as for iodine (92.5 mg mL^{-1}), which is at least in part due to the lower mass concentration/dose of iron oxide particles. The QDs were delivered to the whole lung (Figure 5b) and the mechanism of delivery is a relatively slow and continuous transport (several seconds) of a film of particle liquid (position indicated by arrow) from the trachea to the deeper regions of the lung. Also, similar to iron oxide, the lower mass dose of QDs (0.4 $\times 10^{-6}$ M) results in lower contrast compared with

iodine (92.5 mg mL^{-1}). Relatively uniform distribution of QDs throughout the lung into the distal airways and alveoli makes it even difficult to visualize. The dynamic processes of instillation delivery for iron oxide particles and QDs are shown in Videos S8 and S9 (Supporting Information), respectively. Of note, QDs are particularly interesting, as they can serve as contrast agent for both X-ray and fluorescence imaging.

2.5. Cellular Localization of NPs Revealed by *Ex Vivo* Tissue-Cleared LSF1 in Nondissected Lungs

None of the imaging modalities above offers the possibility for 3D visualization of NP localization with cellular resolution throughout the entire mouse lung. While CT scan and LSF1 offer 3D imaging capabilities, they do not allow for NP localization within individual cells. We recently demonstrated that *ex vivo* LSF1 allows for quantitative co-mapping of lung architecture and NP deposition with single-cell resolution in nondissected but optically cleared lungs.^[27] Here we apply this method to study the pulmonary distribution of 100 μL of an NP suspension after intratracheal slow-instillation. Figure 6 shows the general agreement of the whole lung distribution as observed by PB-PCXI and LSF1 for iodine-melamine NPs (Figure 6a,b), iron oxide-melamine NPs (Figure 6d,e), and QDs (Figure 6g,h). At cellular resolution (pixel size <1 μm) melamine NPs were found mainly deposited in the bronchi as well as the bronchioles and proximal part of the alveolar duct (Figure 6c), the so-called proximal acinar region. Similar results were found for iron oxide and (fluorescent) melamine NPs delivery however with a more preferential delivery to the left half of the lung

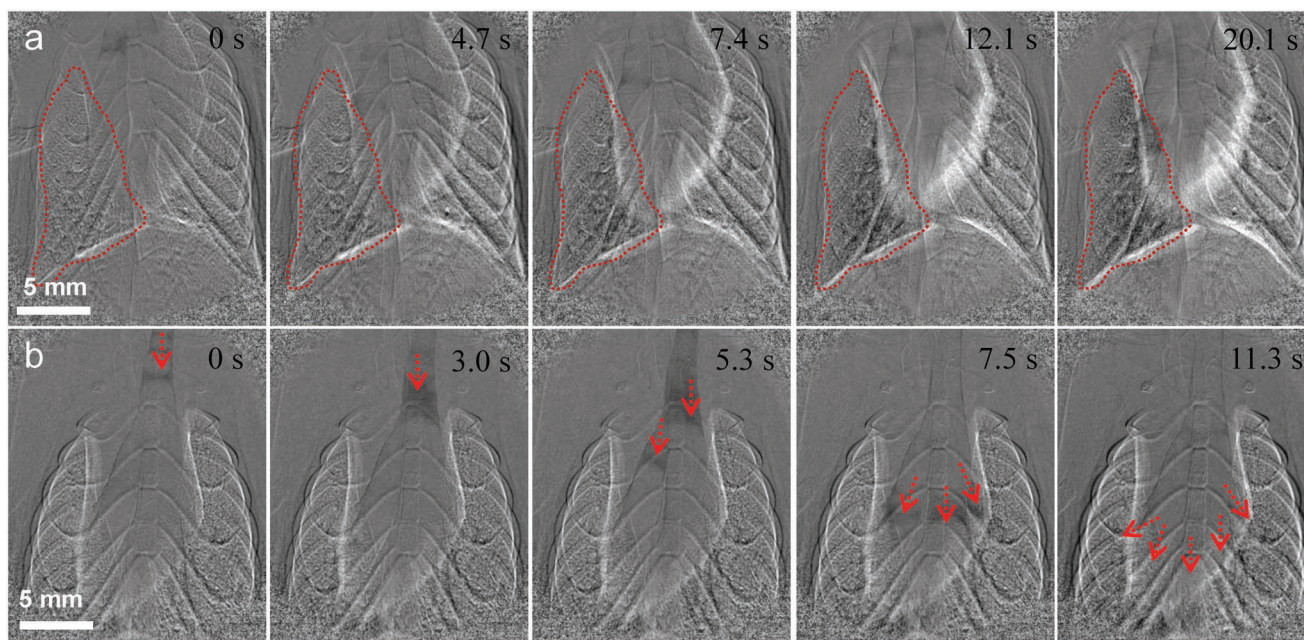


Figure 5. Real-time monitoring of pulmonary delivery of pure particles by in vivo PB-PCXI. a,b) Difference image sequences of the intratracheal slow-instillation of 100 μL iron oxide (mixed with fluorescent melamine NPs) and pure QDs at 24 s ($4.2 \mu\text{L s}^{-1}$) to the mouse lung, respectively. The iron oxide particles were delivered quite uniformly throughout the left lung (results from placing the intubation cannula beyond the first bifurcation) (a) and QDs were distributed to the whole lung (b). Compared to iodine the reduced image contrast is in part due to the lower delivered particle dose. Arrows indicate the formation of liquid accumulations that do not completely block the airways (no secondary aerosol formation) but gradually slide down the airway tree. The increased background noise (e.g., rib cage morphology) is due to unavoidable mouse movements and the lower contrast of pure NPs as compared to iodine. The time axis indicates real time in seconds after the first image in which time was set to 0 s.

distribution (Figure 6d,e). Also the small amount of melamine NPs delivered to the right lung was preferentially located in the distal small airways (bronchioles) and proximal alveolar region (entrance of alveolar sac) (Figure 6f). Finally, Figure 6g displays the QDs distribution profile in the whole lung imaged by PB-PCXI and the regions of high QD dose are indicated by red arrows. It is evident that in this case QDs were distributed to all five lung lobes but did not transport into the peripheral lung (Figure 6h) reaching only a few localized small alveolar regions (Figure 6i). An animation of the distinct 3D distribution profiles of QDs in whole murine lung measured by LSFM can be seen in Video S10 (Supporting Information).

2.6. Multimodal Imaging for Comprehensive Deciphering of the Characteristics of Aerosol Inhalation

The clinically most relevant route of pulmonary drug delivery is aerosol inhalation. Here an iodine-NP liquid was delivered to the lung via ventilator-assisted inhalation of aerosols. Since individual aerosol droplets are too small for direct imaging ($2\text{--}4 \mu\text{m}$ diameter) and their liquid/contrast delivery rate was extremely small (8.6 nL s^{-1} ; ≈ 490 -fold smaller than slow-instillation), in vivo PB-PCXI is very challenging. In order to visualize the dynamic delivery process of aerosol inhalation, a large volume of NP-iodine liquid was nebulized ($225\text{--}300 \mu\text{L}$) and quantitative fluorescence spectroscopy in tissue homogenates revealed that $3.7 \pm 1.1\%$ and $5.6 \pm 2.3\%$ of the applied volume was deposited in the lung lobes and the trachea, respectively

(Figure 7j).^[34] It is noteworthy that from quantitative spectrofluorometry of the lung slices (LSFI) one obtains a deposited aerosol fraction of $15.6 \pm 2.8\%$ (whole lung) (Figure 7j), which is significantly larger than the $9.3 \pm 2.3\%$ (trachea + lung lobes) measured in lung/trachea homogenates, probably due to the higher light attenuation in sliced lung tissue. Since we consider tissue homogenization as more accurate method of LSF, we report 8.6 and 12.9 nL s^{-1} as pulmonary and tracheal aerosol deposition (delivery) rate, resulting in 5.6 and $8.3 \mu\text{L}$ NP liquid out of applied $150 \mu\text{L}$ volume deposited in the lung and trachea, respectively. Not surprisingly, in vivo PB-PCXI showed no iodine-related signal during aerosol application (Figure 7a) due to the low iodine delivery rate and the extremely uniform distribution of (aerosolized) iodine throughout the lung. On the other hand, gradual accumulation of iodine in the lung over the entire inhalation period (10 min and 48 s) was sufficient for obtaining a clear iodine signal from in vivo PB-PCXI (Figure 7a–d and Video S11, Supporting Information).

Moreover, in vivo PB-PCXI was useful to resolve unexpected, nonaerosol related secondary liquid re-distribution mechanisms, which can occur during ventilator-assisted aerosol inhalation. Unlike instillation, which shows a relatively patchy liquid distribution in the lung (Figure 6b), aerosol inhalation spreads the relatively small lung-deposited dose uniformly throughout the entire lung as can be clearly seen from ex vivo 3D reconstruction of the lung from CT scan (Figure 7e), ex vivo WLF (Figure 7f), and ex vivo tissue-cleared LSF (Figure 7g–i). During the process of ventilator-assisted inhalation localized accumulations of liquid were observed in the upper airways

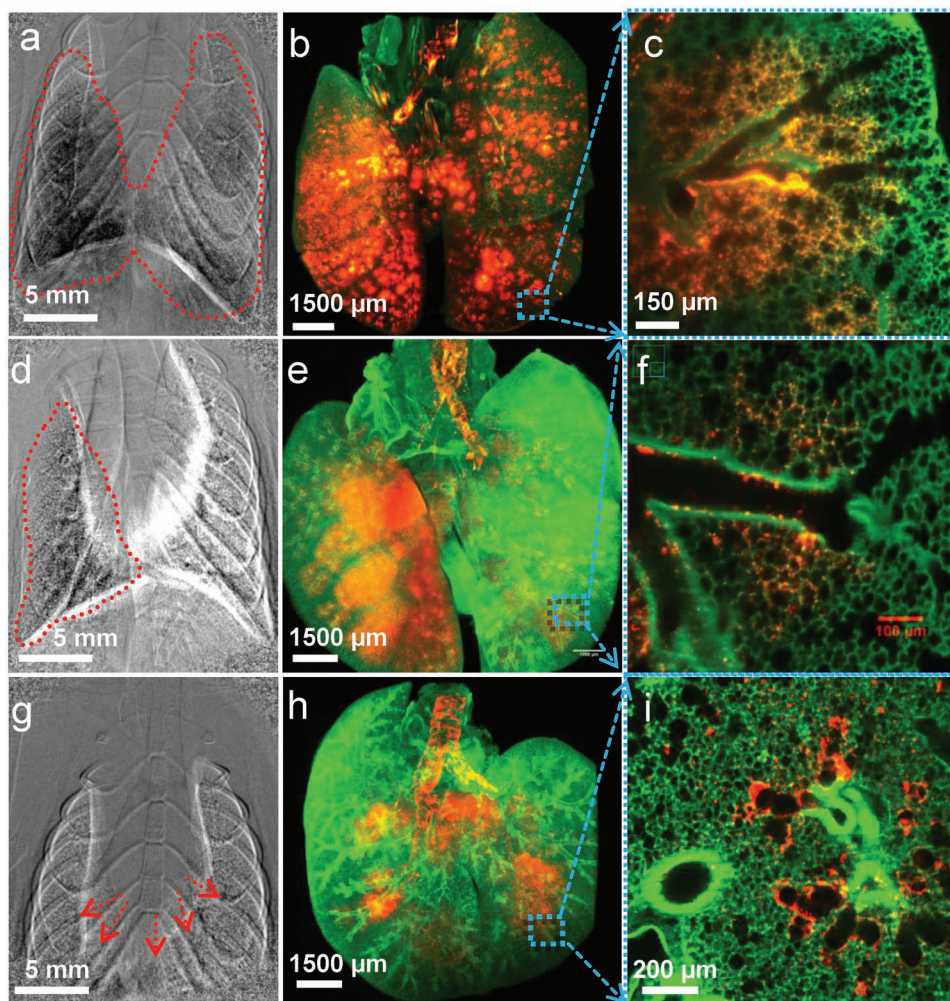


Figure 6. In vivo PB-PCXI and ex vivo tissue-cleared LSFM for cellular-resolution visualization of NP-liquid localization in nondisseminated whole murine lungs after slow-instillation (100 μL of liquid). a) The PB-PCXI difference image shows the pulmonary distribution of an iodine-melamine NP suspension after instillation, which is consistent with the result obtained from b) 3D reconstructed LSFM image. c) A 2D image with cellular resolution further reveals the specific NP localization. Images obtained from d) in vivo PB-PCXI and e) ex vivo LSFM distinctly show preferential left lung distribution of a mixture of iron oxide particles with melamine resin NPs. f) NP deposition in distal small airways (bronchioles) and proximal alveolar regions was revealed by 2D images in single cell resolution. For QD application g–i) a similar set of images shows that QDs were delivered to all five lobes with highest deposition in the distal part of the terminal bronchioles and the entrance of the alveolar duct. Green: tissue autofluorescence; red: melamine NPs (b), (c), (e), and (f)) or QDs ((h) and (i)).

near the trachea (Figure 7b, arrow), which were gradually transported to the lower airways (Figure 7c, arrow) and into the bronchiolar region where they dispersed (Figure 7d, arrows) into even smaller liquid accumulations as evidenced by fluorescence “hot spots” seen in LSFM (Figure 7h, arrows). Not only the presence but also the origin of these occasional accumulations of liquid in the lower bronchial region can be understood from multimodal imaging. Ex vivo whole lung imaging (Figure 7f,g) and quantitative fluorometric dosimetry (Figure 7j) provide evidence for substantial aerosol deposition in the trachea ($\approx 60\%$ of the total deposited aerosol dose is deposited in the trachea). Since the murine trachea is a rather narrow duct, it is conceivable that the trachea-deposited aerosol will eventually block the trachea resulting in spillover of some of the liquid in the trachea into the upper airways and from there into the bronchiolar region as observed by in vivo PB-PCXI (Figure 7b–d) and ex

vivo LSFM (Video 12, Supporting Information). As this spillover typical occurred after 95 s during nebulization, we conclude that at least 1.2 μL ($12.9 \text{ nL s}^{-1} \times 95 \text{ s}$) of liquid has to get accumulated in the trachea for occurrence of the spillover, which corresponds to 22 μL of nebulized liquid ($= 1.2 \mu\text{L}/0.056$).

3. Discussion

Aerosol delivery of drug/NM is the most widely used application route for treatment of lung disease.^[35,36] Targeted delivery of drug/NM on a regional and even cellular scale is of central importance for precision medicine especially for localized lung diseases such as lung cancer, asthma, emphysema, or COPD.^[3,37] Also inhalation of ambient NPs is one of the main health hazards associated with NPs.^[38,39] The region of NM/NP

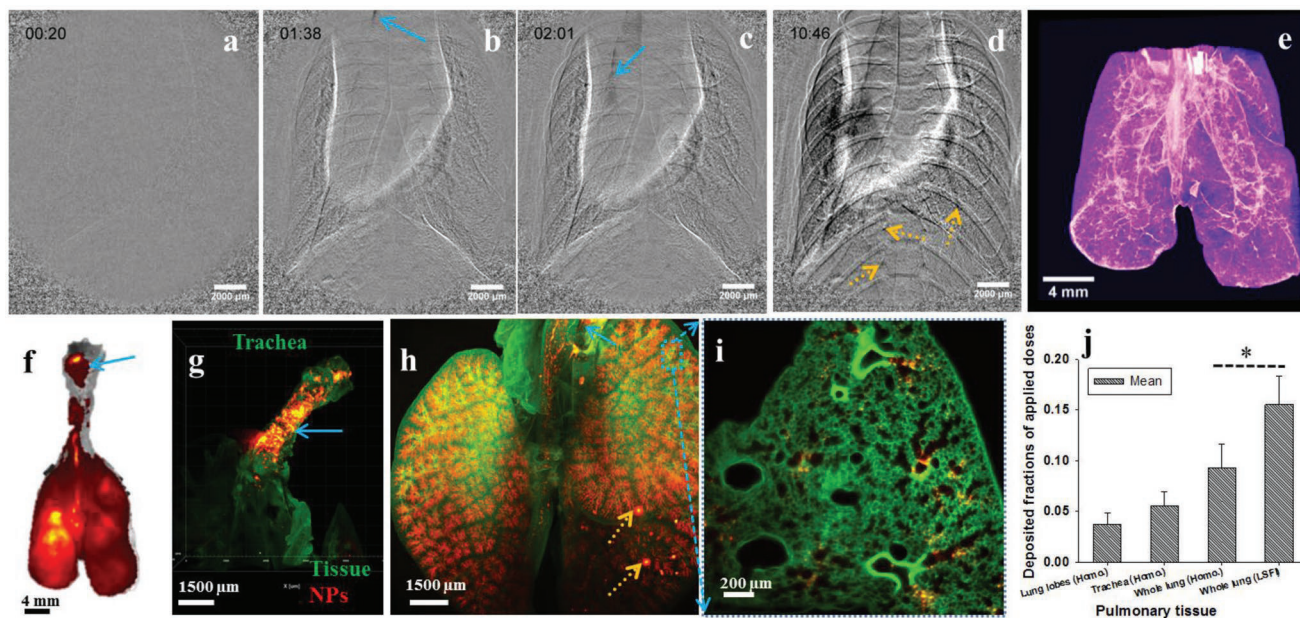


Figure 7. Leveraging multimodal imaging for a comprehensive understanding of the characteristics and delivery mechanism of ventilator-assisted aerosol inhalation. a) Time-resolved visualization of 150 μ L aerosol inhalation (takes 10 min and 48 s) with in vivo PB-PCXI shows no obvious X-ray signals during the entire period of aerosol delivery (iodine-polystyrene NP suspension). However, occasional appearance of localized accumulations of liquid could be observed b) (light blue arrow) in the upper airways, which were then gradually transported to c) (light blue arrow) the lower airways and finally dispersed d) (yellow arrows) in the bronchiolar region. a–d) The time (mm:ss) noted in the left upper corner of the images indicate the time after start of aerosol inhalation. The 3D and 2D images from e) ex vivo CT and f) WLF, respectively, exhibit the whole lung liquid distribution, but only WLF provides a differentiated deposition profile matching end-inhalation PB-PCXI. g–i) The LSF images, which were obtained for a different lung after aerosol inhalation of 40 μ L melamine NP suspension, show high deposition at the end of the intubation cannula in the trachea (g) and very uniform deposition throughout all lung lobes (h) especially in the proximal acinar region (bronchioles and proximal part of alveolar duct) with the exception of a few “hot spots” in the bronchioles (h), yellow arrow, which can be rationalized by the features (yellow arrows) observed by PB-PCXI (d). i) 2D cellular visualization of NP deposition in lung tissue. j) Determination of the deposited fraction of the applied aerosol dose in all lung lobes, trachea, and whole lung (lung lobes + trachea) using quantitative spectrofluorometry in lung homogenates (homo) or on lung slices (LSFI).

deposition can have a significant impact on residence time, release kinetics, and hence bioactivity of the drug or toxicity of NPs.^[40,41] While NM/NP can be quickly (within minutes) removed from the upper airways by mucociliary transport, clearance of NM/NP from the alveolar epithelium mainly relies on uptake by alveolar macrophages (takes a few hours), which may be enough time for direct bioactivity/toxicity of the NM/NP or result in secondary drug release into or from the macrophages.^[2] Consequently, understanding the mechanisms of pulmonary NM/NP delivery and their relevance for tissue-delivered NM/NP dose with cellular resolution is essential for the development of effective NM^[42] or minimizing health hazards of NPs.^[43] Standard histological analysis or single-modality imaging techniques cannot resolve the entire delivery process in all relevant temporal (seconds to days) and spatial scales (whole lung to cellular).^[44] This is also the case for the preclinical efficacy or toxicity testing of NM/NP using animal models.

In this study we combined in vivo X-ray and ex vivo fluorescence imaging modalities to investigate the dynamic process of pulmonary NM delivery and its impact on pulmonary NM distribution with high temporal and spatial resolution in murine lungs. PB-PCXI utilizes differences in X-ray refractive index and associated phase shifts at air–tissue interfaces for enhancing soft tissue contrast (e.g., in the lung) as compared to X-ray absorption.^[26] Building on our previously published in vivo PB-PCXI studies in murine lungs,^[18,24] the present

study demonstrates that combined in vivo PB-PCXI and ex vivo fluorescence imaging can provide complementary information, which enhances the understanding of complex processes such as NM/NP delivery to the lung in a quantitative way on various scales (whole lung to cellular). The strengths and weaknesses of all five imaging modalities used here are summarized with respect to 2D/3D imaging capability, resolution, fidelity (conservation of original anatomical 3D structure), anatomical information, and technical complexity as summarized in Table 1. In general, X-ray imaging is used here for in vivo imaging at high temporal resolution (1 Hz), while ex vivo fluorescence imaging provides insight into spatially resolved dosimetry.

In preclinical lung research, instillation or aspiration of bulk liquids is the most widely used method of pulmonary drug delivery. On the other hand, aerosol inhalation—not bulk liquid application—is the preferred route of drug delivery in clinical settings. In spite of their widespread use detailed information on the dynamic details of the application processes and spatially resolved dosimetry is scarce. All three application routes have been investigated in this study, but a significant focus was on ventilator-assisted aerosol inhalation, since it offers a technologically mature, efficient (\approx 4% of invested dose is delivered to lung) and dose-controlled method for physiologic delivery of liquid substances to the lungs of animal models (here mice) using a commercially available device (flexiVent system,

EMKA/SciReq Inc.). As such it has the potential to at least partially replace intratracheal instillation and nasal aspiration in future preclinical inhalation drug or toxicity testing.

It is evident that intratracheal instillation allows for highly efficient ($76.3 \pm 23.0\%$ of invested dose reaches the lung), dose-controlled delivery of liquids (repeatability: 30.1%) for all tested liquid volumes (4–100 μL) into the deep parts of the lung (bronchioles and even alveoli). It is not intuitively clear how a bulk liquid injected into the trachea via intratracheal instillation can reach the deeper parts of the lung. In vivo PB-PCXI revealed that the instilled bulk liquid is not primarily flowing down the bronchial tree, but is distributed quite uniformly throughout the lung by secondary aerosol formation due to occasional blockage of the airways with liquid and subsequent bursting of this blockage during breathing activity (Videos S1–S3, Supporting Information).^[24] As mentioned above, the slow-instillation process (24 s for 100 μL ; $4.2 \mu\text{L s}^{-1}$), which was used here for the sake of in vivo PB-PCXI imaging, is not identical to the typically used, rapid manual instillation ($<1 \text{ s}$, $>50 \mu\text{L s}^{-1}$). However, the main features of pulmonary fluorescence distribution and the measured delivery efficiency ($76.3 \pm 23.0\%$) are in excellent agreement with observations for rapid instillation ($77.2 \pm 14.2\%$) as provided by Barapatre et al.^[29]

In vivo PB-PCXI also provides valuable insights into the mechanisms of pulmonary NM/NP delivery via ventilator-assisted aerosol inhalation. As expected there is a very gradual, uniformly distributed increase in X-ray signal with no burst-like events as seen for intratracheal instillation, which is related to aerosol deposition in the lung occurring uniformly at a relatively low delivery rate. However, even for ventilator-assisted aerosol inhalation we observed occasional localized accumulations of liquid in the upper airways near the trachea, which were gradually flowing down the airway tree reaching even the bronchiolar region (Figure 7b–d). Fluorescence imaging and fluorescence-based dosimetry revealed that a large fraction of the aerosol dose is deposited in the trachea ($\approx 60\%$ of total deposited dose) due to the spray-like aerosol stream exiting the narrow intratracheal intubation cannula. Since direct aerosol deposition in the bronchial tree would result in a more gradual process of liquid accumulation, spillover from the trachea is the most likely reason for this to occur. From the measured deposition rate (based on fluorescence) and the time of first occurrence of liquid accumulation in the airways (in vivo PB-PCXI), we determined that this nonaerosol-related transport effect occurs if more than 22 μL of liquid is nebulized. The critical liquid volume of 22 μL is expected to depend on positioning of the mouse and on ventilation parameters (breathing frequency, tidal volume, length of breath hold, and inhalation-to-exhalation time ratio). In our case, the mouse was held in upright position (for the sake of in vivo PB-PCXI), while for typical aerosol applications the mouse is laying horizontally on its back. Therefore, we recommend nebulizing as little volume as possible with the flexiVent ventilation system to avoid nonaerosol-related lung delivery processes. However, even with this artifact the delivery of NPs to the lung is much more uniform with ventilator-assisted aerosol inhalation than with intratracheal instillation on a whole lung, regional, generation, and cellular scale. It is important to note that the initially unexpected fluorescence “hot spots” detected with LSFM in the deeper bronchial region

(Figure 7h) could not have been explained without the information provided by in vivo PB-PCXI.

A prerequisite for combining X-ray and fluorescence imaging is that the co-applied active agents (X-ray absorption and fluorescence activity) have the same deposition profile in the lung. Since both agents are applied as liquid mixture, this is to be expected. This was confirmed for all contrast/fluorescence agents/mixtures used here (Table 1)—not just the clinically approved iodine—as evidenced by the excellent qualitative agreement of the spatial distribution profiles for all imaging models covering different volumes (4–100 μL), different localization (left, right, whole lung), and different degrees of spatial uniformity (patchy or uniform) of the applied liquid. QD is the only type of contrast agent (NP) that is both X-ray and fluorescence active.

Limitations of the X-ray imaging modalities were mainly related to the signal-to-noise ratio for low amounts of liquid or very uniformly distributed contrast agents. For instance ex vivo CT reached its detection limit for localized delivery of 4 μL (iodine-NP solution with 92.5 mg mL^{-1} iodine) of bulk liquid and uniformly distributed aerosol (11 μL) (Figure 4b,d and Figure 7e). Also in vivo PB-PCXI was difficult, but not impossible, for the latter case. On the other hand, fluorescence imaging on dried lungs (especially on whole lungs; WLF) was prone to widen the apparent region of particle deposition due to tissue-related light scattering effects, which can be largely eliminated by tissue clearing combined with LSFM.

As mentioned above, most of the standard imaging modalities (e.g., PA, US, CT, SPECT, PET, and MRI) are unable to visualize pulmonary fluid delivery dynamics at 1 Hz under in vivo conditions in mice mainly due to the poor spatial and temporal resolution.^[16] Recently, some multimodal imaging techniques have been used for determination of NP biodistribution and bioactivity in preclinical research. For instance, a combination of triple imaging techniques (i.e., dark-field light microscopy, electron microscopy, and nanoscale secondary ion mass spectrometry) was used to study the NP interaction with green algae in the context of NP localization, internalization, and chemical identity.^[45] Also, quantitative imaging of co-localization of tumor associated macrophages with therapeutic ^{64}Cu -labeled polyglucose nanoparticle in an orthotopic model of lung adenocarcinoma was accomplished via PET, in vivo confocal microscopy, and tissue-cleared LSFM.^[46] PCXI has already been applied for ex vivo and in vivo studies on mucociliary transport of large microparticles or 5–100 μm fibers in the trachea or upper airways of animal models such as mice and pigs^[26,47–49] and for monitoring the delivery of liquids to murine lungs via nose or intubated cannula delivery.^[16–18,25] Moreover, several common bulk particulates (e.g., lead dust, quarry dust, glass beads, asbestos, and Galena with size $\geq 5 \mu\text{m}$) were tracked in live animal trachea airways by PCXI, showing the high variability in particle movement during mucociliary transport.^[26,47,50] A few available NPs with high atomic number such as gold NPs, bismuth NPs, lanthanide-doped NPs, and tantalum pentoxide NPs as new contrast agents of X-ray-based modalities have also been studied for diagnostic and molecular imaging.^[33] However, to the best of our knowledge, real-time monitoring of the pulmonary delivery of NP suspensions has not been studied yet, and the combination of in vivo PCXI and quantitative and spatially

resolved ex vivo fluorescence imaging provided complementary insights into the mechanisms, regional/cellular distribution, and dosimetry of pulmonary drug delivery in mice. By virtue of bioactive fluorescent probes fluorescence imaging is also suitable for bioactivity studies.^[43,44] In principle the five modes of imaging presented here can be reduced to two modalities, namely, in vivo PB-PCXI and one of the three fluorescence imaging modalities, which should be selected based on the experimental constraints (available time for sample and image processing, cost, spatial resolution, etc.).

The core issue of this study is to decipher the main features of the dynamic delivery process of NPs to the nose/lung and to characterize the initial 3D NP distribution profile immediately after varied routes of pulmonary delivery. Here, NPs were suspended in liquid and delivered either as bulk liquid (nasal aspiration, intratracheal instillation) or droplets (aerosol inhalation). Consequently, the initial deposition profile of NPs mainly depends on liquid properties (e.g., delivery rate and droplet size). The more patchy, central deposition of QDs (Figure 6g) as compared to melamine NPs (Figure 6b) could be related to the higher viscosity of QD suspensions.^[27] After deposition on the lung epithelium the liquid phase of the NP suspensions will be resorbed by lung tissue and re-distribution of NPs within the lung or out of the lung (biokinetics) will depend on NP properties including size, shape, chemical composition, and surface functionalization.^[51,52] These secondary redistribution/biokinetics issues are relevant for many therapeutic and toxicological considerations, but beyond the scope of the present study. Nevertheless, they can be addressed with the imaging platform described here. A generation limitation of this study is the use of mixtures (iodine with SkyBlue, iron oxide with melamine NPs), which is not favorable for longitudinal study of NP biokinetics in the lungs as different components (active agents) possess their own pharmacokinetics. The development of bimodal contrast agents or novel NP formations suitable for both X-ray imaging and fluorescent imaging allows for combined NP pulmonary delivery and biokinetics studies since it avoids the occurrence of artifacts due to the use of two potentially interacting and/or differently behaving contrast agents. In this study, 20 nm QDs were successfully applied as an example for a bimodal NP. Alternatively, encapsulated or conjugated hybrid particles consisting of one fluorescent and one X-ray-absorbing material, such as iodinated polymers or liposomes with fluorescent dyes that have been widely used for bimodal imaging of NP accumulation in tumors,^[10,32,33,53] could be particularly useful in future pulmonary studies.

4. Conclusion

In this proof-of-concept study, we introduced and validated a multimodal imaging approach for comprehensive understanding of the mechanisms of pulmonary NP delivery in the context of dynamics of the delivery process, deposited dose, regional distribution, and cellular localization of NP in the (nondissected) whole murine lung. This imaging platform consists of in vivo PB-PCXI, ex vivo CT, and three ex vivo whole and sliced-lung epifluorescence imaging or ex vivo LSFM on tissue-cleared lungs. While each of these imaging modes has

strengths and weaknesses, selection of PB-PCXI and LSFM would not result in substantial loss of information. Mixing of particles as contrast agents for X-ray (iodine, gold NPs, iron oxide particles, and QDs) and fluorescence imaging (fluorescently labeled polystyrene or melamine NP and QDs) allowed for time-resolved (1.5 Hz) in vivo visualization of the dynamics of the pulmonary particle delivery process via intratracheal slow-instillation or ventilator-assisted aerosol inhalation with in vivo PB-PCXI. Moreover, in vivo and ex vivo X-ray particle distribution profiles were in good qualitative and quantitative agreement with regional distribution patterns observed with fluorescence imaging techniques. This implies that the two applied contrast are co-localized during and directly after delivery. Our study also reveals that for intratracheal instillation of a bulk liquid the pulmonary distribution does not primarily occur via draining of the liquid down the bronchial tree, but by secondary aerosol formation associated with liquid blockage of airways and subsequent bursting of this blockage during breathing activity. In contrast, time-resolved in vivo imaging of the ventilator-assisted aerosol inhalation process revealed slowly accumulating uniform aerosol deposition throughout the lung with occasional transport of bulk liquid into the lung. The latter is likely due to direct impaction of aerosol spray exiting the intubation cannula resulting in liquid accumulation in the trachea and eventual spillover into the bronchial region of the lung, if more than 22 μ L of liquid is nebulized. This spillover explains the initially unexpected sporadic occurrence of \approx 100–200 μ m hot-spot regions in ex vivo LSFM lung images after ventilator-assisted inhalation. Development of bimodal contrast agents like QDs, which are suitable for both in vivo PCXI and ex vivo LSFM, is expected to be particularly useful for co-visualization of controlled pulmonary delivery of NP in real time and 3D biokinetics over long term. The present study thus describes a complementary multimodal imaging platform for high temporal and spatial resolution visualization of pulmonary NP delivery in a quantitative manner, which will accelerate the ability to target active NM/drugs to the diseased region of the lung and enhance the development and efficacy of the novel-designed NM.

5. Experimental Section

By virtue of concomitant multimodal in vivo and ex vivo imaging new insights into key aspects of common preclinical and clinical methods for pulmonary substance delivery are presented. The related materials and methods are described including the diverse set of imaging modalities and the panel of methods for pulmonary substance delivery.

Materials: Each of the imaging modalities required the use of materials with specific X-ray contrast or fluoroactivity.

For X-ray phase-contrast imaging, a clinically approved iodine-based contrast agent (Ultravist-370, 370 mg iodine per milliliter) and three types of metal NPs were used, namely, gold NPs ((volume median diameter (VMD)) 20.7 ± 9.7 nm), Roti-MagBeads (magnetic iron oxide embedded in silicium oxide surface coated with carboxylic groups, VMD: 893.5 ± 348.9 nm, 10 mg mL^{-1} , Carl Roth GmbH, Karlsruhe, Germany), and Qdot 800 ITK carboxyl QDs (emission at 800 nm; VMD: $18.1 \text{ nm} \pm 6.5$ nm Invitrogen, Ltd., Paisley, UK). Gold NPs were synthesized according to manufacturer instructions using 6 mg of gold (III) chloride trihydrate ($\text{HAuCl}_4 \cdot 3\text{H}_2\text{O}$, $\geq 99.9\%$, Sigma-Aldrich) dissolved in 1 mL of deionized water. Then, 49 mL of water was added and the final gold solution was heated. When the gold solution started boiling, 0.94 mL

of a 0.04 mol L⁻¹ aqueous solution of sodium citrate (HOC(COONa) (CH₂COONa)₂·2H₂O, ≥99.0%, Sigma-Aldrich) was added to the gold solution, which was kept boiling for further 5 min. The solution changed color from transparent yellow to transparent gray, then black, and finally dark pink. Subsequently, the solution was taken from the heating plate and left stirring for 1 h in the dark, and then stored in the dark until use. The purchased QDs (stock solution: 8 × 10⁻⁶ M) were made from the crystals of a semiconductor material (CdSeTe), shelled with a ZnS layer, and further coated with a polymer layer with carboxylic groups.

For fluorescence-based microscopy, polystyrene NPs with the embedded fluorescent dye SkyBlue (excitation/emission (ex/em) = 670 nm/710 nm; VMD: 483.9 nm ± 122.3 nm; 10 mg mL⁻¹; Kisker Biotech GmbH, Steinfurt, Germany), melamine resin fluorescence particles (MF, ex/em = 636 nm/686 nm; VMD: 498 ± 111.4 nm, microParticles GmbH, Berlin, Germany), and QDs were used. The commercial MF NPs (stock suspension: 25 mg mL⁻¹) were prepared via an acid-catalyzed polycondensation reaction of melamine resin precondensates in the presence of selected fluorescent dyes in the aqueous phase.

Sizing of Nanoparticle Suspensions: Hydrodynamic diameter measurement of all NP suspension was performed with dynamic light scattering using a Malvern Zetasizer Nano instrument (Malvern Instruments Ltd., Malvern, UK) (Figure S1, Supporting Information). Of note, the observed increase of about 50% in VMD of polystyrene and melamine NPs when transferring them from water to iodine solution (from about 490 to 770 nm) (Figure S1, Supporting Information) possibly due to iodine-induced agglomeration did not adversely affect their fluorescence signals, which remained stable for more than a week after mixing (Figure S3, Supporting Information).

Animal Handling: Wildtype C57BL/6 female mice (age 9–18 weeks, 19–25 g) were housed in individually ventilated cages (IVC-Racks; Bio-Zone, Margate, UK) supplied with filtered air in a 12 h light/12 h dark cycle. Mice were provided with food (standard chow) and water ad libitum. All procedures involving animal handling and experiments were carried out in accordance with protocols approved by the Regierung von Oberbayern (District Government of Upper Bavaria, AZ55.2-1-54-2532-108.13).

The animals were anesthetized by intraperitoneal injection of a triple combination of medetomidine (0.5 mg kg⁻¹ body weight), midazolam (5 mg kg⁻¹ body weight), and fentanyl (0.05 mg kg⁻¹ body weight). The mice were then intubated by a nonsurgical technique using a 20 G cannula with one side inserted into the trachea and the other side connected to a mechanical ventilator (flexiVent FX system, Scireq Inc., Canada), allowing for exact control over the breathing activity of the mouse during pulmonary application of liquids and during in vivo acquisition of images.

Methods of Pulmonary Substance Delivery: Three widely used techniques of pulmonary delivery of liquid substances were investigated here, namely, intratracheal instillation and nasal aspiration of bulk liquids, as well as (ventilator-assisted) inhalation of aerosolized liquids. For each of these methods time-resolved in vivo monitoring of pulmonary substance delivery throughout the entire lung was performed with PB-PCXI, which is described in detail below. However, the technical details related to PB-PCXI image acquisition deserve careful attention and are therefore included in this section.

For “intratracheal slow-instillation” delivery, the setting was similar to that depicted in previous studies.^[24,25] The mice were mechanically ventilated at 90 breaths per minute, 30 mL kg⁻¹ tidal volume, and an inhalation–inflation (breath-hold)–exhalation time ratio of 1:1:1. The liquid was introduced by a heat thinned PE10 polyethylene tube that was passed through the flexible wall of the ventilator inspiratory tube. The inner PE tube was small enough not to block the intubation cannula enabling simultaneous liquid delivery and mechanical ventilation. The liquid delivery (slow-instillation) was remotely controlled by a syringe pump (UltraMicroPump III and Micro4 controller, World Precision Instruments, Sarasota, FL) that allowed for both controlled liquid delivery from outside the imaging hutch and consecutive imaging during the whole instillation process. As listed in Table 1, 100 μL of various

NP mixtures for combined X-ray and fluorescence imaging (SkyBlue-iodine: 1:20 SkyBlue (stock suspension) and 1:4 iodine; melamine-iron oxide: 1:20 melamine and 1:4 iron oxide NPs) or QDs (1:20 dilution) was continuously delivered via the syringe pump to the trachea in ≈24 s (4.2 μL s⁻¹). PB-PCXI image acquisition was performed triggered by the ventilator at a frame rate of up to 1.5 fps (frames per second) using a 200 ms (100 ms for QDs) exposure during an end of inspiration 222 ms breath-hold phase.

To study the effect of alveolar surfactant (Alveofact 45 mg mL⁻¹, Lyomark Pharma GmbH, Germany) on the pulmonary distribution of small amounts of liquids applied via intratracheal instillation, the delivery of a small volume (4 μL in 5 s, i.e., 0.8 μL s⁻¹) of an iodine-NP-surfactant mixture was investigated. The mixture contained 1:4 diluted iodine and 1:20 diluted polystyrene-SkyBlue NPs with (+) or without (–) surfactant (25 mg mL⁻¹) in distilled water. For this experiment the mice were spontaneously breathing so the ventilator was replaced with a noncontact fiber optic displacement sensor (RC-60, Philtec, MD) that was configured to detect respiratory motion and deliver an electrical trigger signal for image capture. The frame rate was maintained at 1.5 fps, but the exposure time was reduced to 100 ms to mitigate unavoidable motion blur due to the absence of a breath-hold phase. It is noteworthy that for practical reasons the liquid delivery rates of 4.0 and 0.8 μL s⁻¹ are slow compared to typical intratracheal instillation protocols delivering 50–200 μL within <1 s; by manually emptying a loaded syringe via the intubation cannula into the trachea at a delivery rate of >50 μL s⁻¹. Since less than 1 s of delivery time is too short for reliable in vivo PB-PCXI imaging of different stages of the delivery process, slower delivery rates were chosen here, and image acquisition was performed as described above.

For “ventilator-assisted aerosol inhalation,” a similar protocol and setup as described for 100 μL instillation was used (80 breath per minute, 30 mL kg⁻¹ tidal volume, 200 ms) and PB-PCXI image acquisition occurred during an end-inspiratory breath-hold phase as described above. In contrast to intratracheal slow-instillation, the inner PE10 polyethylene tube was removed and the ventilator was equipped with a nebulizer (Aeroneb Lab Small, Aerogen Inc., Galway, Ireland) in the inspiratory tubing for the generation and transport of liquid aerosol droplets to the lungs of mice. It was shown that for the flexiVent system operated under the conditions described above about 4%–5% of the nebulized liquid was deposited in the lung (downstream of trachea), with the rest being deposited in the ventilation tubing or exhaled by the mouse.^[27] Moreover, it was determined empirically that 150 μL was the maximum liquid volume that could be nebulized without at least partially blocking some part of the inspiratory ventilation tubing by accumulated rainout. Here, the nebulizer typically generated droplets with a liquid output rate of 0.26 mL min⁻¹ and a volume-weighted median diameter of 2–4.0 μm. Here, the nebulizer was breath activated and active for 40 ms during the inspiratory phase. For a breathing rate of 80 breaths per minute this corresponded to an effective liquid output rate of 13.8 μL min⁻¹ during flexiVent operation. Hence it took ≈10.8 min (870 breaths) to nebulize 150 μL liquid resulting in 5.6 μL of contrast agent deposited in the lung (3.7% of applied dose was deposited in the lung), where the dosimetric results from quantitative fluorescence spectroscopy in lung homogenates rather than the experimentally more uncertain LSFI results were relied on^[34] (Figure 7g). The aerosol delivery rate to the lung was 8.6 nL s⁻¹ (=0.0086 μL s⁻¹ = 5.6 μL/10.8 min). For some experiments, a second nebulization of 75 or 150 μL of liquid was carried out keeping the animal ventilated while drying the ventilation tube between nebulizations. For these experiments a 1:16 polystyrene NPs and 1:5 iodine mixture in distilled water was used.

For “nasal aspiration,” a similar protocol was applied as reported by Gradl et al.^[18] Briefly, a mixture of polystyrene NPs (1:10 dilution) and gold NP (1:2 dilution) suspensions was loaded into a syringe pump mentioned above, permitting controlled liquid delivery outside the imaging hutch. Here 80 μL of the polystyrene-gold liquid mixture was spontaneously inhaled via the nose by the mouse. The PB-PCXI frame rate was maintained at 1.5 fps with the exposure time of 100 ms.

In Vivo PB-PCXI: All X-ray imaging experiments were carried out at an inverse Compton scattering source—the MuCLS located at the Technical University of Munich (TUM) in Garching, Germany. The source itself was developed and installed by Lyncean Technologies Inc. (Fremont, USA),^[54,55] and the X-ray beamline infrastructure was designed and developed by TUM researchers. The source delivered a quasi-monochromatic and low divergence (4 mrad) X-ray beam. 25 keV X-rays with flux up to 2×10^{10} ph s⁻¹ were used. The principle behind propagation-based phase-contrast imaging was to use free space propagation of a partial spatial coherent beam (typically around 1 m) after penetrating a sample to introduce additional contrast. As the x-ray wavefield propagated from the sample to the detector the sample-associated phase modulations of the X-ray wavefront were converted into intensity modulations, which could be directly measured by a high-resolution X-ray detector. Here the propagation distance (sample-to-detector distance) was chosen to 1 m. There images were recorded by an Andor Zyla 5.5 sCMOS camera (2560 × 2160 pixels), combined with a 20 μm thick Gadox scintillator (Gd₂O₂S:Tb) (CRYTUR, spol. s r.o., Czech Republic) deposited on a 2:1 fiber optic taper, resulting in 13 μm detector pixel size. The source-to-sample distance was 4 m, leading to a geometric magnification of $M = 1.25$, an effective pixel size of 10.4 μm, and a beam diameter of about 16 mm. As the X-ray beam had a fixed horizontal orientation, mice needed to be positioned in a head-high position. Therefore, mice were placed in a specially designed mouse holder on an x–y–z rotation stage to facilitate positioning in the X-ray beam.^[31]

The pseudocolored images in Figures 3 and 4 are a composition of the raw PB-PCXI images (gray scale) overlaid with the colored difference image,^[24] from which a predelivery image was subtracted to highlight the location of the contrast fluid similar to the analysis performed in Donnelley et al.^[25] Images were aligned before color coding via a cross-correlation-based image registration.

Ex Vivo Lung Tomography: After intratracheal instillation or aerosolized delivery of one of the liquid NP suspensions described above, mice were sacrificed immediately by exsanguination while anaesthetized, the lung was transcidentally perfused for blood removal, and subsequently excised and either dried and inflated or optically cleared for subsequent ex vivo imaging (for a summary see Figure 1). Some of the excised lungs were mildly dried and inflated at a constant air pressure of 20–23 cm water in a microwave oven with the lowest power (10%). The lung tomography was performed on the excised, dried, and inflated lung prior to fluorescence-based microscopy. 2049 projections over 360° were captured and reconstructed with a standard fbp-reconstruction analysis. The 3D data were rendered using AVIZO or Bitplane Imaris (<http://www.bitplane.com/Imaris/Imaris>).

Ex Vivo Tissue Fluorescence Imaging: Followed by CT scan of dried lungs, the ex vivo WLF was performed using an IVIS (in vivo imaging system, Lumina II, Caliper/Perkin Elmer, USA) equipped with ex/em filters (ex/em = 640 nm/Cy5.5) suitable for the fluorescent NPs (SkyBlue). Subsequently, the dried lungs were embedded in polyurethane foam (PU foam Pattex Ultraweiss, Pattex, Germany) and sliced progressively perpendicular to the lung axis at an interval of 1 mm. After each slicing step, white light and fluorescence images of the block face and the 1 mm slice (Figure 3d) were recorded with the IVIS using ex/em = 640 nm/Cy5.5 filter. Similar IVIS imaging settings were used for all the lungs (exposure time = 2 s, binning = 1, field of view = 5, and f-stop = 1; this could be increased if saturated images occurred). Each 1 mm slice was imaged from both sides (top view and bottom view).

NP Dosimetry for the Iodine-NP-Treated and Inhaled Lungs: The autofluorescence in each NP-treated lung was subtracted to yield absolute fluorescence intensity induced by SkyBlue NPs. Three nontreated lungs were set as the background fluorescence and four typically fast-instilled lungs (50 μL 1:10 diluted or 100 μL 1:20 diluted SkyBlue NPs) were used to establish the intensity–dose standard curve for NP dosimetry (Figure S5, Supporting Information). Note that for four regular instilled lungs the SkyBlue liquid was directly injected into the mouse lung via the trachea,^[27,56] which was different from the protocol used for the slow-instilled lungs (e.g., 24 s for 100 μL liquid delivery).

The fluorophore dose in a whole lung should be principally proportional to the sum of absolute fluorescence intensities from all 1 mm slices. After yielding the desired fluorescence intensity–dose conversion curve, quantitative measurement of the deposited dose in those lungs could be achieved. The left/right/whole lung deposition analysis was carried out in the ex vivo WLF data. The background intensity was subtracted to yield the absolute fluorescence intensity of SkyBlue for each part and the fluorophore intensity could be compared.

Ex Vivo Tissue-Clearing LSFM: Other nondried lung samples were optically cleared with a modified version of the 3DISCO protocol^[57] as described in our recent study.^[27] Briefly, lung samples were dehydrated overnight in 10 mL of 50% v/v tetrahydrofuran/H₂O (THF, Sigma 186562-1L), 50% THF/H₂O 1 h, 70% THF/H₂O 4 h, 80% THF/H₂O 4 h, 100% THF 1 h, 100% THF overnight, and 100%THF 1 h with slightly shaking. Samples were gently dried and then incubated in dichloromethane (Sigma 270997-1 L) around 30 min until they sank to the bottom. Finally, samples were incubated without shaking in dibenzyl ether (DBE, Sigma 108014-1KG) for at least 2 h until imaging and then stored in DBE at room temperature.

Lung samples were scanned with an LSFM (Ultramicroscope II, LaVision Biotec) equipped with a sCMOS camera (Andor Neo) and a 2× objective lens (Olympus MVPLAPO 2×/0.5 numerical aperture (NA)) equipped with an Olympus MVX-10 zoom body, which provided zoom-out and -in ranging from 0.63× up to 6.3×. For the whole lung imaging, light sheet scans were generated with 0.63× zoom magnification with individual ex/em bandpass filters for melamine NPs (ex/em = 640(30) nm/690(50) nm) and QDs (ex/em = 640(30) nm/795(50) nm) with a step size of 10 μm. Tissue autofluorescence was imaged under the ex/em = 545(30) nm/605(70) nm filters. Samples were typically imaged with an exposure time of 150 ms, at a full laser power with the light sheet by adjusting xy width and NA to the sample size. High magnification scans (e.g., 8× in Figure 6e,f) were usually performed with a step size of 4 μm. The imaging chamber was filled with DBE.

Image Processing and Analysis: All (X-ray and CT) images were flat field and dark current corrected. X-ray images were analyzed and the dynamic NP delivery videos were generated using ImageJ (<https://imagej.nih.gov/ij/>). Fluorescence images scanned by IVIS consisting of whole lung images and dried lung slices and their corresponding NP dosimetry analysis were performed with the Living Imaging 4.0 Software (Caliper). The 3D images with maximum intensity projection and videos with 3D manipulation scanned by LSFM were processed using Bitplane Imaris. All data were presented as mean ± standard deviation and *, **, and *** refer to statistically significant differences $P < 0.05$, $P < 0.01$, and $P < 0.001$, respectively, and plotted using SigmaPlot version 12.0 (Systat Software GmbH, Germany). $N \geq 3$.

Supporting Information

Supporting Information is available from the Wiley Online Library or from the author.

Acknowledgements

The authors thank Lyncean Technologies Inc. for the technical support of the compact synchrotron light source. The authors also acknowledge financial support through the Centre for Advanced Laser Applications (CALA), and the DFG Gottfried Wilhelm Leibniz program. This research was (partially) supported through the EU Horizon 2020 project SmartNanoTox (grant agreement No. 686098). The authors thank the China Scholarship Council (CSC) for providing the fellowship for L.Y. (201506820008). K.S.M. was supported by a Veski VPRF, ARC FT180100374, and NHRMC GNT1140617; and K.S.M., R.G., and F.P. completed this work with the support of the TUM Institute for Advanced Study, funded by the German Excellence Initiative and the European

Union Seventh Framework Program under grant agreement No. 291763, and co-funded by the European Union. M. Do was supported by NHMRC project GNT1160011, and by a Robinson Research Institute Career Development Fellowship. The authors also thank Juliana Martins de Silva for the production of the gold NPs.

Conflict of Interest

The authors declare no conflict of interest.

Keywords

aerosol inhalation therapy, lung fluorescence imaging, optical tissue clearing, pulmonary delivery, X-ray imaging

Received: July 27, 2019
Revised: September 12, 2019
Published online:

- [1] WHO, The Top 10 Causes of Death, <https://www.who.int/news-room/fact-sheets/detail/the-top-10-causes-of-death> (accessed: May 2018).
- [2] W. H. Lee, C. Y. Loo, D. Traini, P. M. Young, *Asian J Pharm. Sci.* **2015**, *10*, 481.
- [3] M. B. Dolovich, R. Dhand, *Lancet* **2011**, *377*, 1032.
- [4] S. Azarmi, W. H. Roa, R. Lobenberg, *Adv. Drug Delivery Rev.* **2008**, *60*, 863.
- [5] C. Loira-Pastoriza, J. Todoroff, R. Vanbever, *Adv. Drug Delivery Rev.* **2014**, *75*, 81.
- [6] J. Liu, R. Zhang, Z. P. Xu, *Small* **2019**, *15*, 1900262.
- [7] J. Shi, P. W. Kantoff, R. Wooster, O. C. Farokhzad, *Nat. Rev. Cancer* **2017**, *17*, 20.
- [8] M. Doroudian, R. MacLoughlin, F. Poynton, A. Prina-Mello, S. C. Donnelly, *Thorax* **2019**, *74*, 965.
- [9] S. Wilhelm, A. J. Tavares, Q. Dai, S. Ohta, J. Audet, H. F. Dvorak, W. C. W. Chan, *Nat. Rev. Mater.* **2016**, *1*, 16014.
- [10] S. Kunjachan, J. Ehling, G. Storm, F. Kiessling, T. Lammers, *Chem. Rev.* **2015**, *115*, 10907.
- [11] B. Pelaz, C. H. Alexiou, R. A. Alvarez -Puebla, F. Alves, A. M. Andrews, S. Ashraf, L. P. Balogh, L. Ballerini, A. Bestetti, C. Brendel, S. Bosi, M. Carril, W. C. W. Chan, C. Y. Chen, X. D. Chen, X. Y. Chen, Z. Cheng, D. X. Cui, J. Z. Du, C. Dullin, A. Escudero, N. Feliu, M. Y. Gao, M. George, Y. Gogotsi, A. Grunweller, Z. W. Gu, N. J. Halas, N. Hampp, R. K. Hartmann, M. C. Hersam, P. Hunziker, J. Jian, X. Y. Jiang, P. Jungebluth, P. Kadhiresan, K. Kataoka, A. Khademhosseini, J. Kopecek, N. A. Kotov, H. F. Krug, D. S. Lee, C. M. Lehr, K. W. Leong, X. J. Liang, M. L. Lim, L. M. Liz-Marzan, A. M. Ma, P. Macchiariini, H. Meng, H. Mohwald, P. Mulvaney, A. E. Nel, S. M. Nie, P. Nordlander, T. Okano, J. Oliveira, T. H. Park, R. M. Penner, M. Prato, V. Puentes, V. M. Rotello, A. Samarakoon, R. E. Schaak, Y. Q. Shen, S. Sjoqvist, A. G. Skirtach, M. G. Soliman, M. M. Stevens, H. W. Sung, B. Z. Tang, R. Tietze, B. N. Udugama, J. S. VanEpps, T. Weil, P. S. Weiss, I. Willner, Y. Z. Wu, L. L. Yang, Z. Yue, Q. Zhang, Q. Zhang, X. E. Zhang, Y. L. Zhao, X. Zhou, W. J. Parak, *ACS Nano* **2017**, *11*, 2313.
- [12] J. Biederer, S. Mirsadraee, M. Beer, F. Molinari, C. Hintze, G. Bauman, M. Both, E. J. Van Beek, J. Wild, M. Puderbach, *Insights Imaging* **2012**, *3*, 373.
- [13] C. Hoyer, N. Gass, W. Weber-Fahr, A. Sartorius, *Neuropsychobiology* **2014**, *69*, 187.
- [14] M. Eghtedari, A. Oraevsky, J. A. Copland, N. A. Kotov, A. Conjunteau, M. Motamedi, *Nano Lett.* **2007**, *7*, 1914.
- [15] A. Taruttis, V. Ntziachristos, *Nat. Photonics* **2015**, *9*, 219.
- [16] M. Donnelley, K. S. Morgan, K. K. Siu, D. W. Parsons, *J. Aerosol Med. Pulm. Drug Delivery* **2013**, *26*, 307.
- [17] L. Porra, L. Degrugilliers, L. Broche, G. Albu, S. Strengell, H. Suhonen, G. H. Fodor, F. Petak, P. Suortti, W. Habre, A. R. A. Sovijarvi, S. Bayat, *Sci. Rep.* **2018**, *8*, 3519.
- [18] R. Gradl, M. Dierolf, B. Gunther, L. Hehn, W. Moller, D. Kutschke, L. Yang, M. Donnelley, R. Murrie, A. Erl, T. Stoeger, B. Gleich, K. Achterhold, O. Schmid, F. Pfeiffer, K. S. Morgan, *Sci. Rep.* **2018**, *8*, 6788.
- [19] F. G. Meinel, F. Schwab, S. Schleede, M. Bech, J. Herzen, K. Achterhold, S. Auweter, F. Bamberg, A. O. Yildirim, A. Bohla, O. Eickelberg, R. Loewen, M. Gifford, R. Ruth, M. F. Reiser, F. Pfeiffer, K. Nikolaou, *PLoS One* **2013**, *8*, e59526.
- [20] S. Aryal, J. Key, C. Stigliano, M. D. Landis, D. Y. Lee, P. Decuzzi, *Small* **2014**, *10*, 2688.
- [21] N. Karra, T. Nassar, A. N. Ripin, O. Schwob, J. Borlak, S. Benita, *Small* **2013**, *9*, 4221.
- [22] C. Xu, P. Wang, J. Zhang, H. Tian, K. Park, X. Chen, *Small* **2015**, *11*, 4321.
- [23] C. S. Schneider, Q. G. Xu, N. J. Boylan, J. Chisholm, B. C. Tang, B. S. Schuster, A. Henning, L. M. Ensign, E. Lee, P. Adstamongkonkul, B. W. Simons, S. Y. S. Wang, X. Q. Gong, T. Yu, M. P. Boyle, J. S. Suk, J. Hanes, *Sci. Adv.* **2017**, *3*, e1601556.
- [24] R. Gradl, M. Dierolf, L. Yang, L. Hehn, B. Gunther, W. Moller, D. Kutschke, T. Stoeger, B. Gleich, K. Achterhold, M. Donnelley, F. Pfeiffer, O. Schmid, K. S. Morgan, *J. Controlled Release* **2019**, *307*, 282.
- [25] M. Donnelley, K. K. Siu, R. A. Jamison, D. W. Parsons, *Gene Ther.* **2012**, *19*, 8.
- [26] M. Donnelley, K. S. Morgan, K. K. W. Siu, D. W. Parsons, *Synchrotron Radiat.* **2012**, *19*, 551.
- [27] L. Yang, A. Feuchtinger, W. Moller, Y. Ding, D. Kutschke, G. Moller, J. C. Schittny, G. Burgstaller, W. Hofmann, T. Stoeger, R. Daniel, A. Walch, O. Schmid, *ACS Nano* **2019**, *13*, 1029.
- [28] D. Yi, A. Price, A. Panoskaltis-Mortari, A. Naqwi, T. S. Wiedmann, *Anal. Biochem.* **2010**, *403*, 88.
- [29] N. Barapatre, P. Symvoulidis, W. Moller, F. Prade, N. C. Deliolanis, S. Hertel, G. Winter, A. O. Yildirim, T. Stoeger, O. Eickelberg, V. Ntziachristos, O. Schmid, *J. Pharm. Biomed. Anal.* **2015**, *102*, 129.
- [30] E. J. Veldhuizen, H. P. Haagsman, *Biochim. Biophys. Acta, Biomembr.* **2000**, *1467*, 255.
- [31] K. S. Morgan, D. Parsons, P. Cmielewski, A. McCarron, R. Gradl, N. Farrow, K. Siu, A. Takeuchi, Y. Sukuji, K. Uesugi, M. Uesugi, N. Yagi, C. Hall, M. Klein, A. Maksimenko, A. Stevenson, D. Hausermann, M. Dierolf, F. Pfeiffer, M. Donnelley, unpublished.
- [32] H. Lusic, M. W. Grinstaff, *Chem. Rev.* **2013**, *113*, 1641.
- [33] J. C. De La Vega, U. O. Hafeli, *Contrast Media Mol. Imaging* **2015**, *10*, 81.
- [34] S. H. van Rijt, D. A. Bolukbas, C. Argyo, K. Wipplinger, M. Naureen, S. Datz, O. Eickelberg, S. Meiners, T. Bein, O. Schmid, T. Stoeger, *Nanoscale* **2016**, *8*, 8058.
- [35] S. Hussain, J. Joo, J. Kang, B. Kim, G. B. Braun, Z. G. She, D. Kim, A. P. Mann, T. Molder, T. Teesalu, S. Carnazza, S. Guglielmino, M. J. Sailor, E. Ruoslahti, *Nat. Biomed. Eng.* **2018**, *2*, 95.
- [36] P. Muralidharan, M. Malapit, E. Mallory, D. Hayes Jr., H. M. Mansour, *Nanomedicine* **2015**, *11*, 1189.
- [37] F. S. Collins, H. Varmus, *N. Engl. J. Med.* **2015**, *372*, 793.
- [38] O. Schmid, T. Stoeger, *J. Aerosol Sci.* **2016**, *99*, 133.
- [39] K. Ganguly, D. Ettehadieh, S. Upadhyay, S. Takenaka, T. Adler, E. Karg, F. Krombach, W. G. Kreyling, H. Schulz, O. Schmid, T. Stoeger, *Part. Fibre Toxicol.* **2017**, *14*, 19.
- [40] X. Duan, Y. Li, *Small* **2013**, *9*, 1521.

- [41] L. Yang, H. Kuang, W. Zhang, Z. P. Aguilar, H. Wei, H. Xu, *Sci. Rep.* **2017**, *7*, 3303.
- [42] O. Schmid, F. R. Cassee, *Part. Fibre Toxicol.* **2017**, *14*, 52.
- [43] B. Drasler, D. Vanhecke, L. Rodriguez-Lorenzo, A. Petri-Fink, B. Rothen-Rutishauser, *Nanomedicine* **2017**, *12*, 1095.
- [44] D. Vanhecke, L. Rodriguez-Lorenzo, M. J. D. Clift, F. Blank, A. Petri-Fink, B. Rothen-Rutishauser, *Nanomedicine* **2014**, *9*, 1885.
- [45] R. Sekine, K. L. Moore, M. Matzke, P. Vallotton, H. Jiang, G. M. Hughes, J. K. Kirby, E. Donner, C. R. M. Grovenor, C. Svendsen, E. Lombi, *ACS Nano* **2017**, *11*, 10894.
- [46] H. Y. Kim, R. Li, T. S. C. Ng, G. Courties, C. B. Rodell, M. Prytyskach, R. H. Kohler, M. J. Pittet, M. Nahrendorf, R. Weissleder, M. A. Miller, *ACS Nano* **2018**, *12*, 12015.
- [47] M. Donnelley, K. K. W. Siu, K. S. Morgan, W. Skinner, Y. Suzuki, A. Takeuchi, K. Uesugi, N. Yagi, D. W. Parsons, *J. Synchrotron Radiat.* **2010**, *17*, 719.
- [48] M. Donnelley, K. S. Morgan, K. K. Siu, N. R. Farrow, C. S. Stahr, R. C. Boucher, A. Fouras, D. W. Parsons, *Sci. Rep.* **2015**, *4*, 3689.
- [49] M. Donnelley, K. S. Morgan, M. Awadalla, N. R. Farrow, C. Hall, D. W. Parsons, *Respir. Res.* **2017**, *18*, 95.
- [50] M. Donnelley, K. S. Morgan, A. Fouras, W. Skinner, K. Uesugi, N. Yagi, K. K. Siu, D. W. Parsons, *J. Synchrotron Radiat.* **2009**, *16*, 553.
- [51] W. G. Kreyling, S. Hirn, W. Moller, C. Schleh, A. Wenk, G. Celik, J. Lipka, M. Schaffler, N. Haberl, B. D. Johnston, R. Sperling, G. Schmid, U. Simon, W. J. Parak, M. Semmler-Behnke, *ACS Nano* **2014**, *8*, 222.
- [52] H. S. Choi, Y. Ashitate, J. H. Lee, S. H. Kim, A. Matsui, N. Insin, M. G. Bawendi, M. Semmler-Behnke, J. V. Frangioni, A. Tsuda, *Nat. Biotechnol.* **2010**, *28*, 1300.
- [53] J. Harrison, C. A. Bartlett, G. Cowin, P. K. Nicholls, C. W. Evans, T. D. Clemons, B. Zdyrko, I. A. Luzinov, A. R. Harvey, K. S. Iyer, S. A. Dunlop, M. Fitzgerald, *Small* **2012**, *8*, 1579.
- [54] E. Eggel, M. Dierolf, K. Achterhold, C. Jud, B. Gunther, E. Braig, B. Gleich, F. Pfeiffer, *J. Synchrotron Radiat.* **2016**, *23*, 1137.
- [55] K. Achterhold, M. Bech, S. Schleede, G. Potdevin, R. Ruth, R. Loewen, F. Pfeiffer, *Sci. Rep.* **2013**, *3*, 1313.
- [56] A. A. Gotz, J. Rozman, H. G. Rodel, H. Fuchs, V. Gailus-Durner, M. H. de Angelis, M. Klingenspor, T. Stoeger, *Part. Fibre Toxicol.* **2011**, *8*, 30.
- [57] A. Erturk, K. Becker, N. Jahrling, C. P. Mauch, C. D. Hojer, J. G. Egen, F. Hellal, F. Bradke, M. Sheng, H. U. Dodt, *Nat. Protoc.* **2012**, *7*, 1983.



Multimodal Precision Imaging of Pulmonary Nanoparticle Delivery in Mice: Dynamics of Application, Spatial Distribution, and Dosimetry

Author: Otmar Schmid, Kaye S. Morgan, Franz Pfeiffer, et al

Publication: Small

Publisher: John Wiley and Sons

Date: Oct 22, 2019

© 2019 The Authors. Published by WILEY-VCH Verlag GmbH & Co. KGaA, Weinheim

Welcome to RightsLink

This article is available under the terms of the [Creative Commons Attribution License \(CC BY\)](#) (which may be updated from time to time) and permits use, distribution and reproduction in any medium, provided that the Contribution is properly cited.

For an understanding of what is meant by the terms of the [Creative Commons License](#), please refer to [Wiley's Open Access Terms and Conditions](#).

Permission is not required for this type of reuse.

Wiley offers a professional reprint service for high quality reproduction of articles from over 1400 scientific and medical journals. Wiley's reprint service offers:

- Peer reviewed research or reviews
- Tailored collections of articles
- A professional high quality finish
- Glossy journal style color covers
- Company or brand customisation
- Language translations
- Prompt turnaround times and delivery directly to your office, warehouse or congress.

Please contact our Reprints department for a quotation. Email corporatesaleseurope@wiley.com or corporatesalesusa@wiley.com or corporatesalesDE@wiley.com.

CLOSE WINDOW

5. Discussion

Aerosol inhalation delivery of the drug or NM/NPs to the respiratory system is the primary route for the treatment of lung infections and diseases such as asthma, cystic fibrosis, and COPD, which has been widely used not only in preclinical studies but also at clinical settings^{15, 115}. Time- and spatially-resolved targeted delivery of drug/NM to the specific lung regions or sites is fundamental for drug efficacy and toxicological studies¹¹⁶. Depending on the type of lung disease, a therapeutic drug/NM should be preferably delivered to the specific tissue regions or cells. For instance, SCLC and squamous cell carcinomas require delivering a drug/NM at the large bronchi where the occurrence of cancer, whereas the alveolar (or the acinar) deposition of drug/NM is necessary for large cell carcinomas and adenocarcinomas¹¹⁷. Moreover, the associated health effects of NM/NPs also greatly rely on the site of NP deposition in the lung of animal models after pulmonary delivery. Particles with size larger than 1 μm are primarily limited to accumulate in the airway, which was considered that can be excluded quickly by mucociliary transport¹¹⁸. In contrast, smaller NPs (less than 200 nm) are conceived to be delivered deep enough to enter into the alveolar regions, possessing the prolonged residence time, reduced phagocytosis, and high translocation ability of NPs to the vasculature system²⁷⁻²⁸. While comprehensive understanding of the pulmonary NP delivery, distribution, and biokinetics in entire organs is of central significance for precision medicine, there are no effective imaging tools to resolve those issues. In this study, we thus first successfully presented a single-modality imaging technique namely tissue-cleared LSFM to address the limitations maintained by conventional analyzed methods on 3D characterization of lung morphology, whole-organ visualization of NPs at single cell level, and quantitative NP dosimetry (PRP1). Secondly, a multimodal imaging approach including both *in vivo* X-ray and *ex vivo* fluorescence imaging methods was established to investigate the specific features and mechanisms of three types of commonly used pulmonary delivered routes namely nasal aspiration, intratracheal instillation, and ventilator-assisted aerosol inhalation (PRP2).

In the first study (PRP1), the spatially-resolved imaging technique includes the use of tissue optical clearing to eliminate the light scattering and absorption and sequential light-sheet scan of the whole lung utilizing LSFM to allow for 3D reconstruction of lung structure and NP distribution. A prerequisite of this method is to select a suitable and effective clearing protocol that preserves the fluorescence intensity of fluorescent particles, dyes, or proteins over the treatment of clearing solvents with high quality of optical transparency. Currently,

there are various kinds of tissue clearing methods such as organic solvent-based protocols¹¹⁹⁻¹²⁰ (*e.g.*, 3DISCO, μ DISCO, and vDISCO), aqueous-based clearing methods (*e.g.*, SeeDB, CUBIC, and FRUIT)¹²¹ and hydrogel-based clearing protocols (*e.g.*, PAT/PARS and CLARITY)¹²². A modified 3DISCO was utilized to clear the lung samples in this study as it was considered as the most effective method in terms of the degree of transparency and time consumption (within hours to 1-2 days). Tissue optical clearing is nowadays widely being performed in the different research fields particularly in neurobiology and embryology to observe the brain activity, nerve connection, and embryo development^{119, 121, 123}, a few studies, however, have also applied it to study the basic lung structure and development¹²⁴⁻¹²⁵, lung fibrosis¹²⁶, formation of bronchus associated lymphoid tissue during lung infection¹²⁷, and macrophage infiltration in lung tumors¹²⁸. Tissue-clearing 3D visualization of NP distribution in intact organs is largely unexplored. To the best of our knowledge, current existed studies have only been reported that the application of tissue-cleared LSFM to investigate NP localization in the organs/tissues (the liver, spleen, and tumor) other than the lungs¹²⁹⁻¹³¹. Although the most of NPs were found to accumulate in the regions of proximal to blood vessels in both the health and tumor tissues by simultaneously detecting the NP scattering signal and tissue (immune- or auto-) fluorescence¹³⁰⁻¹³¹, the used clearing method CLARTIY not only is time-consuming and much more complicated but also potentially destroy the tissue structure¹³². Another important consideration for tissue-cleared LSFM is that the fluorescence proteins, dyes, and particles might be bleached or degraded during the process of tissue clearing and then it is critical to know whether the NPs are compatible with clearing protocols. A convenient and reliable *ex vivo* WLFI using IVIS was first introduced to evaluate the fluorescence stability of NPs and tissue shrinkage by imaging lung samples after each processing step from initial body perfusion to final matching RI. In this study, three different types of NPs were tested and found that QDs and MF were stable enough while polystyrene latex NPs lost their fluorescence, which could be partially due to the degradation or bleaching of dyes. Some different mild water-based clearing protocols such as CUBIC should be considered for different types of fluorescent particles, which beyond the scope of this study and thus not be further investigated. Overall, *ex vivo* WLFI using IVIS will be a reliable and robust method for the selection of suitable fluorescent tracers and measurement of the tissue shrinkage/expansion, as well as for optimization of clearing protocols in future research.

Accurate quantification of lung morphometry in intact or dissected organs with high resolution is quite challenging for both non-invasive (*in vivo*) and destructive (*ex vivo*) imaging methods due to the millions of gas-exchanging alveoli connecting terminals of the conducting airway tree, yielding to the changeable lung volume. The fundamental lung structural parameters including airways length and diameters, wall thickness, and alveolar MCL are commonly utilized as physiology/diagnostic indicators for lung diseases in both preclinical research and clinical settings like the narrowed airways are the hallmark in asthma patients¹³³. Traditionally, morphometric analysis of the lungs of humans and animal models has been typically performed in HE-stained lung sections under light microscope using a coherent test line system based on point and intersection counting utilization of the computer-assisted stereological toolbox (CAST)¹³⁴. Recently, *in vivo* and *ex vivo* CT is also widely performed for quantitative measurements of lung structure of both animal models and patients due to the avoidance of lung slicing, preservation of breath state of the lung, and time-saving procedures^{95, 135}. Generally speaking, conventional 2D stereological methods require tedious laboratory efforts due to the tissue slicing, staining, slice-by-slice microscopy, and manual counting, as well as lost the 3D information, while *ex vivo* tissue-cleared LSFM enables planewise imaging of the entire lung at the cellular and even subcellular level in a relatively short time. Additionally, compared to X-ray based approaches, LSFM had much better resolution and wider selection of fluorescent agents than the X-ray contrast agents for performing the functional imaging. This study thus for the first time shows the 3D whole lung structure with cellular resolution and provides the morphometric analysis of bronchial trees and alveoli in adult murine animals based on LSFM data. Future more accurate and automatic analysis of lung architecture can be performed by establishing methods of algorithms or machine learning to determine *e.g.*, the surface area of airways and acini. Corrections for tissue shrinkage and collapsed state of lung are critical as parameters of lung structure crucially depend on lung volume varying with its inflated level. Overall, tissue-clearing LSFM offers new insights for whole lung morphometry with cellular resolution including the visualization and quantification of conducting airways, alveoli, vasculature system (by intravenous injection of lectin or CD31 antibody, endothelial cell markers)¹³⁶, and specific cells.

This study further verifies that the tissue-cleared LSFM enables co-mapping of lung morphology and NP distribution with cellular resolution in murine lungs after two types of pulmonary delivery namely intratracheal instillation and ventilator-assisted aerosol inhalation.

Qualitative 3D visualization of NP distribution illuminates that instillation delivery displays a much patchier and central deposition of NPs in the intact lung compared to that of delivered by ventilator-assisted aerosol inhalation, which is further proved by quantification of deposition ratio of central-to-peripheral. Ventilator-assisted aerosol inhalation exhibits a homogeneous distribution as indicated by central-to-peripheral deposition ratio equal to 0.98 ± 0.13 versus 1.98 ± 0.37 for instillation (preferentially central deposition). Quantitative analysis of delivered doses in inhaled lungs after the establishment of dose-intensity standard curve using known amount of instilled lungs revealed that about 4.2% of applied doses can be deposited to the lung, which is in good consistent with the homogenization data with 8% deposition. Lobe wise deposition analysis also shows that around 40% of deposited dose accumulated to the left lung and a relatively uniform NP deposition in different lung lobes when considered to the volume-weighted NP deposition. Although an even distribution of NPs among the bronchioles and acini was clearly evident in the lungs of mice after ventilator-assisted aerosol inhalation, a significant finding was that NPs are predominantly deposited in the proximal part of individual acini.

The above features possessed by tissue-cleared LSFM applied in lungs represent substantial progress over commonly used *in vivo* and *ex vivo* optical imaging techniques, which are only able to offer the semi-quantitative information on NP dose and biodistribution in the tissue because of the strong tissue autofluorescence and poor spatial resolution. Whole-body fluorescence imaging or WLFIm using FMT or IVIS can only be used for quantitative visualization of the distribution pattern of drug in the whole body or organ. For instance, hybrid imaging combined FMT and micro-CT has been used to observe the NM (pHPMA-Dy750) distribution in different organs of mice bearing CT26 tumors *in vivo*¹³⁷ and IVIS whole body imaging displays a more uniform and deeper distribution of dry powder in mouse lung with delivery using an aerosol generator than the use of Penn-Century insufflator⁹⁶. Also, *ex vivo* LSFM such as cryo-slicing and compressed-lung fluorescence imaging⁴²⁻⁴³ enables relatively good quantification accuracy on NP regional distribution and dosimetry, but with apparent limitations with respect to the poor spatial resolution. Other currently available *in vivo* imaging techniques like PCXI, CT, MRI, PET, and SPECT offer anatomical and/or functional imaging of NP deposition, while they generally require expensive instrumentation and the process of radiolabeling or the use of contrast agents with limited spatial resolution. This greatly hampers the inspection of cellular activities and fate like NP phagocytosis or endocytosis and lung inflammation (local recruitment and

accumulation of neutrophils), which can be overcome by the established method in this study. 2D stereological methods, by contrast, allow for cellular-resolution observation of NP localization, but the 3D morphological information was totally spoiled. This single imaging modality presented here overcomes some of above issues by planewise LSM imaging of tissue-cleared samples which enables label-free morphological analysis with quantitative NP distribution at single-cell level on whole organ or thick tissue layer. This therefore offers unappreciated insights into 3D distribution and biokinetics of drug/NPs and by combining with multicolor whole-mount immunostaining it opens new avenues for future drug efficacy and toxicological studies.

In the second study (PRP2), a marriage of X-ray and fluorescent imaging was employed to fully understand the pulmonary NM/NP delivery to the lungs in a preclinical animal model (mice) consisting of the dynamic process, delivered dose, spatial distribution, biokinetics, and bioactivity of the NM/NPs on all scales ranging from centimeter (whole lung) to sub-micrometer (subcellular) resolution. Conventional X-ray imaging typically displays low contrast for soft tissue *e.g.*, the lung, while the boundaries between lung tissue and air can be substantially enhanced by their variations in X-ray refractive index using phase-contrast techniques¹⁰⁶. PB-PCXI is therefore particularly useful for dramatically enhancing soft tissue (*e.g.*, the lung) contrast by utilizing X-ray refraction and associated phase shifts at air-tissue interfaces¹⁰⁶. To observe the treatment process of pulmonary delivery, the acquisition of a single image should be captured in a relatively short time (*e.g.*, about 100 ms). PB-PCXI applied here only requires a single exposure for a lung scan, exhibiting great possibility to track dynamic process. Other standard imaging modalities (*e.g.*, CT, PET, SPECT, and MRI) are generally incapable of capturing pulmonary fluid dosing dynamics via the mouse nose or lung *in vivo* mainly because of poor temporal and spatial resolution⁹³. In an early study, delivery of a 50 μ L iodine-based liquid to the mouse lung *via* intratracheal slow-instillation was visualized in real-time⁴⁹. This indicates that capturing the dynamics of pulmonary delivery is achievable using PCXI at a laboratory compact X-ray source, an experiment that would typically be carried out at synchrotron facility^{107, 138}. One of the limitations of PCXI and CT imaging methods presented here is the difficulty associated with accurate dosimetry analysis, given that X-ray contrast originates from the anatomy and the treatment, so it is not as easily isolated as a fluorescent signal. Optical imaging modalities offer the necessary complementary features. Particularly, *ex vivo* LSM as an emerging optical imaging method allows for 3D imaging of whole NP distribution profile in whole lungs after rendering the

tissue transparent, eliminating or minimizing the tissue absorption and scattering¹⁸. The main characteristics and complementarities of all five imaging methods applied here are summarized in Table 1 (PRP2). This study therefore demonstrates that combined *in vivo* PCXI and *ex vivo* fluorescent imaging can offer complementary and unappreciated insights into the complex process of different routes of NP delivery to the lung of mice with administration of a mixture of an X-ray contrast agent and fluorescent NPs.

The key issue of this study is to understand the main features and mechanisms of different types of pulmonary delivery. Instillation or aspiration of bulk liquids is the commonly utilized approach for preclinical lung research, while aerosol inhalation is the optimal route for the clinical practice. Here we therefore applied three kinds of pulmonary delivery (intratracheal instillation, nasal aspiration, and aerosol inhalation) to determine their respective characteristics of the dynamic process and initial 3D NP distribution pattern. Intratracheal slow-instillation (*e.g.*, 24 s for 100 μL ; 4.2 $\mu\text{L/s}$) is used here since the regular instillation that is typically occurred within 1 s cannot be captured by PCXI. However, they show the very identical delivery efficiency in a 50 μL liquid delivery (the former $76.3 \pm 23.0\%$ versus the latter $77.2 \pm 14.2\%$ ⁴²). Also, the delivered dose to the lung is independent with the applied volumes ranging from 4-100 μL . We first performed time-resolved imaging of the site-specific NP delivery to the left, right, or whole lung utilizing PB-PCXI in a controllable manner with a slow-instillation of the mixture of iodine with fluorescent NPs. This is of significance for targeted delivery and could be used to test the mechanisms of drug efficacy or toxicity in one side of the lung while the other side served as a control. This direct noninvasive visualization of the behavior of NP-liquid in murine airways also for the first time clearly discloses the underlying mechanism of uniformity degree of pulmonary instillation that partial blockage of airways with subsequent distribution by breathing activity. Moreover, the site of NP-liquid deposition in slow-instillation can be qualitatively observed in PCXI images, which generally show good correlation with that in the subsequent images obtained from CT and fluorescent imaging (WLF, LSFI, and LSFM).

Leveraging the multimodality imaging established above, this study further unveils the mechanisms of lung delivery via ventilator-assisted aerosol inhalation. This method is technologically mature, high efficient, and dose controllable for physiologic delivery of liquid aerosol droplets to the mouse lungs. Of note, during pure aerosol delivery, the transport of aerosols containing iodine-NP through primary airways to the lower airways could not be seen, while after delivery of around 22 μL liquid aerosols (calculated from 3 inhaled lungs

where the first appearance of the liquid accumulation and transportation), some liquid droplets or bubbles were formed and halted for a few seconds and then burst and distributed to lower airways. This could explain that some NPs appearing as circular drops (100-200 μm) were located in certain regions of the lower airways, which is inconsistent with our previous finding¹⁸. Clearly homogenous distribution of NP after inhalation was observed in images of CT, WLFI, and LSFM, while only very specific local regional distribution was tracked using *in vivo* PCXI. This could be due to the droplets/aerosols having lower iodine density and longer delivery time (8.6 nL/s, 10.8 min) in inhalation than the liquid for slow-instillation (velocity: 4.2 $\mu\text{L/s}$). Lower iodine density during inhalation with very slow delivery (longer inhalation time) could play an important role in weak/no signal detection by X-ray imaging. However, for 4 μl instillation, they passed the trachea as liquid with high iodine concentration/density in short delivery time so that they can be relatively easily detected.

Currently, PCXI has been mainly used to track particle movement of mucociliary transport for different bulk particulates (*e.g.*, glass beads, lead dust, asbestos, quarry dust, and Galena with size $\geq 5 \mu\text{m}$) in live animal trachea airways,^{106, 139-140} and to monitor the liquid bolus delivery via the nose or inserted cannula by utilizing the typical X-ray contrast agents like iodine and lanthanides¹⁴¹. Due to the high atomic number, several new types of NPs including lanthanide-doped NPs, bismuth NPs, gold NPs, and tantalum pentoxide NPs can be also served as contrast agents for X-ray based modalities to perform the diagnostic and molecular imaging¹⁴². To the best of our knowledge, time-resolved tracking of the NP suspension for pulmonary fluid dosing delivery has not previously been reported. Taking advantage of high X-ray absorption of iodine, NP suspension mixed with iodine was first observed by PCXI during slow-instillation delivery⁴⁹. Tracking sole NP suspension during pulmonary dynamic delivery remains unexplored. Three particle suspensions (mixed with another fluorescent melamine NPs or sole QDs) were then applied to visualize the NP-liquid dosing delivery *via* mouse nose and trachea. The dynamics of gold NP distribution during and immediately after delivery into one nostril of the mouse nose was visualized during nasal aspiration, while this route of delivery was hard to predict the distribution pattern and dose into the lungs. Slow-instillation *via* an intubated cannula in the trachea was first performed to effectively deliver iron oxide particles or QDs into deep lung regions, which could be of value for prevention or treatment of respiratory disease in preclinical studies. PCXI hence permits monitoring of the real-time delivery dynamics and deposition regions of NPs in lungs.

Subsequent *ex vivo* tissue-cleared LSFM offers 3D cellular visualization of NP localization and quantitative dosimetry ability in non-dissected lungs.

An important consideration is the detection limit of the liquid distribution in the X-ray images presented here. PCXI allows for visualization of as little as a 4 μ L iodine-NP solution (with or without added surfactant) in real time, suggesting the very high contrast sensitive in tracking NP-liquid for slow-instillation delivery. In contrast to PCXI images, CT scans of the lung with such little volume display no obvious signals. However, WLF and LSF using IVIS enable qualitative viewing of the small volume of NP-liquid deposition or quantitatively measure the delivered dose, respectively in lungs independent of surfactant. Tissue-cleared LSFM could further eliminate the tissue light scattering and absorption, which enables more precise observation of the NP localization and quantitatively regional dosimetry. To successfully apply this multimodal imaging platform, one should consider the joint use of X-ray contrast agents and fluoroactive substances which should have the exact same initial deposition pattern. This is to be expected as the substances are mixed and applied as a liquid mixture. On the other hand, the apparent limitation of co-application of two agents is that it is not suitable for long term study like NP biokinetics since different components having their own pharmacodynamics may separate one from the other. X-ray contrast agent- and fluorescence-labeled NP formations such as (iodinated polymers or liposomes with fluorescent dyes) have been used for bimodal imaging of NPs accumulation in tumors^{7, 141-142}, which could be applied for NP pulmonary studies. This study shows a very good example that QDs can be used for bimodal imaging (PCXI and fluorescent imaging) of NP delivery dynamics and cellular localization. Another potential weakness of this study is that the use of five modes of imaging methods is very laborious and each mode requires special care and expertise when performing the experiment. In principle, selection of PCXI and one type of fluorescent imaging especially LSFM would not be lost much information on NP dynamic delivery, distribution, and biokinetics.

6. Outlook

For future targeted NP delivery studies development of bi- or tri-modal NP contrast agents is particularly useful in multimodal imaging modalities. Such multimodal NM/NP contrast agents permit visualization of controlled pulmonary delivery in real-time and 3D distribution, biokinetics, and cellular targeting of NP at single-cell resolution in intact mouse lung without the danger of artifacts due to the use of two or three different, potentially differently behaving contrast agents. The established multimodal imaging platform has opened new avenues to address various engineering obstacles on effective pulmonary delivery and scientific questions on NM targeting in a more sophisticated and detailed manner. For instance, besides the above mentioned pulmonary delivery methods, other application routes such as the nose-only exposure and oropharyngeal aspiration can also be investigated by this imaging platform. The main characteristics of 3D distribution pattern and cellular localization of NP in whole mouse lung has been elucidated by tissue-cleared LSFM, which will be discussed in our future studies. Since some clinically inhaled drugs are currently applied in a form of dry powder, determining whole-lung single-cell resolution distribution and biokinetics features and mechanisms of dry powder aerosol delivery (using DPIs) could be of high interest. The presented imaging platform provides high possibility to address this issue on dry powder particle delivery. Owing to the advantages of this imaging platform like 3D qualitative visualization and quantitative dosimetry, it could allow researchers optimize the delivery protocol to achieve a controlled and predictable dose of delivered substances to the lung, which is an area of active research. Moreover, it permits an in-depth understanding of the redistribution pattern and cellular interaction of NM/NPs in whole murine lungs (we have explored this, but the data is not presented here).

Cellular targeting of NP to cancer or other diseased regions is an attractive promise of NM. Visualization and confirmation of targeted delivery of novel-designed NP to the tumor or specific tissue regions in an animal model are largely relied on the general analysis using WBFL and WOFL or PET and SPECT, even though they have very restricted spatial resolution. By applying this imaging platform, one could for the first time understand whether the administered NM is specifically delivered to the diseased regions or the tumor cells and drug efficacy in intact organ/tissue at a single-cell resolution. To better understand the interaction of drug/NM with specific cell/tissue and the underlying mechanisms, one should consider expanding the application of tissue-cleared LSFM for different types of fluorescent-labeled drug/NM and the utilization of multicolor immunostaining with multi-wavelength

LSFM. Currently, different types of optical clearing protocols were reported in the literature, many of them have not been tested for fluorescent NMs, yet. The selection of mild and low-bleaching clearing protocols could amplify the LSFM application to some sensitive drugs/NM. Moreover, LSFM imaging of whole-mount immunostained or specific gene reported tissue samples of animal models would enable determination the interplay between NP and vasculature system, lymphatics, *etc.*, which is of central importance for understanding NM therapeutic efficacy and fate *in vivo*.

7. References

1. WHO The Top 10 Causes of Death. <https://www.who.int/en/news-room/fact-sheets/detail/the-top-10-causes-of-death>.
2. *The Burden of Lung Disease: The European Lung White Book*. European Respiratory Society: 2011.
3. Zhou, Q.; Tang, P.; Leung, S. S. Y.; Chan, J. G. Y.; Chan, H. K., Emerging Inhalation Aerosol Devices and Strategies: Where Are We Headed? *Adv Drug Deliver Rev* **2014**, *75*, 3-17.
4. Dolovich, M. B.; Dhand, R., Aerosol Drug Delivery: Developments in Device Design and Clinical Use. *Lancet* **2011**, *377*, 1032-1045.
5. Laube, B. L., The Expanding Role of Aerosols in Systemic Drug Delivery, Gene Therapy and Vaccination: An Update. *Transl Respir Med* **2014**, *2*, 3.
6. Kuzmov, A.; Minko, T., Nanotechnology Approaches for Inhalation Treatment of Lung Diseases. *J Control Release* **2015**, *219*, 500-518.
7. Kunjachan, S.; Ehling, J.; Storm, G.; Kiessling, F.; Lammers, T., Noninvasive Imaging of Nanomedicines and Nanotheranostics: Principles, Progress, and Prospects. *Chem. Rev.* **2015**, *115*, 10907-10937.
8. Todoroff, J.; Vanbever, R., Fate of Nanomedicines in the Lungs. *Curr Opin Colloid In* **2011**, *16*, 246-254.
9. Shi, J.; Kantoff, P. W.; Wooster, R.; Farokhzad, O. C., Cancer Nanomedicine: Progress, Challenges and Opportunities. *Nat Rev Cancer* **2017**, *17*, 20-37.
10. Doroudian, M.; MacLoughlin, R.; Poynton, F.; Prina-Mello, A.; Donnelly, S. C., Nanotechnology Based Therapeutics for Lung Disease. *Thorax* **2019**.
11. Smith, A. D. Big Moment for Nanotech: Oncology Therapeutics Poised for a Leap. <https://www.onclive.com/publications/Oncology-live/2013/June-2013/Big-Moment-for-Nanotech-Oncology-Therapeutics-Poised-for-a-Leap>.
12. Lee, W. H.; Loo, C. Y.; Traini, D.; Young, P. M., Inhalation of Nanoparticle-Based Drug for Lung Cancer Treatment: Advantages and Challenges. *Asian J Pharm Sci* **2015**, *10*, 481-489.
13. Loira-Pastoriza, C.; Todoroff, J.; Vanbever, R., Delivery Strategies for Sustained Drug Release in the Lungs. *Adv Drug Deliv Rev* **2014**, *75*, 81-91.
14. Schneider, C. S.; Xu, Q. G.; Boylan, N. J.; Chisholm, J.; Tang, B. C.; Schuster, B. S.; Henning, A.; Ensign, L. M.; Lee, E.; Adstamongkonkul, P.; Simons, B. W.; Wang, S. Y. S.; Gong, X. Q.; Yu, T.; Boyle, M. P.; Suk, J. S.; Hanes, J., Nanoparticles That Do Not Adhere to Mucus Provide Uniform and Long-Lasting Drug Delivery to Airways Following Inhalation. *Sci Adv* **2017**, *3*.
15. Hussain, S.; Joo, J.; Kang, J.; Kim, B.; Braun, G. B.; She, Z. G.; Kim, D.; Mann, A. P.; Molder, T.; Teesalu, T.; Carnazza, S.; Guglielmino, S.; Sailor, M. J.; Ruoslahti, E., Antibiotic-Loaded Nanoparticles Targeted to the Site of Infection Enhance Antibacterial Efficacy. *Nat Biomed Eng* **2018**, *2*, 95-103.
16. Agarwal, R.; Johnson, C. T.; Imhoff, B. R.; Donlan, R. M.; McCarty, N. A.; Garcia, A. J., Inhaled Bacteriophage-Loaded Polymeric Microparticles Ameliorate Acute Lung Infections. *Nat Biomed Eng* **2018**, *2*, 841-849.
17. Chan, W. C. W., Nanomedicine 2.0. *Accounts of Chem. Res.* **2017**, *50*, 627-632.
18. Yang, L.; Feuchtinger, A.; Moller, W.; Ding, Y.; Kutschke, D.; Moller, G.; Schittny, J. C.; Burgstaller, G.; Hofmann, W.; Stoeger, T.; Daniel, R.; Walch, A.; Schmid, O., Three-Dimensional Quantitative Co-Mapping of Pulmonary Morphology and Nanoparticle Distribution with Cellular Resolution in Nondissected Murine Lungs. *ACS Nano* **2019**, *13*, 1029-1041.
19. Kreyling, W. G.; Moller, W.; Holzwarth, U.; Hirn, S.; Wenk, A.; Schleh, C.; Schaffler, M.; Haberl, N.; Gibson, N.; Schittny, J. C., Age-Dependent Rat Lung Deposition Patterns of Inhaled 20 Nanometer Gold Nanoparticles and Their Quantitative Biokinetics in Adult Rats. *ACS Nano* **2018**, *12*, 7771-7790.
20. Kreyling, W. G.; Hirn, S.; Moller, W.; Schleh, C.; Wenk, A.; Celik, G.; Lipka, J.; Schaffler, M.; Haberl, N.; Johnston, B. D.; Sperling, R.; Schmid, G.; Simon, U.; Parak, W. J.; Semmler-Behnke, M., Air-Blood Barrier Translocation of Tracheally Instilled Gold Nanoparticles Inversely Depends on Particle Size. *ACS Nano* **2014**, *8*, 222-33.

21. Ellender, M.; Hodgson, A.; Wood, K. L.; Moody, J. C., Effect of Bronchopulmonary Lavage on Lung Retention and Clearance of Particulate Material in Hamsters. *Environ Health Perspect* **1992**, *97*, 209-13.
22. Lehnert, B. E.; Valdez, Y. E.; Tietjen, G. L., Alveolar Macrophage-Particle Relationships During Lung Clearance. *Am J Respir Cell Mol Biol* **1989**, *1*, 145-54.
23. Semmler-Behnke, M.; Takenaka, S.; Fertsch, S.; Wenk, A.; Seitz, J.; Mayer, P.; Oberdorster, G.; Kreyling, W. G., Efficient Elimination of Inhaled Nanoparticles from the Alveolar Region: Evidence for Interstitial Uptake and Subsequent Reentrainment onto Airways Epithelium. *Environ Health Perspect* **2007**, *115*, 728-33.
24. Schmid, O.; Moller, W.; Semmler-Behnke, M.; Ferron, G. A.; Karg, E.; Lipka, J.; Schulz, H.; Kreyling, W. G.; Stoeger, T., Dosimetry and Toxicology of Inhaled Ultrafine Particles. *Biomarkers* **2009**, *14 Suppl 1*, 67-73.
25. Oberdorster, G.; Sharp, Z.; Atudorei, V.; Elder, A.; Gelein, R.; Lunts, A.; Kreyling, W.; Cox, C., Extrapulmonary Translocation of Ultrafine Carbon Particles Following Whole-Body Inhalation Exposure of Rats. *J Toxicol Environ Health A* **2002**, *65*, 1531-43.
26. Stone, V.; Miller, M. R.; Clift, M. J. D.; Elder, A.; Mills, N. L.; Moller, P.; Schins, R. P. F.; Vogel, U.; Kreyling, W. G.; Alstrup Jensen, K.; Kuhlbusch, T. A. J.; Schwarze, P. E.; Hoet, P.; Pietroiusti, A.; De Vizcaya-Ruiz, A.; Baeza-Squiban, A.; Teixeira, J. P.; Tran, C. L.; Cassee, F. R., Nanomaterials Versus Ambient Ultrafine Particles: An Opportunity to Exchange Toxicology Knowledge. *Environ Health Perspect* **2017**, *125*, 106002.
27. Kreyling, W. G.; Semmler-Behnke, M.; Seitz, J.; Scymczak, W.; Wenk, A.; Mayer, P.; Takenaka, S.; Oberdorster, G., Size Dependence of the Translocation of Inhaled Iridium and Carbon Nanoparticle Aggregates from the Lung of Rats to the Blood and Secondary Target Organs. *Inhal. Toxicol.* **2009**, *21 Suppl 1*, 55-60.
28. Moller, W.; Felten, K.; Sommerer, K.; Scheuch, G.; Meyer, G.; Meyer, P.; Haussinger, K.; Kreyling, W. G., Deposition, Retention, and Translocation of Ultrafine Particles from the Central Airways and Lung Periphery. *Am. J. Resp. Crit. Care.* **2008**, *177*, 426-432.
29. Semmler, M.; Seitz, J.; Erbe, F.; Mayer, P.; Heyder, J.; Oberdorster, G.; Kreyling, W. G., Long-Term Clearance Kinetics of Inhaled Ultrafine Insoluble Iridium Particles from the Rat Lung, Including Transient Translocation into Secondary Organs. *Inhal Toxicol* **2004**, *16*, 453-9.
30. Snipes, M. B.; Boecker, B. B.; McClellan, R. O., Retention of Monodisperse or Polydisperse Aluminosilicate Particles Inhaled by Dogs, Rats, and Mice. *Toxicol Appl Pharmacol* **1983**, *69*, 345-62.
31. Jin, D.; Xi, P.; Wang, B.; Zhang, L.; Enderlein, J.; van Oijen, A. M., Nanoparticles for Super-Resolution Microscopy and Single-Molecule Tracking. *Nat Methods* **2018**, *15*, 415-423.
32. van der Zwaag, D.; Vanparijs, N.; Wijnands, S.; De Rycke, R.; De Geest, B. G.; Albertazzi, L., Super Resolution Imaging of Nanoparticles Cellular Uptake and Trafficking. *ACS Appl Mater Interfaces* **2016**, *8*, 6391-9.
33. Nava, R. G.; Li, W.; Gelman, A. E.; Krupnick, A. S.; Miller, M. J.; Kreisel, D., Two-Photon Microscopy in Pulmonary Research. *Semin Immunopathol* **2010**, *32*, 297-304.
34. Ibaldo-Mulli, A.; Timonen, K. L.; Peters, A.; Heinrich, J.; Wolke, G.; Lanki, T.; Buzorius, G.; Kreyling, W. G.; de Hartog, J.; Hoek, G.; ten Brink, H. M.; Pekkanen, J., Effects of Particulate Air Pollution on Blood Pressure and Heart Rate in Subjects with Cardiovascular Disease: A Multicenter Approach. *Environ Health Perspect* **2004**, *112*, 369-77.
35. Schmid, O.; Cassee, F. R., On the Pivotal Role of Dose for Particle Toxicology and Risk Assessment: Exposure Is a Poor Surrogate for Delivered Dose. *Part. Fibre Toxicol.* **2017**, *14*.
36. Vanhecke, D.; Rodriguez-Lorenzo, L.; Clift, M. J. D.; Blank, F.; Petri-Fink, A.; Rothen-Rutishauser, B., Quantification of Nanoparticles at the Single-Cell Level: An Overview About State-of-the-Art Techniques and Their Limitations. *Nanomedicine* **2014**, *9*, 1885-1900.
37. Semmler-Behnke, M.; Kreyling, W. G.; Lipka, J.; Fertsch, S.; Wenk, A.; Takenaka, S.; Schmid, G.; Brandau, W., Biodistribution of 1.4- and 18-Nm Gold Particles in Rats. *Small* **2008**, *4*, 2108-11.

38. Park, J. D.; Kim, J. K.; Jo, M. S.; Kim, Y. H.; Jeon, K. S.; Lee, J. H.; Faustman, E. M.; Lee, H. K.; Ahn, K.; Gulumian, M.; Oberdorster, G.; Yu, I. J., Lobar Evenness of Deposition/Retention in Rat Lungs of Inhaled Silver Nanoparticles: An Approach for Reducing Animal Use While Maximizing Endpoints. *Part Fibre Toxicol* **2019**, *16*, 2.
39. Yang, L.; Kuang, H.; Zhang, W.; Aguilar, Z. P.; Wei, H.; Xu, H., Comparisons of the Biodistribution and Toxicological Examinations after Repeated Intravenous Administration of Silver and Gold Nanoparticles in Mice. *Sci. Rep.* **2017**, *7*, 3303.
40. Yang, L.; Kuang, H.; Zhang, W.; Wei, H.; Xu, H., Quantum Dots Cause Acute Systemic Toxicity in Lactating Rats and Growth Restriction of Offspring. *Nanoscale* **2018**, *10*, 11564-11577.
41. Yang, L.; Kuang, H. J.; Zhang, W. Y.; Aguilar, Z. P.; Xiong, Y. H.; Lai, W. H.; Xu, H. Y.; Wei, H., Size Dependent Biodistribution and Toxicokinetics of Iron Oxide Magnetic Nanoparticles in Mice. *Nanoscale* **2015**, *7*, 625-636.
42. Barapatre, N.; Symvoulidis, P.; Moller, W.; Prade, F.; Deliolanis, N. C.; Hertel, S.; Winter, G.; Yildirim, A. O.; Stoeger, T.; Eickelberg, O.; Ntziachristos, V.; Schmid, O., Quantitative Detection of Drug Dose and Spatial Distribution in the Lung Revealed by Cryoslicing Imaging. *J. Pharm. Biomed. Anal.* **2015**, *102*, 129-36.
43. Yi, D.; Price, A.; Panoskaltsis-Mortari, A.; Naqwi, A.; Wiedmann, T. S., Measurement of the Distribution of Aerosols among Mouse Lobes by Fluorescent Imaging. *Anal. Biochem.* **2010**, *403*, 88-93.
44. Yi, D.; Naqwi, A.; Panoskaltsis-Mortari, A.; Wiedmann, T. S., Distribution of Aerosols in Mouse Lobes by Fluorescent Imaging. *Int. J. Pharm.* **2012**, *426*, 108-15.
45. Stelzer, E. H. K., Light-Sheet Fluorescence Microscopy for Quantitative Biology. *Nat Methods* **2015**, *12*, 23-26.
46. Erturk, A.; Becker, K.; Jahrling, N.; Mauch, C. P.; Hojer, C. D.; Egen, J. G.; Hellal, F.; Bradke, F.; Sheng, M.; Dodt, H. U., Three-Dimensional Imaging of Solvent-Cleared Organs Using 3disco. *Nat. Protoc.* **2012**, *7*, 1983-95.
47. van Rijjt, S. H.; Bolukbas, D. A.; Argyo, C.; Wipplinger, K.; Naureen, M.; Datz, S.; Eickelberg, O.; Meiners, S.; Bein, T.; Schmid, O.; Stoeger, T., Applicability of Avidin Protein Coated Mesoporous Silica Nanoparticles as Drug Carriers in the Lung. *Nanoscale* **2016**, *8*, 8058-8069.
48. Porra, L.; Degrugilliers, L.; Broche, L.; Albu, G.; Strengell, S.; Suhonen, H.; Fodor, G. H.; Petak, F.; Suortti, P.; Habre, W.; Sovijarvi, A. R. A.; Bayat, S., Quantitative Imaging of Regional Aerosol Deposition, Lung Ventilation and Morphology by Synchrotron Radiation Ct. *Sci Rep* **2018**, *8*, 3519.
49. Gradl, R.; Dierolf, M.; Yang, L.; Hehn, L.; Gunther, B.; Moller, W.; Kutschke, D.; Stoeger, T.; Gleich, B.; Achterhold, K.; Donnelley, M.; Pfeiffer, F.; Schmid, O.; Morgan, K. S., Visualizing Treatment Delivery and Deposition in Mouse Lungs Using in Vivo X-Ray Imaging. *J Control Release* **2019**.
50. Schmid, O.; Stoeger, T., Surface Area Is the Biologically Most Effective Dose Metric for Acute Nanoparticle Toxicity in the Lung. *J. Aerosol Sci.* **2016**, *99*, 133-143.
51. Ganguly, K.; Ettehadieh, D.; Upadhyay, S.; Takenaka, S.; Adler, T.; Karg, E.; Krombach, F.; Kreyling, W. G.; Schulz, H.; Schmid, O.; Stoeger, T., Early Pulmonary Response Is Critical for Extra-Pulmonary Carbon Nanoparticle Mediated Effects: Comparison of Inhalation Versus Intra-Arterial Infusion Exposures in Mice. *Part. Fibre Toxicol.* **2017**, *14*.
52. Li, Z.; Hulderman, T.; Salmen, R.; Chapman, R.; Leonard, S. S.; Young, S. H.; Shvedova, A.; Luster, M. I.; Simeonova, P. P., Cardiovascular Effects of Pulmonary Exposure to Single-Wall Carbon Nanotubes. *Environ Health Perspect* **2007**, *115*, 377-82.
53. Stoeger, T.; Reinhard, C.; Takenaka, S.; Schroepel, A.; Karg, E.; Ritter, B.; Heyder, J.; Schulz, H., Instillation of Six Different Ultrafine Carbon Particles Indicates a Surface Area Threshold Dose for Acute Lung Inflammation in Mice. *Environ Health Perspect* **2006**, *114*, 328-33.
54. Oberdorster, G.; Oberdorster, E.; Oberdorster, J., Nanotoxicology: An Emerging Discipline Evolving from Studies of Ultrafine Particles. *Environ Health Perspect* **2005**, *113*, 823-39.

55. Stoeger, T.; Schmid, O.; Takenaka, S.; Schulz, H., Inflammatory Response to Tio₂ and Carbonaceous Particles Scales Best with Bet Surface Area. *Environ Health Perspect* **2007**, *115*, A290-1; author reply A291-2.
56. Suzui, M.; Futakuchi, M.; Fukamachi, K.; Numano, T.; Abdelgied, M.; Takahashi, S.; Ohnishi, M.; Omori, T.; Tsuruoka, S.; Hirose, A.; Kanno, J.; Sakamoto, Y.; Alexander, D. B.; Alexander, W. T.; Xu, J. G.; Tsuda, H., Multiwalled Carbon Nanotubes Intratracheally Instilled into the Rat Lung Induce Development of Pleural Malignant Mesothelioma and Lung Tumors. *Cancer Science* **2016**, *107*, 924-935.
57. Miller, M. R.; Raftis, J. B.; Langrish, J. P.; McLean, S. G.; Samutrtai, P.; Connell, S. P.; Wilson, S.; Vesey, A. T.; Fokkens, P. H. B.; Boere, A. J. F.; Krystek, P.; Campbell, C. J.; Hadoke, P. W. F.; Donaldson, K.; Cassee, F. R.; Newby, D. E.; Duffin, R.; Mills, N. L., Inhaled Nanoparticles Accumulate at Sites of Vascular Disease. *ACS Nano* **2017**, *11*, 4542-4552.
58. Lu, X.; Zhu, Y.; Bai, R.; Wu, Z.; Qian, W.; Yang, L.; Cai, R.; Yan, H.; Li, T.; Pandey, V.; Liu, Y.; Lobie, P. E.; Chen, C.; Zhu, T., Long-Term Pulmonary Exposure to Multi-Walled Carbon Nanotubes Promotes Breast Cancer Metastatic Cascades. *Nat Nanotechnol* **2019**, *14*, 719-727.
59. Sattler, C.; Moritz, F.; Chen, S.; Steer, B.; Kutschke, D.; Irmiler, M.; Beckers, J.; Eickelberg, O.; Schmitt-Kopplin, P.; Adler, H.; Stoeger, T., Nanoparticle Exposure Reactivates Latent Herpesvirus and Restores a Signature of Acute Infection. *Part Fibre Toxicol* **2017**, *14*, 2.
60. DeLoid, G. M.; Cohen, J. M.; Pyrgiotakis, G.; Demokritou, P., Preparation, Characterization, and in Vitro Dosimetry of Dispersed, Engineered Nanomaterials. *Nat Protoc* **2017**, *12*, 355-371.
61. Lamon, L.; Aschberger, K.; Asturiol, D.; Richarz, A.; Worth, A., Grouping of Nanomaterials to Read-across Hazard Endpoints: A Review. *Nanotoxicology* **2019**, *13*, 100-118.
62. Poh, T. Y.; Ali, N.; Mac Aogain, M.; Kathawala, M. H.; Setyawati, M. I.; Ng, K. W.; Chotirmall, S. H., Inhaled Nanomaterials and the Respiratory Microbiome: Clinical, Immunological and Toxicological Perspectives. *Part Fibre Toxicol* **2018**, *15*, 46.
63. Rubin, B. K., Pediatric Aerosol Therapy: New Devices and New Drugs. *Respir Care* **2011**, *56*, 1411-21; discussion 1421-3.
64. Moller, W.; Heimbeck, I.; Hofer, T. P. J.; Saba, G. K.; Neiswirth, M.; Frankenberger, M.; Ziegler-Heitbrock, L., Differential Inflammatory Response to Inhaled Lipopolysaccharide Targeted Either to the Airways or the Alveoli in Man. *Plos One* **2012**, *7*.
65. Denyer, J.; Dyche, T., The Adaptive Aerosol Delivery (Aad) Technology: Past, Present, and Future. *J Aerosol Med Pulm D* **2010**, *23*, S1-S10.
66. Smyth, H. D. C., The Influence of Formulation Variables on the Performance of Alternative Propellant-Driven Metered Dose Inhalers. *Adv Drug Deliver Rev* **2003**, *55*, 807-828.
67. Sumbly, B.; Slater, A.; Atkins, P. J.; Prime, D., Review of Dry Powder Inhalers. *Adv Drug Deliv Rev* **1997**, *26*, 51-58.
68. Atkins, P. J., Dry Powder Inhalers: An Overview. *Respir Care* **2005**, *50*, 1304-12; discussion 1312.
69. Cryan, S. A.; Sivadas, N.; Garcia-Contreras, L., In Vivo Animal Models for Drug Delivery across the Lung Mucosal Barrier. *Adv Drug Deliv Rev* **2007**, *59*, 1133-51.
70. Guillon, A.; Secher, T.; Dailey, L. A.; Vecellio, L.; de Monte, M.; Si-Tahar, M.; Diot, P.; Page, C. P.; Heuze-Vourc'h, N., Insights on Animal Models to Investigate Inhalation Therapy: Relevance for Biotherapeutics. *Int J Pharm* **2018**, *536*, 116-126.
71. Fernandes, C. A.; Vanbever, R., Preclinical Models for Pulmonary Drug Delivery. *Expert Opin Drug Deliv* **2009**, *6*, 1231-45.
72. Pauluhn, J., Overview of Testing Methods Used in Inhalation Toxicity: From Facts to Artifacts. *Toxicology Letters* **2003**, *140*, 183-193.
73. Nahar, K.; Gupta, N.; Gauvin, R.; Absar, S.; Patel, B.; Gupta, V.; Khademhosseini, A.; Ahsan, F., In Vitro, in Vivo and Ex Vivo Models for Studying Particle Deposition and Drug Absorption of Inhaled Pharmaceuticals. *European Journal of Pharmaceutical Sciences* **2013**, *49*, 805-818.

74. Verma, R. K.; Kaur, J.; Kumar, K.; Yadav, A. B.; Misra, A., Intracellular Time Course, Pharmacokinetics, and Biodistribution of Isoniazid and Rifabutin Following Pulmonary Delivery of Inhalable Microparticles to Mice. *Antimicrob Agents Ch* **2008**, *52*, 3195-3201.
75. Mainelis, G.; Seshadri, S.; Garbuzenko, O. B.; Han, T.; Wang, Z.; Minko, T., Characterization and Application of a Nose-Only Exposure Chamber for Inhalation Delivery of Liposomal Drugs and Nucleic Acids to Mice. *J Aerosol Med Pulm Drug Deliv* **2013**, *26*, 345-54.
76. Codrons, V.; Vanderbist, F.; Ucar, B.; Preat, V.; Vanbever, R., Impact of Formulation and Methods of Pulmonary Delivery on Absorption of Parathyroid Hormone (1-34) from Rat Lungs. *J Pharm Sci-US* **2004**, *93*, 1241-1252.
77. Gotz, A. A.; Rozman, J.; Rodel, H. G.; Fuchs, H.; Gailus-Durner, V.; de Angelis, M. H.; Klingenspor, M.; Stoeger, T., Comparison of Particle-Exposure Triggered Pulmonary and Systemic Inflammation in Mice Fed with Three Different Diets. *Part. Fibre Toxicol.* **2011**, *8*.
78. Robichaud, A.; Fereydoonzad, L.; Schuessler, T. F., Delivered Dose Estimate to Standardize Airway Hyperresponsiveness Assessment in Mice. *Am J Physiol-Lung C* **2015**, *308*, L837-L846.
79. Minne, A.; Louahed, J.; Mehouden, S.; Baras, B.; Renaud, J. C.; Vanbever, R., The Delivery Site of a Monovalent Influenza Vaccine within the Respiratory Tract Impacts on the Immune Response. *Immunology* **2007**, *122*, 316-325.
80. Babin, A. L.; Cannet, C.; Gerard, C.; Saint-Mezard, P.; Page, C. P.; Sparrer, H.; Matsuguchi, T.; Beckmann, N., Bleomycin-Induced Lung Injury in Mice Investigated by Mri: Model Assessment for Target Analysis. *Magn Reson Med* **2012**, *67*, 499-509.
81. De Vooght, V.; Vanoirbeek, J. A.; Haenen, S.; Verbeken, E.; Nemery, B.; Hoet, P. H., Oropharyngeal Aspiration: An Alternative Route for Challenging in a Mouse Model of Chemical-Induced Asthma. *Toxicology* **2009**, *259*, 84-9.
82. Woods, A.; Patel, A.; Spina, D.; Rifo-Vasquez, Y.; Babin-Morgan, A.; de Rosales, R. T. M.; Sunassee, K.; Clark, S.; Collins, H.; Bruce, K.; Dailey, L. A.; Forbes, B., In Vivo Biocompatibility, Clearance, and Biodistribution of Albumin Vehicles for Pulmonary Drug Delivery. *J. Control. Release.* **2015**, *210*, 1-9.
83. Taruttis, A.; Ntziachristos, V., Advances in Real-Time Multispectral Optoacoustic Imaging and Its Applications. *Nat Photonics* **2015**, *9*, 219-227.
84. Newman, S.; Bennett, W. D.; Biddiscombe, M.; Devadason, S. G.; Dolovich, M. B.; Fleming, J.; Haeussermann, S.; Kietzig, C.; Kuehl, P. J.; Laube, B. L.; Sommerer, K.; Taylor, G.; Usmani, O. S.; Zeman, K. L., Standardization of Techniques for Using Planar (2d) Imaging for Aerosol Deposition Assessment of Orally Inhaled Products. *J Aerosol Med Pulm D* **2012**, *25*, S10-S28.
85. Eberl, S.; Chan, H. K.; Daviskas, E., Spect Imaging for Radioaerosol Deposition and Clearance Studies. *Journal of Aerosol Medicine-Deposition Clearance and Effects in the Lung* **2006**, *19*, 8-20.
86. Chatziioannou, A. F., Instrumentation for Molecular Imaging in Preclinical Research: Micro-Pet and Micro-Spect. *Proc Am Thorac Soc* **2005**, *2*, 533-6, 510-11.
87. Newman, S. P.; Pitcairn, G. R.; Hirst, P. H.; Rankin, L., Radionuclide Imaging Technologies and Their Use in Evaluating Asthma Drug Deposition in the Lungs. *Adv Drug Deliver Rev* **2003**, *55*, 851-867.
88. Dolovich, M.; Labiris, R., Imaging Drug Delivery and Drug Responses in the Lung. *Proc Am Thorac Soc* **2004**, *1*, 329-37.
89. Gammon, S. T.; Foje, N.; Brewer, E. M.; Owers, E.; Downs, C. A.; Budde, M. D.; Leevy, W. M.; Helms, M. N., Preclinical Anatomical, Molecular, and Functional Imaging of the Lung with Multiple Modalities. *Am J Physiol Lung Cell Mol Physiol* **2014**, *306*, L897-914.
90. Caravan, P.; Yang, Y.; Zachariah, R.; Schmitt, A.; Mino-Kenudson, M.; Chen, H. H.; Sosnovik, D. E.; Dai, G.; Fuchs, B. C.; Lanuti, M., Molecular Magnetic Resonance Imaging of Pulmonary Fibrosis in Mice. *Am J Respir Cell Mol Biol* **2013**, *49*, 1120-6.
91. Martin, A. R.; Thompson, R. B.; Finlay, W. H., Mri Measurement of Regional Lung Deposition in Mice Exposed Nose-Only to Nebulized Superparamagnetic Iron Oxide Nanoparticles. *J Aerosol Med Pulm D* **2008**, *21*, 335-341.

92. Arms, L.; Smith, D. W.; Flynn, J.; Palmer, W.; Martin, A.; Woldu, A.; Hua, S., Advantages and Limitations of Current Techniques for Analyzing the Biodistribution of Nanoparticles. *Front Pharmacol* **2018**, *9*, 802.
93. Donnelley, M.; Morgan, K. S.; Siu, K. K. W.; Parsons, D. W., Variability of in Vivo Fluid Dose Distribution in Mouse Airways Is Visualized by High-Speed Synchrotron X-Ray Imaging. *Journal of Aerosol Medicine and Pulmonary Drug Delivery* **2013**, *26*, 307-316.
94. Donnelley, M.; Morgan, K. S.; Awadalla, M.; Farrow, N. R.; Hall, C.; Parsons, D. W., High-Resolution Mucociliary Transport Measurement in Live Excised Large Animal Trachea Using Synchrotron X-Ray Imaging. *Respir Res* **2017**, *18*, 95.
95. Barre, S. F.; Haberthur, D.; Cremona, T. P.; Stampanoni, M.; Schittny, J. C., The Total Number of Acini Remains Constant Throughout Postnatal Rat Lung Development. *Am. J. Physiol.-Lung C* **2016**, *311*, L1082-L1089.
96. Tonnis, W. F.; Bagerman, M.; Weij, M.; Sjollem, J.; Frijlink, H. W.; Hinrichs, W. L.; de Boer, A. H., A Novel Aerosol Generator for Homogenous Distribution of Powder over the Lungs after Pulmonary Administration to Small Laboratory Animals. *Eur J Pharm Biopharm* **2014**, *88*, 1056-63.
97. Cherry, S. R., Multimodality Imaging: Beyond Pet/Ct and Spect/Ct. *Semin Nucl Med* **2009**, *39*, 348-53.
98. Ale, A.; Ermolayev, V.; Herzog, E.; Cohrs, C.; de Angelis, M. H.; Ntziachristos, V., Fmt-Xct: In Vivo Animal Studies with Hybrid Fluorescence Molecular Tomography-X-Ray Computed Tomography. *Nat Methods* **2012**, *9*, 615-20.
99. Catana, C.; Procissi, D.; Wu, Y.; Judenhofer, M. S.; Qi, J.; Pichler, B. J.; Jacobs, R. E.; Cherry, S. R., Simultaneous in Vivo Positron Emission Tomography and Magnetic Resonance Imaging. *Proc Natl Acad Sci U S A* **2008**, *105*, 3705-10.
100. Head, H. W.; Dodd, G. D., 3rd; Bao, A.; Soundararajan, A.; Garcia-Rojas, X.; Prihoda, T. J.; McManus, L. M.; Goins, B. A.; Santoyo, C. A.; Phillips, W. T., Combination Radiofrequency Ablation and Intravenous Radiolabeled Liposomal Doxorubicin: Imaging and Quantification of Increased Drug Delivery to Tumors. *Radiology* **2010**, *255*, 405-14.
101. Zhang, R.; Xiong, C.; Huang, M.; Zhou, M.; Huang, Q.; Wen, X.; Liang, D.; Li, C., Peptide-Conjugated Polymeric Micellar Nanoparticles for Dual Spect and Optical Imaging of Ephb4 Receptors in Prostate Cancer Xenografts. *Biomaterials* **2011**, *32*, 5872-9.
102. Cormode, D. P.; Skajaa, T.; van Schooneveld, M. M.; Koole, R.; Jarzyna, P.; Lobatto, M. E.; Calcagno, C.; Barazza, A.; Gordon, R. E.; Zanzonico, P.; Fisher, E. A.; Fayad, Z. A.; Mulder, W. J. M., Nanocrystal Core High-Density Lipoproteins: A Multimodality Contrast Agent Platform. *Nano Letters* **2008**, *8*, 3715-3723.
103. Mulder, W. J. M.; Koole, R.; Brandwijk, R. J.; Storm, G.; Chin, P. T. K.; Strijkers, G. J.; Donega, C. D.; Nicolay, K.; Griffioen, A. W., Quantum Dots with a Paramagnetic Coating as a Bimodal Molecular Imaging Probe. *Nano Letters* **2006**, *6*, 1-6.
104. Kamaly, N.; Kalber, T.; Ahmad, A.; Oliver, M. H.; So, P. W.; Herlihy, A. H.; Bell, J. D.; Jorgensen, M. R.; Miller, A. D., Bimodal Paramagnetic and Fluorescent Liposomes for Cellular and Tumor Magnetic Resonance Imaging. *Bioconjugate Chem* **2008**, *19*, 118-129.
105. Huh, Y. M.; Jun, Y. W.; Song, H. T.; Kim, S.; Choi, J. S.; Lee, J. H.; Yoon, S.; Kim, K. S.; Shin, J. S.; Suh, J. S.; Cheon, J., In Vivo Magnetic Resonance Detection of Cancer by Using Multifunctional Magnetic Nanocrystals. *Journal of the American Chemical Society* **2005**, *127*, 12387-12391.
106. Donnelley, M.; Morgan, K. S.; Siu, K. K.; Parsons, D. W., Dry Deposition of Pollutant and Marker Particles onto Live Mouse Airway Surfaces Enhances Monitoring of Individual Particle Mucociliary Transit Behaviour. *J Synchrotron Radiat* **2012**, *19*, 551-8.
107. Gradl, R.; Dierolf, M.; Gunther, B.; Hehn, L.; Moller, W.; Kutschke, D.; Yang, L.; Donnelley, M.; Murrie, R.; Erl, A.; Stoeger, T.; Gleich, B.; Achterhold, K.; Schmid, O.; Pfeiffer, F.; Morgan, K. S., In Vivo Dynamic Phase-Contrast X-Ray Imaging Using a Compact Light Source. *Sci Rep* **2018**, *8*, 6788.
108. Eggl, E.; Dierolf, M.; Achterhold, K.; Jud, C.; Gunther, B.; Braig, E.; Gleich, B.; Pfeiffer, F., The Munich Compact Light Source: Initial Performance Measures. *J Synchrotron Radiat* **2016**, *23*, 1137-42.

109. Achterhold, K.; Bech, M.; Schleede, S.; Potdevin, G.; Ruth, R.; Loewen, R.; Pfeiffer, F., Monochromatic Computed Tomography with a Compact Laser-Driven X-Ray Source. *Sci Rep* **2013**, *3*, 1313.
110. Donnelley, M.; Siu, K. K.; Jamison, R. A.; Parsons, D. W., Synchrotron Phase-Contrast X-Ray Imaging Reveals Fluid Dosing Dynamics for Gene Transfer into Mouse Airways. *Gene Ther* **2012**, *19*, 8-14.
111. Brown, D. G.; Riederer, S. J., Contrast-to-Noise Ratios in Maximum Intensity Projection Images. *Magn. Reson. Med.* **1992**, *23*, 130-7.
112. Wallau, B. R.; Schmitz, A.; Perry, S. F., Lung Morphology in Rodents (Mammalia, Rodentia) and Its Implications for Systematics. *J. Morphol.* **2000**, *246*, 228-48.
113. Hsia, C. C.; Hyde, D. M.; Ochs, M.; Weibel, E. R.; Structure, A. E. J. T. F. o. Q. A. o. L., An Official Research Policy Statement of the American Thoracic Society/European Respiratory Society: Standards for Quantitative Assessment of Lung Structure. *Am. J. Respir. Crit. Care. Med.* **2010**, *181*, 394-418.
114. Michel, R. P.; Cruz-Orive, L. M., Application of the Cavalieri Principle and Vertical Sections Method to Lung: Estimation of Volume and Pleural Surface Area. *J. Microsc.* **1988**, *150*, 117-36.
115. Muralidharan, P.; Malapit, M.; Mallory, E.; Hayes, D., Jr.; Mansour, H. M., Inhalable Nanoparticulate Powders for Respiratory Delivery. *Nanomedicine* **2015**, *11*, 1189-99.
116. Collins, F. S.; Varmus, H., A New Initiative on Precision Medicine. *N Engl J Med* **2015**, *372*, 793-5.
117. Wistuba, II; Gazdar, A. F., Lung Cancer Preneoplasia. *Annu Rev Pathol* **2006**, *1*, 331-48.
118. van Rijjt, S. H.; Bein, T.; Meiners, S., Medical Nanoparticles for Next Generation Drug Delivery to the Lungs. *European Respiratory Journal* **2014**, *44*, 765-774.
119. Cai, R.; Pan, C.; Ghasemigharagoz, A.; Todorov, M. I.; Forstera, B.; Zhao, S.; Bhatia, H. S.; Parra-Damas, A.; Mrowka, L.; Theodorou, D.; Rempfler, M.; Xavier, A. L. R.; Kress, B. T.; Benakis, C.; Steinke, H.; Liebscher, S.; Bechmann, I.; Liesz, A.; Menze, B.; Kerschensteiner, M., *et al.*, Panoptic Imaging of Transparent Mice Reveals Whole-Body Neuronal Projections and Skull-Meninges Connections. *Nat Neurosci* **2019**, *22*, 317-327.
120. Pan, C.; Cai, R.; Quacquarelli, F. P.; Ghasemigharagoz, A.; Lourbopoulos, A.; Matryba, P.; Plesnila, N.; Dichgans, M.; Hellal, F.; Erturk, A., Shrinkage-Mediated Imaging of Entire Organs and Organisms Using Udisco. *Nat Methods* **2016**, *13*, 859-67.
121. Susaki, E. A.; Tainaka, K.; Perrin, D.; Yukinaga, H.; Kuno, A.; Ueda, H. R., Advanced Cubic Protocols for Whole-Brain and Whole-Body Clearing and Imaging. *Nat. Protoc.* **2015**, *10*, 1709-1727.
122. Feuchtinger, A.; Walch, A.; Dobosz, M., Deep Tissue Imaging: A Review from a Preclinical Cancer Research Perspective. *Histochem. Cell Biol.* **2016**, *146*, 781-806.
123. Belle, M.; Godefroy, D.; Couly, G.; Malone, S. A.; Collier, F.; Giacobini, P.; Chedotal, A., Tridimensional Visualization and Analysis of Early Human Development. *Cell* **2017**, *169*, 161-173 e12.
124. Tainaka, K.; Kubota, S. I.; Suyama, T. Q.; Susaki, E. A.; Perrin, D.; Ukai-Tadenuma, M.; Ukai, H.; Ueda, H. R., Whole-Body Imaging with Single-Cell Resolution by Tissue Decolorization. *Cell* **2014**, *159*, 911-924.
125. Scott, G. D.; Blum, E. D.; Fryer, A. D.; Jacoby, D. B., Tissue Optical Clearing, Three-Dimensional Imaging, and Computer Morphometry in Whole Mouse Lungs and Human Airways. *Am. J. Respir. Cell Mol. Biol.* **2014**, *51*, 43-55.
126. Ochoa, L. F.; Kholodnykh, A.; Villarreal, P.; Tian, B.; Pal, R.; Freiberg, A. N.; Brasier, A. R.; Motamedi, M.; Vargas, G., Imaging of Murine Whole Lung Fibrosis by Large Scale 3d Microscopy Aided by Tissue Optical Clearing. *Sci Rep* **2018**, *8*, 13348.
127. Mzinza, D. T.; Fleige, H.; Laarmann, K.; Willenzon, S.; Ristenpart, J.; Spanier, J.; Sutter, G.; Kalinke, U.; Valentin-Weigand, P.; Forster, R., Application of Light Sheet Microscopy for Qualitative and Quantitative Analysis of Bronchus-Associated Lymphoid Tissue in Mice. *Cell Mol Immunol* **2018**, *15*, 875-887.

128. Cuccarese, M. F.; Dubach, J. M.; Pfirschke, C.; Engblom, C.; Garris, C.; Miller, M. A.; Pittet, M. J.; Weissleder, R., Heterogeneity of Macrophage Infiltration and Therapeutic Response in Lung Carcinoma Revealed by 3d Organ Imaging. *Nat. Commun.* **2017**, *8*.
129. Sindhvani, S.; Syed, A. M.; Wilhelm, S.; Glancy, D. R.; Chen, Y. Y.; Dobosz, M.; Chan, W. C., Three-Dimensional Optical Mapping of Nanoparticle Distribution in Intact Tissues. *ACS Nano* **2016**, *10*, 5468-78.
130. Kingston, B. R.; Syed, A. M.; Ngai, J.; Sindhvani, S.; Chan, W. C. W., Assessing Micrometastases as a Target for Nanoparticles Using 3d Microscopy and Machine Learning. *P Natl Acad Sci USA* **2019**, *116*, 14937-14946.
131. Syed, A. M.; Sindhvani, S.; Wilhelm, S.; Kingston, B. R.; Lee, D. S. W.; Gommerman, J. L.; Chan, W. C. W., Three-Dimensional Imaging of Transparent Tissues Via Metal Nanoparticle Labeling. *J. Am. Chem. Soc.* **2017**, *139*, 9961-9971.
132. Murray, E.; Cho, J. H.; Goodwin, D.; Ku, T.; Swaney, J.; Kim, S. Y.; Choi, H.; Park, Y. G.; Park, J. Y.; Hubbert, A.; Mccue, M.; Vassallo, S.; Bakh, N.; Frosch, M. P.; Wedeen, V. J.; Seung, H. S.; Chung, K., Simple, Scalable Proteomic Imaging for High-Dimensional Profiling of Intact Systems. *Cell* **2015**, *163*, 1500-1514.
133. Sanderson, M. J., Exploring Lung Physiology in Health and Disease with Lung Slices. *Pulm. Pharmacol. Ther.* **2011**, *24*, 452-465.
134. Knudsen, L.; Weibel, E. R.; Gundersen, H. J.; Weinstein, F. V.; Ochs, M., Assessment of Air Space Size Characteristics by Intercept (Chord) Measurement: An Accurate and Efficient Stereological Approach. *J. Appl. Physiol. (1985)* **2010**, *108*, 412-21.
135. Counter, W. B.; Wang, I. Q.; Farncombe, T. H.; Labiris, N. R., Airway and Pulmonary Vascular Measurements Using Contrast-Enhanced Micro-Ct in Rodents. *Am. J. Physiol.-Lung C* **2013**, *304*, L831-L843.
136. Klingberg, A.; Hasenberg, A.; Ludwig-Portugall, I.; Medyukhina, A.; Mann, L.; Brenzel, A.; Engel, D. R.; Figge, M. T.; Kurts, C.; Gunzer, M., Fully Automated Evaluation of Total Glomerular Number and Capillary Tuft Size in Nephritic Kidneys Using Lightsheet Microscopy. *J. Am. Soc. Nephrol.* **2017**, *28*, 452-459.
137. Kunjachan, S.; Gremse, F.; Theek, B.; Koczera, P.; Pola, R.; Pechar, M.; Etrych, T.; Ulbrich, K.; Storm, G.; Kiessling, F.; Lammers, T., Noninvasive Optical Imaging of Nanomedicine Biodistribution. *Acs Nano* **2013**, *7*, 252-262.
138. Fouras, A.; Kitchen, M. J.; Dubsky, S.; Lewis, R. A.; Hooper, S. B.; Hourigan, K., The Past, Present, and Future of X-Ray Technology for in Vivo Imaging of Function and Form. *J Appl Phys* **2009**, *105*.
139. Donnelley, M.; Siu, K. K. W.; Morgan, K. S.; Skinner, W.; Suzuki, Y.; Takeuchi, A.; Uesugi, K.; Yagi, N.; Parsons, D. W., A New Technique to Examine Individual Pollutant Particle and Fibre Deposition and Transit Behaviour in Live Mouse Trachea. *J Synchrotron Radiat* **2010**, *17*, 719-729.
140. Donnelley, M.; Morgan, K. S.; Fouras, A.; Skinner, W.; Uesugi, K.; Yagi, N.; Siu, K. K.; Parsons, D. W., Real-Time Non-Invasive Detection of Inhalable Particulates Delivered into Live Mouse Airways. *J Synchrotron Radiat* **2009**, *16*, 553-61.
141. Lusic, H.; Grinstaff, M. W., X-Ray-Computed Tomography Contrast Agents. *Chem Rev* **2013**, *113*, 1641-66.
142. De La Vega, J. C.; Hafeli, U. O., Utilization of Nanoparticles as X-Ray Contrast Agents for Diagnostic Imaging Applications. *Contrast Media Mol I* **2015**, *10*, 81-95.

8. Acknowledgments

Pursuing and completing a Ph.D. degree is one of the biggest things in my life until now. At the moment, I would like to express my deepest appreciation to my supervisor Dr. Otmar Schmid (Comprehensive Pneumology Center (CPC) & Institute of Lung Biology and Disease (iLBD), Helmholtz Zentrum München), who offered me the opportunity to do my doctoral studies in his group, gave me tremendous guidance, and trained me how to be a qualified and independent researcher. Over the last four years, what impressed me most from him is not only the immense knowledge and expertise but also the scientific attitude and enthusiasm. I am most grateful to him for his selfless and countless support and help, for high flexibility and accessibility, for long and open discussions, and for allowing me to attend the numerous scientific conferences/workshops. Thank you Otmar for all of that you have taught me, given me, encouraged me, and inspired me, which makes the last four years' experience so rewarding. It has been a special journey for me to be part of your group and I was really enjoyed work with you in the whole doctoral period and hopefully it will be continued in my future career.

Foremost, I address my most sincere gratitude to my TUM advisors Prof. Dr. Daniel Razansky and Prof. Dr. Franz Pfeiffer and the member of my thesis committee Dr. Tobias Stoeger (CPC/iLBD, Helmholtz Zentrum München) for their continuous support, insightful discussion, and creative ideas.

Furthermore, I am very much grateful to TUM researchers from Chair of Biomedical Physics, Department of Physics, Dr. Kaye S. Morgan, Regine, Gradl, and Dr. Martin Dierolf (group members of Prof. Dr. Franz Pfeiffer) for the highly productive project, nice working atmosphere, constructive discussion, and prompt feedback. It was a great experience to work with all of you.

Many thanks go to the members of Dr. Tobias Stoeger lab (CPC/iLBD), Prof. Dr. Markus Rehberg, Dr. Carola Voss, David Kutschke, Mehwish Ishaque, Anna Fuchs, Dr. Carolina Ballester López, and Qiongliang Liu for their discussion, support, and help.

I would like to deeply thank my collaborator at Institute for Biological and Medical Imaging (IBMI), Helmholtz Zentrum München, Neda Davoudi (a group member of Prof. Dr. Daniel Razansky) for her support and contribution with data analysis.

I also appreciate a lot to my CPC/iLBD collaborators Dr. Gerald Burgstaller and Arunima Sengupta with whom we have great project collaboration and effective experimental progress (immunostaining).

I would further thank Dr. Annette Feuchtinger and Prof. Dr. Axel Walch from Research Unit Analytical Pathology, Helmholtz Zentrum München for providing me the use of light sheet fluorescent microscopy and for the guidance and support about sample treatment and imaging scanning, process, and analysis.

My deep gratitude goes to all former and current members of our group (Dr. Schmid lab; (CPC/iLBD): Dr. Winfried Möller, Dr. Yaobo Ding, Andreas Schröppel, Paula Mayer, Gunter Eder, Dr. Anke Lenz, Marina Schuhmann, Dr. Pramod Kumar, Dr. Ali Farnoud, Ali Doryab, and Sezer Orak.

I would like to address my special acknowledgment to an outstanding CPC Research School team, specifically Prof. Dr. Silke Meiners, PD Dr. Claudia Staab-Weijnitz, Dr. Darcy Wagner and Dr. Doreen Franke, for their help, motivation, enthusiasm, and challenges during the entire graduate school program. Also I am very grateful to the secretary Silke Lauer for the support and help on general tasks and in personal life.

I greatly thank all my classmates, colleagues, and friends in CPC and iLBD, especially Dr. Dongshen Jiang, Juan Liu, Li Wan, Qing Yu, Simon Christ, Dr. Tim Koopmans, Prof. Xiaoying Wang, Dr. Youjia Yu, Lianyong Han, Verna Häfner, Qiaoxia Zhou, Severine Selina Somlo, Dr. Hengshuo Liu, Carmela Morrone, Ilias Angelidis, Christoph Mayr, Dr. Jie Chen, Dr. Xinyuan Wang) with whom we have some pleasantly scientific discussion and/or lots of invaluable living memories.

I am very thankful to the collaboration partners for all the input and contribution to the publications.

Most importantly, I feel very fortunate to have my family's tremendous support and endless love. Words cannot express my gratitude and appreciation to my parents, my sister, and my wife and our young kid.

Thank you all kind people.